UNIVERSITÀ DEGLI STUDI DI PERUGIA

Dipartimento di Fisica e Geologia

PhD Course in
Science and Technology for Physics and Geology
Curriculum in Physics

Doctoral Thesis:

Measurement of $Br(K^+ \to \pi^+ \nu \bar{\nu})$ with the NA62 experiment at CERN

Supervisors:

Prof. Giuseppina ANZIVINO

Dr. Mauro PICCINI

Candidate:

Francesco BRIZIOLI

Academic years 2017-2020, XXXIII Cycle

Abstract

The ultra-rare decay $K^+ \to \pi^+\nu\bar{\nu}$, with a very precisely predicted branching ratio of less than 10^{-10}, is one of the best candidates to reveal indirect effects of new physics at the highest mass scales. The NA62 experiment at CERN SPS is designed to measure $Br(K^+ \to \pi^+\nu\bar{\nu})$ with a decay-in-flight technique, novel for this channel. NA62 took data in 2016, 2017 and 2018. Statistics collected in 2016 and 2017 allows NA62 to reach the Standard Model sensitivity for the $K^+ \to \pi^+\nu\bar{\nu}$ search. The analysis of the 2018 data, topic of this PhD thesis, leads to the most precise preliminary measurement ever performed combining the full data set: $Br(K^+ \to \pi^+\nu\bar{\nu}) = (1.10^{+0.40}_{-0.35\ stat} \pm 0.03_{syst}) \cdot 10^{-10}$, with 3.5σ significance for the process observation. The context of the measurement is presented, the details of the data analysis are described, with particular emphasis on the improvements achieved in the experimental sensitivity, and the prospects are illustrated.

Thesis submitted in December 2020.

Acknowledgements

To my Mum and my Dad

I would like to express my sincere gratitude to all the people that have been part of my life during the last three years of my doctoral studies.

I am particularly grateful to my supervisors, Giuseppina Anzivino and Mauro Piccini, and to the other members of the NA62-Perugia group, Patrizia Cenci, Bruno Checcucci, Viacheslav Duk, Ermanno Imbergamo, Riccardo Lollini, Pasquale Lubrano, Monica Pepe and Roberto Piandani, for all their patience, their support and their advice.

A special thank goes to all the members of the NA62 Collaboration, who have given me the opportunity to learn a lot and to do my best for our Experiment.

Table of Contents

List of Tables

List of Figures

Introduction

The Standard Model of fundamental interactions (SM) is a quantum field theory developed in the 20^{th} century starting from the works of Glashow, Weinberg and Salam [1] [2] [3], that provides a full picture of the existing elementary particles and how they interact. The SM comprises quarks and leptons, grouped in three generations, as the fundamental building blocks of matter, and describes their interactions through the exchange of force mediators, the gauge bosons: the photon for electromagnetic interactions, the W and Z bosons for weak interactions and the gluons for strong interactions. The electromagnetic and weak interactions are unified in the electroweak theory. The model is based on the gauge group $SU(3)_C \otimes SU(2)_L \otimes U(1)_Y$, where $SU(3)_C$ is the group of the strong interaction described by quantum chromodynamics (QCD), while $SU(2)_L \otimes U(1)_Y$ represents the electroweak interaction. A detailed description of the SM is provided in [4].

This theory accurately predicts most of the processes involving elementary particles and is well confirmed by experimental observations. The latest main confirmation in chronological order has been provided by the observation of the *Higgs boson* by the ATLAS and the CMS experiments at CERN LHC in 2012 [5] [6]. The existence of this particle was predicted in the SM framework introducing a scalar field in the Lagrangian that leads to a spontaneous symmetry breaking in gauge theories [7] [8] [9] [10] [11] [12], needed to answer to a fundamental question: how do the W and Z gauge bosons (and, in general, the fermions) acquire mass? Applying this mechanism to the electroweak theory leads to the generation of the W and Z masses and to the prediction of the existence of the Higgs boson [13] [14] [15]. The same scalar field is also used to give mass to the fundamental fermions through Yukawa interaction.

Even if the SM successfully describes most of the experimental observations, there are still fundamental questions, triggered by experimental results, without a proper answer in its framework. The most relevant are: the observation of neutrino flavor oscillations [16] [17] contradicts the hypothesis of massless neutrinos, the dark matter evidenced via astrophysical and cosmological observations [18] does not find correspondence in the SM puzzle, the baryon asymmetry between matter and anti-matter [19] is only partially justified by CP violation effects.

Therefore, after the Higgs boson observation, the High Energy Physics community focused to carry on additional stringent tests to search for evidence of deviations from the SM, resulting in New Physics (NP), i.e. processes not already included in the SM, that should involve particles with very small or very high masses, with respect to the energy scales now accessible, i.e. few eV (or lower) or tens of TeV (or higher).

Two complementary approaches are followed by accelerator-based experiments to test the SM and to search for NP evidences: the energy and the intensity frontiers. In the first scenario the goal is to increase as much as possible the energy (e.g. energies of colliding protons at LHC) extending the reach for NP particle production, that is the approach used for the Higgs boson discovery. In the second case the goal is to collect as much statistics as possible in order to measure ultra-rare processes, in which a given measured physics quantity (e.g. the branching ratio) could deviate with respect to the SM prediction due to effects of NP.

The intensity frontier approach is the one exploited by the NA62 experiment [20], whose main goal is the measurement of the branching ratio (Br) of the ultra-rare decay $K^+ \to \pi^+ \nu\bar{\nu}$, for which the SM predicts a value of $(0.84 \pm 0.10) \cdot 10^{-10}$, with an uncertainty of the order of 10% [21]. This is one of the golden channels for NP searches, given its precise theoretical prediction and the presence of several NP models that allow significant deviations from the SM prediction for the value of the branching ratio [22] [23] [24] [25] [26] [27] [28] [29] [30] [31] [32].

The NA62 experiment has collected data at the CERN SPS from 2016 to 2018. The data recorded in 2016 and 2017 have been analyzed, achieving the $K^+ \to \pi^+ \nu\bar{\nu}$ SM sensitivity [33] [34], but they do not allow to perform a measurement.

I joined the $K^+ \to \pi^+ \nu\bar{\nu}$ *analysis Working Group* during the analysis of the 2017 data. My main contribution was focused on studies to improve the RICH detector performance and to estimate the background originating from kaon decays with positrons in the final state.

The analysis of the 2018 data and the preliminary combined result (2016-2018 data) of the $Br(K^+ \to \pi^+ \nu\bar{\nu})$ measurement are the object of this thesis, since I am one of the people main involved in the full analysis, with particular attention to the improvements with respect to the previous analyses (2016 and 2017 data).

The result has been presented for the first time at the ICHEP 2020 Conference [35] and then I presented it in a seminar organized by the Experimental Physics Department of CERN [36] in October 2020. The paper with the final result is in preparation.

The thesis is organized as follows. The first chapter is dedicated to the description of the theoretical framework of the $K^+ \to \pi^+ \nu\bar{\nu}$ process in the Standard Model and beyond, and to the experimental state of the art. In the second chapter the NA62 experiment is described. Chapters 3, 4 and 5 illustrate the signal and the normalization selections, the measurement of the Single Event Sensitivity and background contamination, while the sixth chapter is dedicated to the result of the $Br(K^+ \to \pi^+ \nu\bar{\nu})$ measurement.

During my PhD, I was also involved in the study of the $K^+ \to \pi^0 e^+ \nu\gamma$ decay, started for my Master thesis project and now close to be finalized. For this study I developed a new algorithm for the fine calibration of the energy measured in the electromagnetic calorimeter LKr. This activity is described in Appendix A.

Perugia (Italy), December 2020.

Chapter 1

The $K^+ \to \pi^+\nu\bar{\nu}$ decay in the Standard Model and beyond

The K mesons (kaons) have always played a key role in the development of models to understand fundamental interactions, starting from their discovery in 1947 [37] and moving, for instance, to the first experimental evidence of CP symmetry violation in weak interactions with the famous experiment by Christenson and colleagues in 1964 [38].

Nowadays, experimental studies of K mesons at high intensities can still be of uppermost importance for the indirect search of New Physics beyond the Standard Model.

At the LHC we are now able to test the presence of new particles with masses no greater then few TeV. That is why the indirect search of NP is the only way to reach the level tens of TeV or more.

One of the best theoretical environment for indirect search of NP is given by the *flavor physics sector*, in particular with processes involving strange and beauty quarks. Therefore the kaon physics programme, that involves the strange quark, is complementary to the physics of the heavy flavors explored, for example, with the LHCb [39] and the Belle II [40] experiments.

In particular, a golden probe of the SM is represented by the ultra-rare decay $K^+ \to \pi^+\nu\bar{\nu}$, together with the neutral partner $K_L \to \pi^0\nu\bar{\nu}$ that are described in this chapter.

1.1 Quark mixing and GIM mechanism

In the theory of weak interactions, a fundamental role is played by the quark mixing initially proposed by Cabibbo [41], since it is able to recover the universality of the weak interaction also in the quark sector: in fact he realized that the weak eigenstates of the known quarks with charge $-1/3$ are not the mass eigenstates d and s, but a linear combination, of them, rotated by an angle θ:

$$d' = d\cos\theta + s\sin\theta \tag{1.1}$$

The Cabibbo model has been applied by Glashow, Iliopoulos and Maiani [42], in the so called *GIM mechanism*, in order to explain the suppression of particular processes, as the *Flavor Changing Neutral Current (FCNC)* processes, or for example the $K_L \to \mu^+\mu^-$ decay, whose branching fraction is experimentally observed to be smaller than 10^{-8} [43]. They postulated the existence of a new up-like quark, the charm, following the indirect experimental evidence that $\Delta S = 2$ transitions were strongly disfavoured with respect to processes with $\Delta S = 1$. Therefore in the $K_L \to \mu^+\mu^-$ decay there are two main contributions to the decay amplitude, as shown in Figure 1.1.

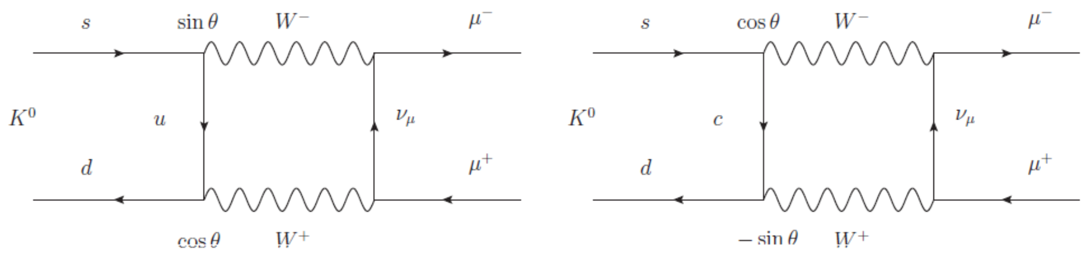

Figure 1.1: Two contributions to the $K_L \to \mu^+\mu^-$ decay: up quark (left) and charm quark (right).

Applying the Cabibbo theory, both diagrams amplitudes are proportional to $\sin\theta\cos\theta$, but have opposite signs and cancel. However, the cancellation is not perfect due to the mass difference between the up and the charm quarks and the residual amplitude is different from 0, but heavily suppressed.

1.2 CKM theory

The $K^+ \to \pi^+\nu\bar{\nu}$ decay is strongly related to the Cabibbo-Kobayashi-Maskawa (CKM) matrix of weak interactions, introduced for the first time in 1973 [44].

The CKM matrix, shown in Equation 1.2, connects the quark flavor eigenstates to those of the weak interaction, determining also the probability of transition between different quark flavors, thus generalizing the Cabibbo theory.

$$\begin{pmatrix} d' \\ s' \\ b' \end{pmatrix}_{weak} = \begin{pmatrix} V_{ud} & V_{us} & V_{ub} \\ V_{cd} & V_{cs} & V_{cb} \\ V_{td} & V_{ts} & V_{tb} \end{pmatrix} \times \begin{pmatrix} d \\ s \\ b \end{pmatrix}_{flavor} = V_{CKM} \times \begin{pmatrix} d \\ s \\ b \end{pmatrix}_{flavor} \tag{1.2}$$

The standard formulation of the weak interaction provides a mixing between quarks of down-type (d, s, b), leaving the up-type unmixed, but this is an arbitrary choice due to the fact that Cabibbo originally proposed quark mixing when only up, down and strange quarks were known.

The main characteristic of the CKM matrix is the unitarity, that directly follows from the weak interaction universality assumption. This is why the experimental confirmation of CKM matrix unitarity represents one of the most stringent test for the Standard Model.

Even if the CKM matrix contains 9 complex numbers, the unitarity requirement and gauge invariance reduce the number of free parameters to 4: three mixing angles and a complex phase, that leads to the CP simmetry violation in the Standard Model.

Taking into account the experimental values of the CKM elements, it can be useful to represent the CKM matrix using the Wolfenstein parametrization [45], generated by the 4 parameters λ, A, ρ, η defined as follows:

$$\lambda = \frac{|V_{us}|}{\sqrt{|V_{ud}|^2 + |V_{us}|^2}} \tag{1.3}$$

$$A = \frac{|V_{cb}|}{\lambda^2\sqrt{|V_{ud}|^2 + |V_{us}|^2}} \tag{1.4}$$

$$\rho = \frac{Re(V_{ub})}{A\lambda^3} \tag{1.5}$$

$$\eta = \frac{Im(V_{ub})}{A\lambda^3} \tag{1.6}$$

In this parametrization each matrix term is expanded as a power series in the parameter $\lambda \simeq |V_{us}| = 0.2243 \pm 0.0005$ [43], and thanks to its small value, only the first therms of the expansion are non-negligible (Equation 1.7). With this parametrization the hierarchy of the CKM elements, therefore the transition probability between quarks in the weak interactions, is evident.

$$V_{CKM} = \begin{pmatrix} 1 - \frac{\lambda^2}{2} & \lambda & A\lambda^3(\rho - i\eta) \\ -\lambda & 1 - \frac{\lambda^2}{2} & A\lambda^2 \\ A\lambda^3(1 - \rho - i\eta) & -A\lambda^2 & 1 \end{pmatrix} + \mathcal{O}(\lambda^4) \tag{1.7}$$

The unitarity of CKM matrix leads to the following conditions:

$$\sum_i V_{ij}V^*_{ik} = \delta_{jk} \ , \ \sum_j V_{ij}V^*_{kj} = \delta_{ik} \tag{1.8}$$

The six vanishing combinations can be represented as triangles in a complex plane, of which those obtained by taking scalar products of neighboring rows or columns are nearly degenerate. The most common triangle is the one derived from

$$V_{ud}V^*_{ub} + V_{cd}V^*_{cb} + V_{td}V^*_{tb} = 0 \tag{1.9}$$

dividing by $V_{cd}V^*_{cb}$, the best measured elements, as shown in Figure 1.2. It is represented in the $(\bar{\rho}, \bar{\eta})$ plane, where $\bar{\rho}$ and $\bar{\eta}$ are equivalent to the Wolfenstein parameters, defined as follows:

$$\bar{\rho} = \rho\left(1 - \frac{\lambda^2}{2} + \mathcal{O}(\lambda^4)\right) \tag{1.10}$$

$$\bar{\eta} = \eta\left(1 - \frac{\lambda^2}{2} + \mathcal{O}(\lambda^4)\right) \tag{1.11}$$

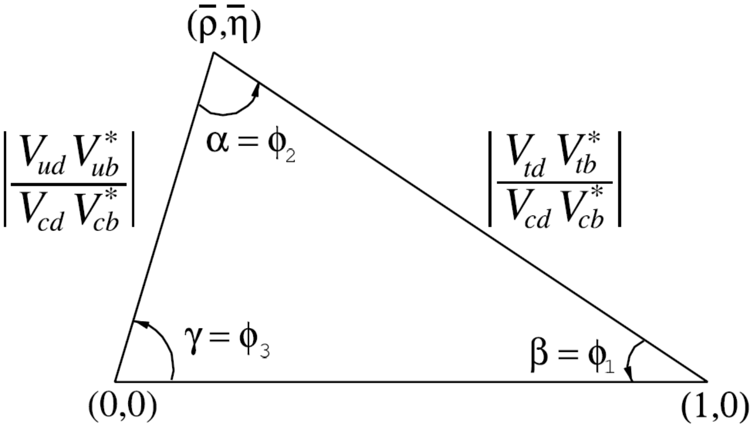

Figure 1.2: The CKM unitarity most common triangle.

The current fitted values for the Wolfenstein parameters are [43]:

$$\lambda = 0.22453 \pm 0.00044 \ , \ A = 0.836 \pm 0.015 \ , \tag{1.12}$$

$$\bar{\rho} = 0.122^{+0.018}_{-0.017} \ , \ \bar{\eta} = 0.355^{+0.012}_{-0.011} \ . \tag{1.13}$$

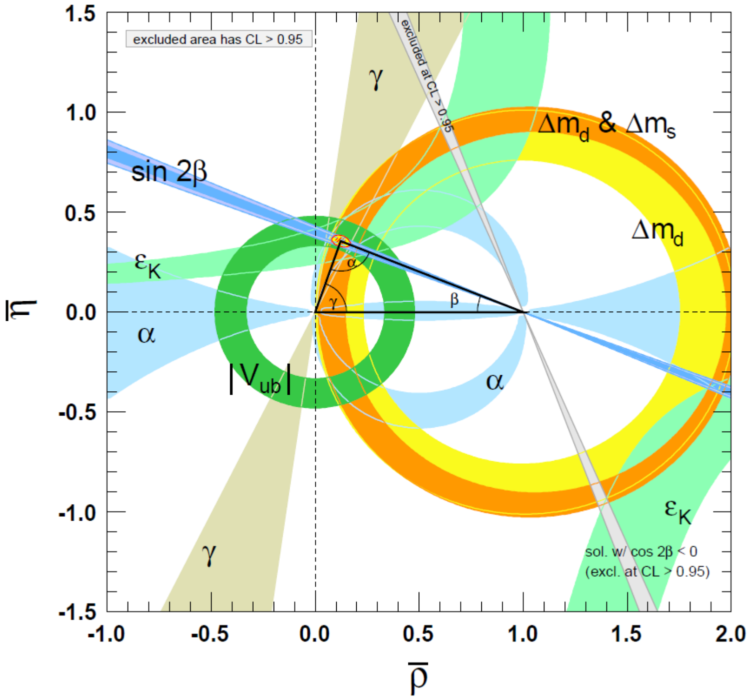

Figure 1.3: Constraints on the$(\bar{\rho}, \bar{\eta})$ plane. The shaded areas have 95% CL. Figure from [43].

Figure 1.3 illustrates the constraints on the $(\bar{\rho}, \bar{\eta})$ plane from various measurements and the global fit results obtained in [43]. No experimental deviation from the unitarity condition has emerged.

In the kaon sector, a very clean test of the SM can be performed measuring $K^+ \to \pi^+\nu\bar{\nu}$ and $K_L \to \pi^0\nu\bar{\nu}$, since these rare decays are sensitive to New Physics, and will allow a determination of β, independent of its value measured in B decays [46].

1.3 $K^+ \to \pi^+\nu\bar{\nu}$ decay in the Standard Model

The $K^+ \to \pi^+\nu\bar{\nu}$ decay is a *FCNC* process, whose amplitude is given by the Z^0 penguin and box diagrams shown in Figure 1.4, with the transition $s \to d\nu\nu$, not allowed at tree level in the Standard Model.

In each diagram, all the three up-like quarks (u,c,t) can run in the loops, therefore each diagram amplitude is the sum of three different contributions. Due to the quadratic GIM mechanism, the amplitude of the contributions of an up-like quark

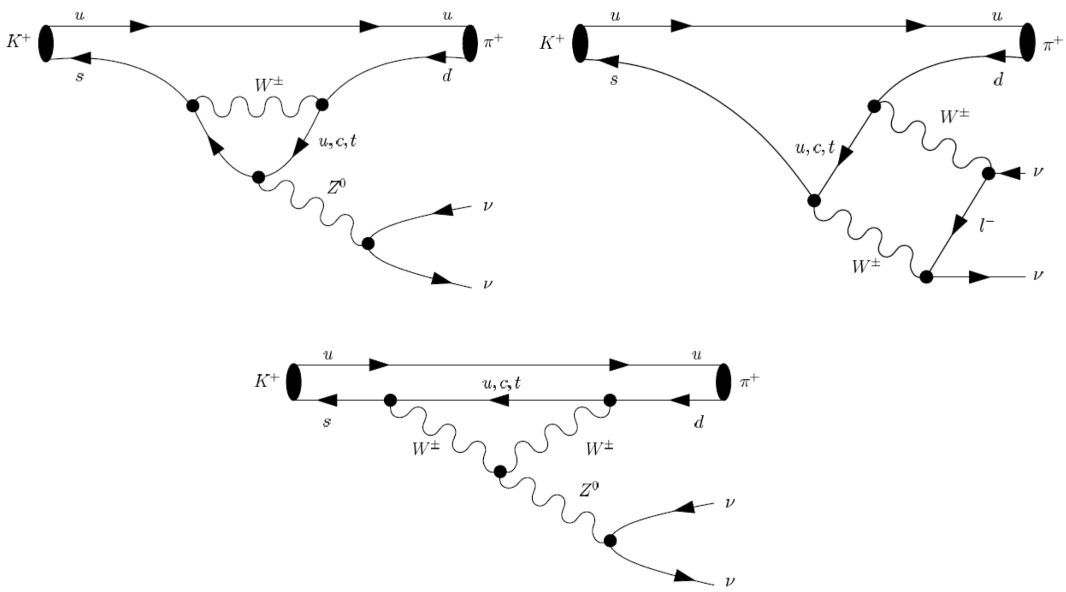

Figure 1.4: The penguin and box diagrams contributing the $K^+ \to \pi^+ \nu\bar{\nu}$ decay. Figure from [47].

running in the loops can be approximately written as:

$$A_q \simeq \frac{m_q^2}{m_W^2} V_{qs}^* V_{qd} \tag{1.14}$$

It is quite evident that diagrams containing an up quark are strongly suppressed: the amplitude will be dominated by the top quark contribution. Loops with a charm quark provide a small but non-negligible contribution to the total decay rate. Whereby the decay is largely dominated by top quark exchange: the mixture of quadratic GIM mechanism and the small value of the CKM element V_{td} describing the transition of a top into a down quark, makes this process extremely rare.

The dependence on the charged lepton mass resulting from the box diagrams is negligible for the top contribution, while for the charm this is the case only for the electron and the muon but not for the τ lepton.

Then summing up over all the three neutrino flavors gives the final formula for the $K^+ \to \pi^+ \nu\bar{\nu}$ branching ratio [21], with the derivation details in [48]:

$$Br(K^+ \to \pi^+ \nu\bar{\nu}) = k_+(1 + \Delta_{EM}) \cdot \left[\left(\frac{Im\lambda_t}{\lambda^5} X(x_t) \right)^2 + \left(\frac{Re\lambda_c}{\lambda} P_c(X) + \frac{Re\lambda_t}{\lambda^5} X(x_t) \right)^2 \right] \tag{1.15}$$

$$k_+ = (5.173 \pm 0.025) \cdot 10^{-11} \left[\frac{\lambda}{0.225}\right]^8 \ , \ \Delta_{EM} = -0.003 \tag{1.16}$$

where:

- k_+ (and its electromagnetic correction Δ_{EM}) summarizes the hadronic contributions, that can be extracted experimentally from semi-leptonic decays $K^+ \to \pi^0 l^+ \nu$ $(l = e, \mu)$ using the isospin symmetry between π^+ and π^0 [49]. This is one of the crucial aspects that strongly improves the theoretical uncertainty.
- $X(x_t)$ is the loop function that represents the top quark contribution, with $x_t = m_t^2/m_W^2$. Its most recent value, including two-loop electroweak corrections [50] and NLO QCD corrections [51], is $X(x_t) = 1.481 \pm 0.005 \pm 0.008$ [21].
- $P_c(X)$ is the loop function representing the charm quark contribution. It can be written as $P_c(X) = P_c^{SD}(X) + \delta P_{c,u}$. $P_c^{SD}(X) = 0.365 \pm 0.012$ is the short-distance contribution, computed in [21], applying most recent input parameter to the formula given in [52] . $\delta P_{c,u} = 0.04 \pm 0.02$ is the long-distance contribution calculated in [53].
- $\lambda = |V_{us}|$ and $\lambda_q = V_{qs}^* V_{qd}$ are the factors related to the CKM matrix elements for the involved quarks.

Inserting the most recent values for the CKM matrix elements in Equation 1.15 leads to the final computation of $Br(K^+ \to \pi^+\nu\bar{\nu})$ in the Standard Model framework [21]:

$$Br^{SM}(K^+ \to \pi^+\nu\bar{\nu}) = (0.84 \pm 0.10) \cdot 10^{-10} \tag{1.17}$$

The achieved precision on the computation of high order QCD and electroweak corrections makes the $K^+ \to \pi^+\nu\bar{\nu}$ decay one the most precisely computed FCNC processes involving quarks in the Standard Model.

In order to better understand the single contributions to the global uncertainty, that is around 10%, it is useful to factorize the expression in Equation 1.15 as follows [21]:

$$Br(K^+ \to \pi^+\nu\bar{\nu}) = (0.839 \pm 0.030) \cdot 10^{-10} \cdot \left[\frac{|V_{cb}|}{40.7 \cdot 10^{-3}}\right]^{2.8} \cdot \left[\frac{\gamma}{73.2^\circ}\right]^{0.74} \tag{1.18}$$

where γ is the angle of the unitarity triangle represented in Figure 1.2.

A representation of the single contributions to the global uncertainty is given in Figure 1.5.

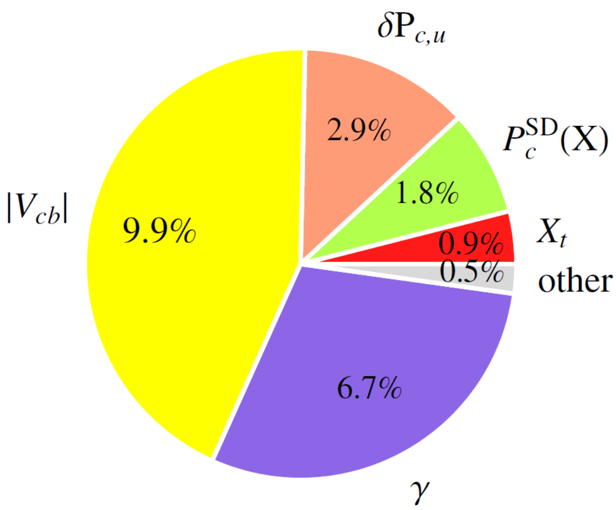

Figure 1.5: Error budget for the theoretical calculation of the $Br(K^+ \to \pi^+\nu\bar{\nu})$ observable. Figure from [21].

The only theoretical uncertainty, smaller than 4% is due to poor knowledge of the long-distance $\delta P_{c,u}$ contribution that amounts to about 3%. The global uncertainty is dominated by the knowledge of the CKM parameters V_{cb} and γ.

With similar considerations also the branching ratio of the $K_L \to \pi^0\nu\bar{\nu}$ decay (that is described by the same Feynman diagrams in Figure 1.4, where the spectator quark is changed from up to down) is computed in [21]:

$$Br^{SM}(K_L \to \pi^0\nu\bar{\nu}) = (0.34 \pm 0.06) \cdot 10^{-10}. \tag{1.19}$$

The combined measurements of both these branching ratios would be able to provide the determination of two elements of the unitarity triangle as shown in Figure 1.6.

The measurement of the neutral channel allows to directly extract the height of the unitarity triangle: it is a CP-violating process and only the imaginary part of the decay amplitude is involved.

The charged channel, instead, receives contributions by both the imaginary and the real component of the decay amplitude. The imaginary part is the same as for the neutral channel, while the real part is provided by the top, within the unitarity triangle, and by the charm. The $K^+ \to \pi^+\nu\bar{\nu}$ decay provides, therefore, the measurement of one side of the unitarity triangle, after the correction for the charm contribution.

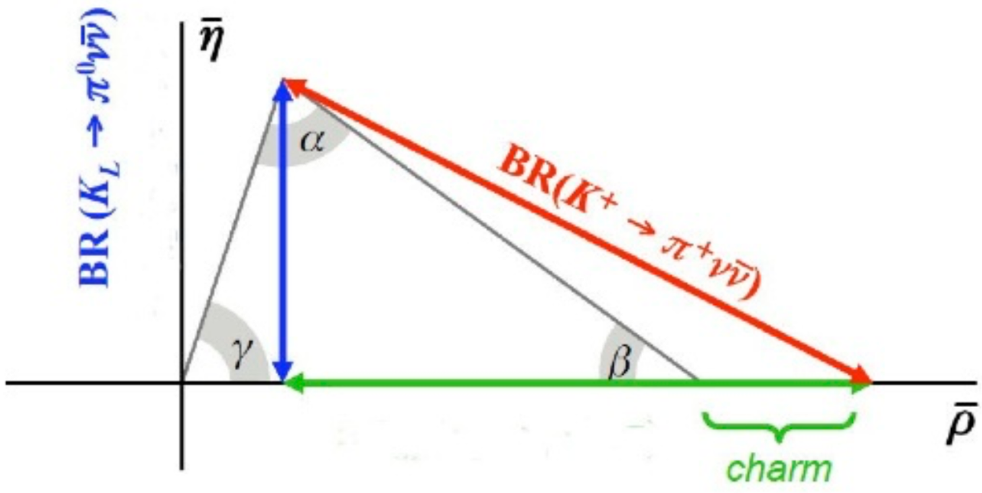

Figure 1.6: Relations between the unitarity triangle and the $K \to \pi\nu\bar{\nu}$ decays.

1.4 $K \to \pi\nu\bar{\nu}$ decays beyond the Standard Model

Several models Beyond the Standard Model (BSM) predict large deviations in the branching fraction of both charged and neutral channels of the $K \to \pi\nu\bar{\nu}$ decays, involving NP particles running in the diagram loops.

The largest deviations from the SM are expected in models with new sources of flavor violation, with weaker B physics constraints [22] [23].

The experimental value of the CP violation parameter ϵ_k limits the expected $Br(K^+ \to \pi^+\nu\bar{\nu})$ range within models with currents of defined chirality, producing specific correlation patterns between the $K^+ \to \pi^+\nu\bar{\nu}$ and $K_L \to \pi^0\nu\bar{\nu}$ branching fractions. An example are the models reviewed in [24], with a new heavy gauge boson Z' generating FCNC processes at tree level. In the most general case it is possible to predict the correlations between $K^+ \to \pi^+\nu\bar{\nu}$ and $K_L \to \pi^0\nu\bar{\nu}$ decays for different values of the Z' boson mass and couplings $\Delta_{L,R}$; the same correlation can be found applying models obeying Constrained Minimal Flavor Violation (CMFV), as shown in Figure 1.7.

Some other models rely on different kind of constraints: as an example, the correlation between $K^+ \to \pi^+\nu\bar{\nu}$ and $B_d \to K^*\nu\bar{\nu}$ is shown in Figure 1.8 for a simplified Z model and a 5 TeV Z' model, imposing CMFV and constraint from B physics [24].

A complete review of models involving heavy gauge bosons can be found in [25].

Present experimental constraints limit the range of variation of $Br(K^+ \to \pi^+\nu\bar{\nu})$ within supersymmetric models [26] [27] [28].

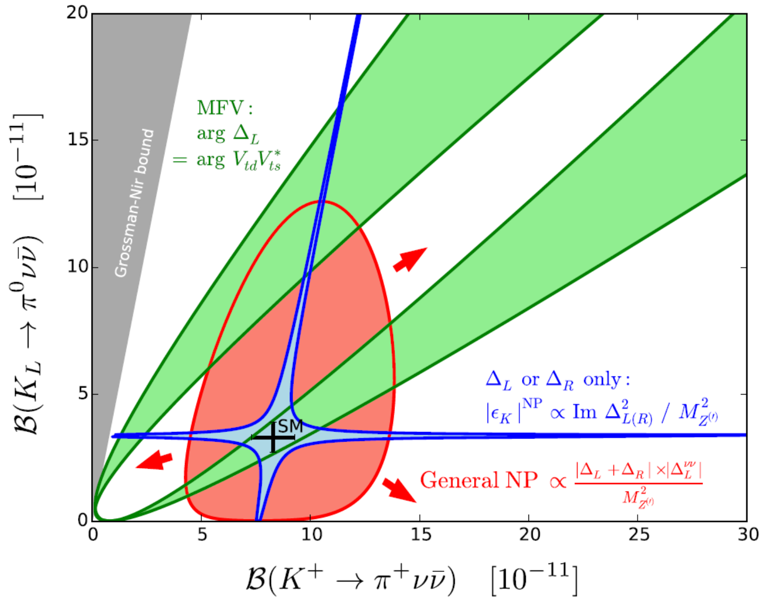

Figure 1.7: Illustrations of common correlations in the $Br(K_L \to \pi^0 \nu\bar{\nu})$ versus $Br(K^+ \to \pi^+ \nu\bar{\nu})$ plane. The expanding red region illustrates the lack of correlation for models with general LH and RH NP couplings of Z' boson. The green region shows the correlation present in models obeying CMFV. The blue region shows the correlation induced by the constraint from ϵ_k if only LH or RH couplings are present. Figure from [24].

The $K^+ \to \pi^+ \nu\bar{\nu}$ decay can also be sensitive to effects of lepton flavor non-universality models [29] [30], which assume that the new physics particles can be coupled only to the third generation of quarks and leptons (Figure 1.9).

Models that include leptoquarks [31] [32] also predict different values for $Br(K^+ \to \pi^+ \nu\bar{\nu})$, therefore its measurement could be able to constrain them.

Finally, it is important to mention that the ratio $Br(K_L \to \pi^0 \nu\bar{\nu})/Br(K^+ \to \pi^+ \nu\bar{\nu})$ shows an upper bound (visible in Figure 1.7) under the assumptions of the lepton flavor conservation and that the underlying interactions change isospin by $\Delta I = 1/2$ [54]:

$$Br(K_L \to \pi^0 \nu\bar{\nu}) < 4.4 \cdot Br(K^+ \to \pi^+ \nu\bar{\nu}) \tag{1.20}$$

This is referred to as the Grossman-Nir (GN) bound, which is respected by the Standard Model and also by many scenarios beyond it. A recent study [55] published in 2020 demonstrates how the inclusion of $\Delta I = 3/2$ operators in New Physics models could lead to a violation of the GN bound.

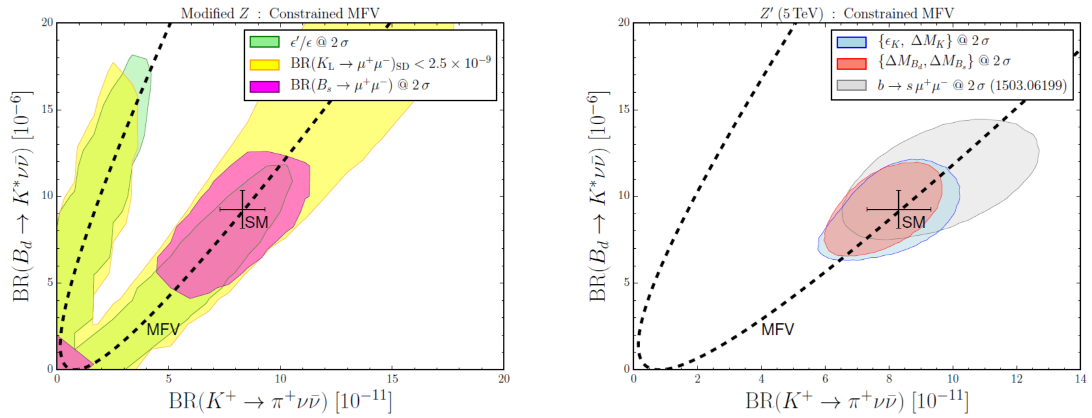

Figure 1.8: Allowed ranges for $Br(B_d \to K^* \nu\bar{\nu})$ versus $Br(K^+ \to \pi^+ \nu\bar{\nu})$ in a simplified Z model (left) and a 5 TeV Z' model (right) obeying CMFV. In the left panel the 2σ confidence regions shown correspond to constraints from ϵ'/ϵ (green), $K_L \to \mu^+\mu^-$ (yellow) and $B_s \to \mu^+\mu^-$ (magenta), while in the right panel they correspond to constraints from kaon mixing (blue), B mixing (red) and $b \to s\mu^+\mu^-$ transitions (grey). Figures from [24].

1.5 Experimental status of $Br(K \to \pi\nu\bar{\nu})$

A recent summary of the experimental status of $Br(K \to \pi\nu\bar{\nu})$ measurements is provided in [56].

Concerning the charged channel, there are two different experimental approaches to this measurement: observing stopped kaon decaying, or using a decay-in-flight technique.

The KEK E10 experiment exploited stopped kaons, with chambers and range counters above a K^+ stopping target to track and distinguish pions from muons based on the deposited energy and range. Using this technique they were able to impose the limit $Br(K^+ \to \pi^+\nu\bar{\nu}) < 1.4 \cdot 10^{-7}$ @ 90% CL [57].

The same technique has been used by the BNL E787 and E949 experiments. They had two stages of electromagnetic separators in the beam to have a high K^+/π^+ ratio. They also had cylindrical range counters and hermetic photon veto detectors to increase the coverage and a magnetic spectrometer was used to measure the momentum of the charged pion. They achieved the SES corresponding to $\simeq 1$ SM event and they observed 7 signal-like events (Figure 1.10), providing the first branching ratio measurement [58] [59]:

$$Br^{BNL}(K^+ \to \pi^+\nu\bar{\nu}) = (1.73^{+1.15}_{-1.05}) \cdot 10^{-10} \tag{1.21}$$

The central value is a factor of 2 higher with respect to the Standard Model

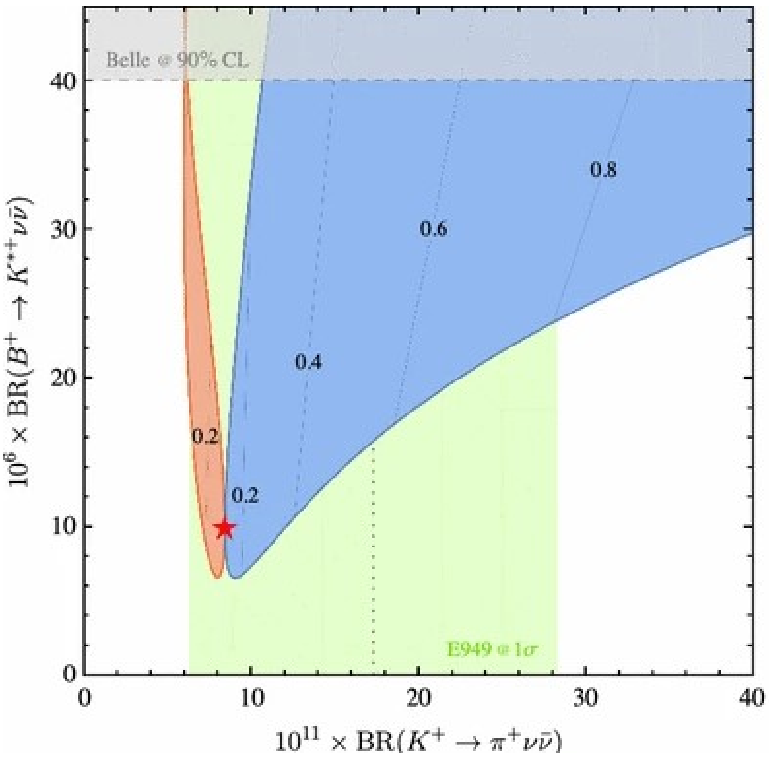

Figure 1.9: Correlation of $Br(K^+ \to \pi^+\nu\bar{\nu})$ with $Br(B^+ \to K^{*+}\nu\bar{\nu})$, having imposed $R_{D^{(*)}} = 1.25$. The red (blue) coloured region is for $c_{13} = 0$ ($c_{13} = 2$), where c_{13} denotes the ratio between the Wilson coefficients of the electroweak singlet and triplet current-current interactions of the NP model. The red star is the SM point. Figure from [29].

prediction (Equation 1.17), but the experimental uncertainty is large and does not indicate any deviation from the Standard Model.

The NA62 experiment has been proposed [20] with the main goal of measuring $Br(K^+ \to \pi^+\nu\bar{\nu})$ with an experimental uncertainty comparable to the theoretical prediction, using a decay-in-flight technique. The NA62 experiment is described in details in the next chapter. It has been operating at the CERN SPS since 2016: data have been recorded in three different runs in 2016, 2017 and 2018. From the 2016-2017 data sets the following results have been obtained [33] [34], based on 3 signal candidates observed (Figure 1.11):

$$Br^{NA62-16-17}(K^+ \to \pi^+\nu\bar{\nu}) = (0.48^{+0.72}_{-0.48}) \cdot 10^{-10} \tag{1.22}$$

$$Br^{NA62-16-17}(K^+ \to \pi^+\nu\bar{\nu}) < 1.78 \cdot 10^{-10} \text{ @ } 90\%\ CL \tag{1.23}$$

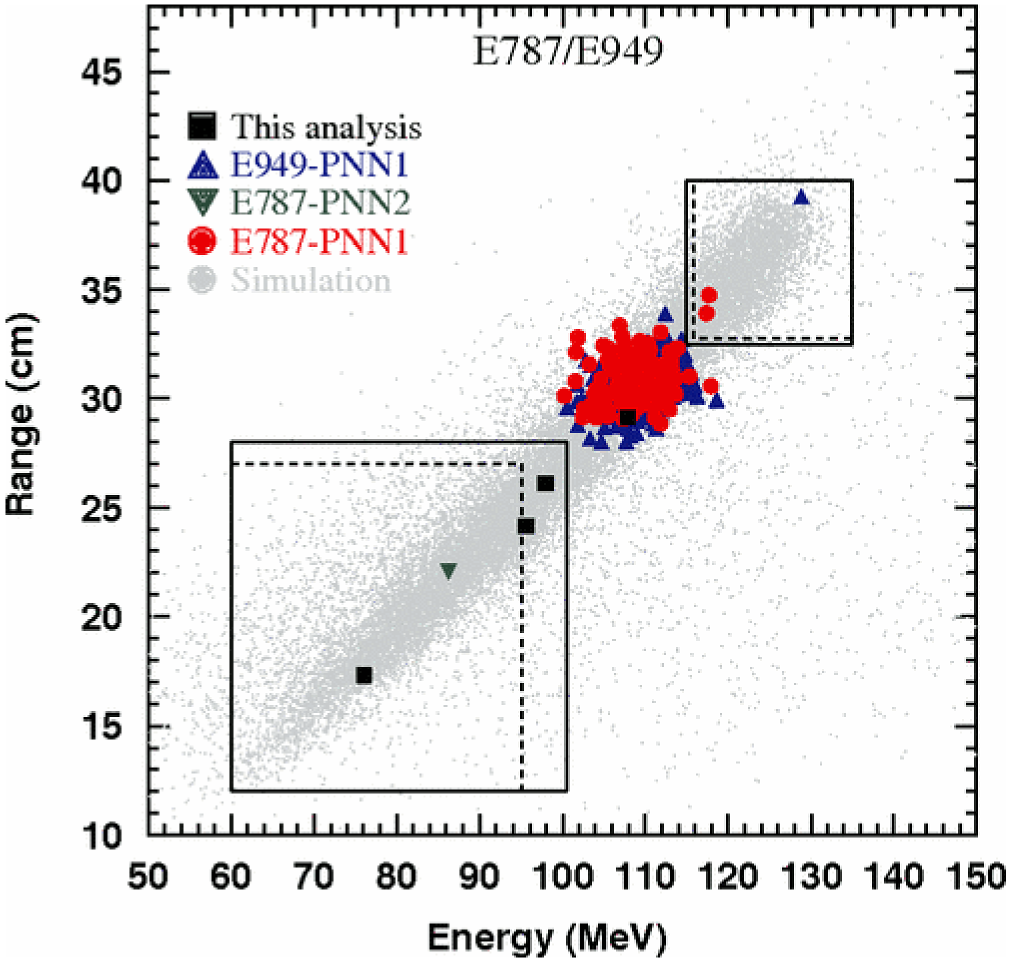

Figure 1.10: Observed $K^+ \to \pi^+\nu\bar{\nu}$ candidates by the BNL E787 and E949 experiments. Figure from [59].

The measurements performed by BNL E787 and E949 experiments and by NA62 are reported in Figure 1.12, together with the theoretical predictions as a function of the year of publication.

The result of the analysis of the full 2016-2018 data-set is the main topic of this thesis, and it will be described in detail in the following chapters.

The neutral channel is currently explored by the KOTO experiment at J-PARC. The KOTO collaboration established an upper limit on $Br(K_L \to \pi^0\nu\bar{\nu})$ with data collected in 2015 (no signal candidates observed) [60]:

$$Br^{KOTO-15}(K_L \to \pi^0\nu\bar{\nu}) < 3.0 \cdot 10^{-9} \text{ @ } 90\% \; CL \tag{1.24}$$

After that the KOTO collaboration provided an update on the search for such decay with the data collected in 2016-2017-2018 runs [61]: with a Single Event

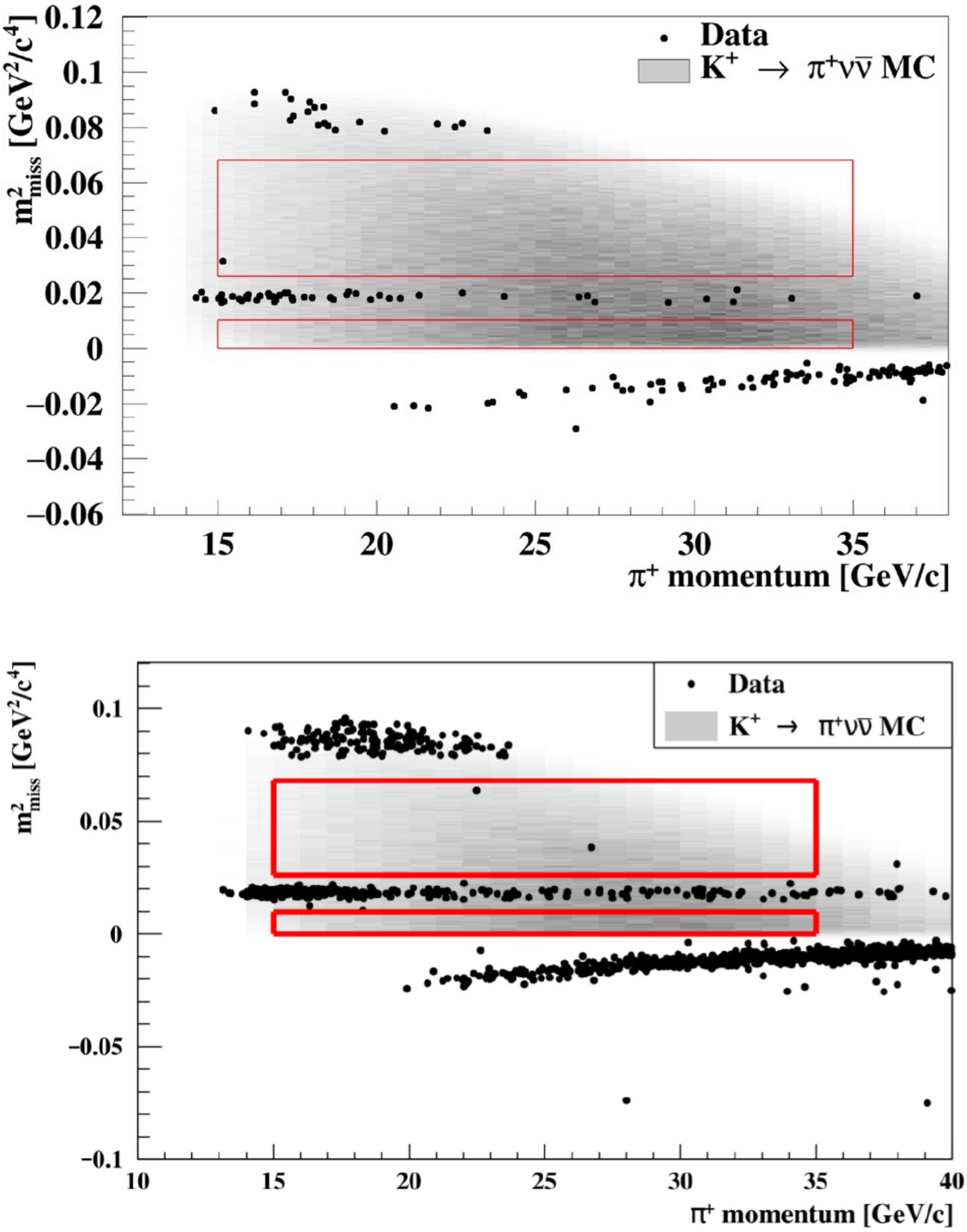

Figure 1.11: Observed $K^+ \to \pi^+\nu\bar{\nu}$ candidates by the NA62 experiment in 2016 (Top) and 2017 (Bottom) data. Figures from [33] and [34].

Sensitivity of $6.9 \cdot 10^{-10}$, corresponding to ~ 0.05 expected Standard Model signal events, and 0.05 ± 0.02 expected background events, they observed 4 signal

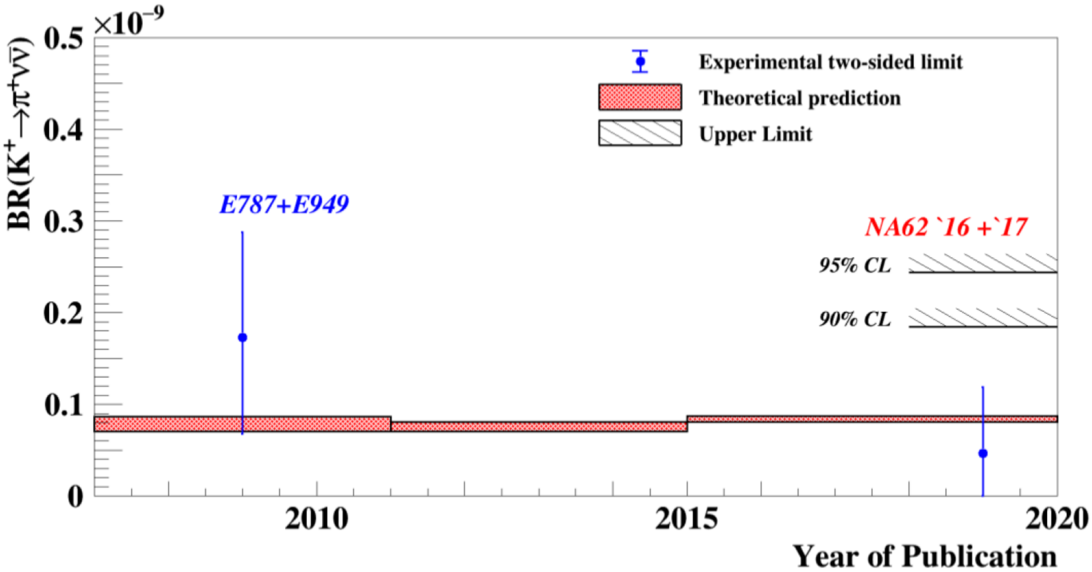

Figure 1.12: Theoretical predictions and experimental measurements of $Br(K^+ \to \pi^+\nu\bar{\nu})$ as a function of the year of publication.

candidates (Figure 1.13), even if one of them has a signature compatible with background. Nevertheless the KOTO collaboration did not provide any branching ratio measurement based on their observations, since further studies of the background sources were needed.

According to a theoretical speculation [62] based on the KOTO observations, a branching ratio measurement is extracted:

$$Br^{speculation}(K_L \to \pi^0\nu\bar{\nu}) = (2.1^{+2.0}_{-1.1}) \cdot 10^{-9} \tag{1.25}$$

The central value is two orders of magnitude above the Standard Model prediction (Equation 1.19) and with the NA62 result (Equation 1.22) could lead to an evidence of Grossman-Nir bound violation, as shown in Figure 1.14.

In a very recent pre-print [63] the KOTO collaboration provided a new estimation of the expected background, according to the analysis of a new source of background. The new number of estimated background events in the 2016-2017-2018 data sample is 1.22 ± 0.26: this new result decreases the discrepancy between expectation and observation, therefore the branching fraction shown in Equation 1.25 is not valid anymore. According to the new background estimation, a new upper limit based on the 2016-2017-2018 data has been set by KOTO [63]:

$$Br^{KOTO-16-17-18}(K_L \to \pi^0\nu\bar{\nu}) < 4.9 \cdot 10^{-9} \text{ @ } 90\% \; CL \tag{1.26}$$

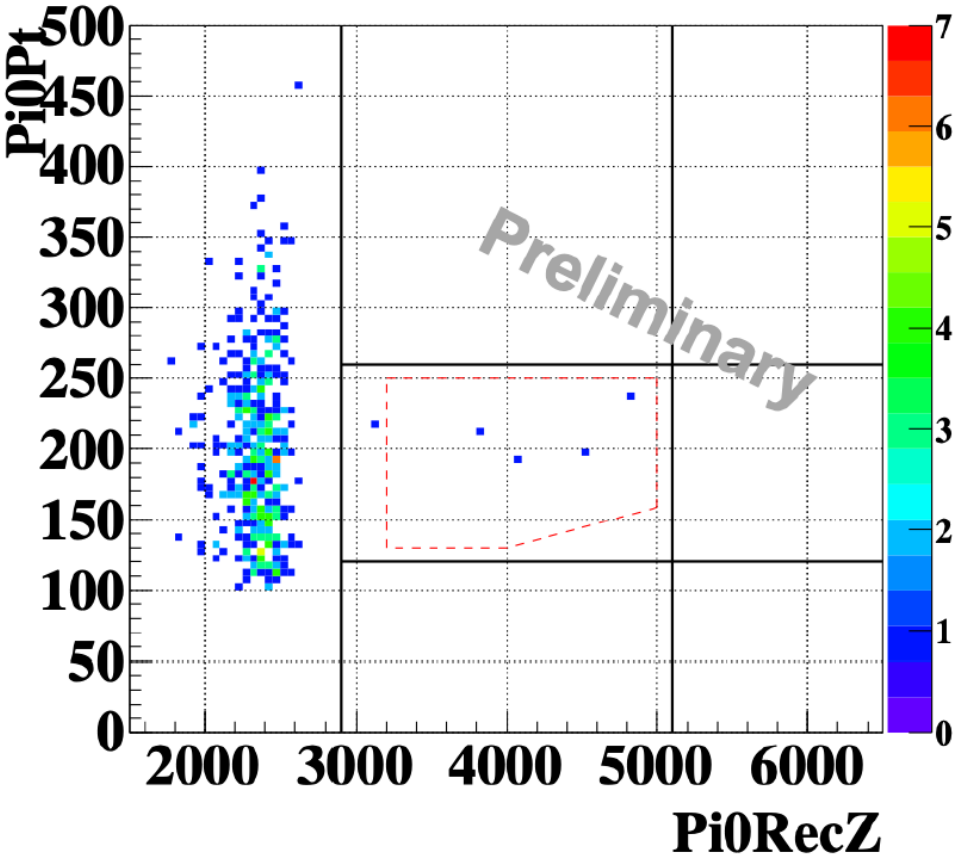

Figure 1.13: Observed $K_L \to \pi^0 \nu\bar{\nu}$ candidates by the KOTO experiment in data collected in 2016-2017-2018 runs. Figure from [61].

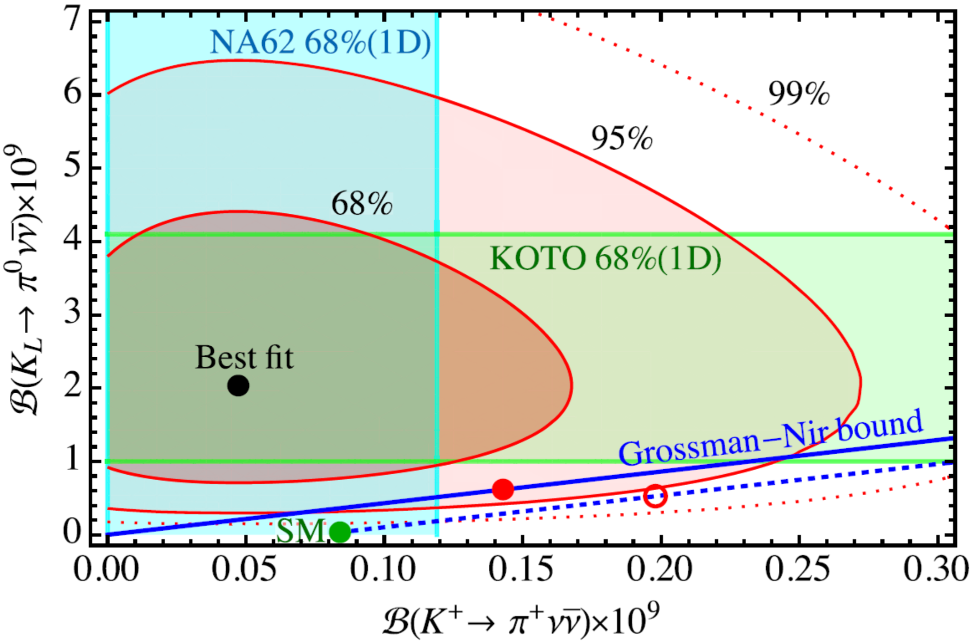

Figure 1.14: $Br^{speculation}(K_L \to \pi^0\nu\bar{\nu})$ of Equation 1.25 and $Br^{NA62-16-17}(K^+ \to \pi^+\nu\bar{\nu})$ of Equation 1.22 are represented by the green and blue bands, respectively. The red ellipses show a simultaneous fits to both. The GN bound with (without) interference with the SM is shown by the solid (dashed) blue line. The red dots are the best fit points on those lines. The green dot is the SM prediction. Only statistical uncertainties are taken into account. Figure from [62].

Chapter 2

The NA62 experiment

This chapter describes the NA62 experiment and its apparatus, built to measure $Br(K^+ \to \pi^+\nu\bar{\nu})$. The physics program of the NA62 experiment also includes the study of other K^+ decays, e.g. [64] [65] [66] [67] [68] [69] [70] and other exotic searches as [71] [72] [73].

A complete description of the NA62 beam and detector is provided in [74] [75] and summarized in [76] [77]. Further details about the recent status of the experiment are available in [78] [79] [80] [81].

2.1 Principles of the experiment

The NA62 experiment is designed to reconstruct positive charged kaons decaying in flight and to detect the products of the decays, with the particular goal of observing the ultra-rare decay $K^+ \to \pi^+\nu\bar{\nu}$, distinguishing it from other possible decay channels of the K^+ meson.

This is very challenging from the experimental point of view, because of the small value expected for the branching fraction and the weak experimental signature, due to the missing information on the $\nu\bar{\nu}$ pair.

The K^+ decay channels that mainly constitute background for the $K^+ \to \pi^+\nu\bar{\nu}$ decay search are reported in Table 2.1, together with the corresponding branching ratios [43], to be compared with $Br^{SM}(K^+ \to \pi^+\nu\bar{\nu}) = (0.84 \pm 0.10) \cdot 10^{-10}$ (Equation 1.17).

Table 2.1 clearly indicates that a measurement of this very rare process calls for extremely high intensity and an experimental apparatus capable of suppressing 10 orders of magnitude backgrounds.

The experimental signature of the $K^+ \to \pi^+\nu\bar{\nu}$ decay is depicted in Figure 2.1: the charged kaon and pion directions in the initial and final state can be reconstructed, together with the measurement of their momenta, while the $\nu\bar{\nu}$ pair

K^+ decay	Br
$K^+ \to \mu^+\nu$	$(63.56 \pm 0.11) \cdot 10^{-2}$
$K^+ \to \pi^+\pi^0$	$(20.67 \pm 0.08) \cdot 10^{-2}$
$K^+ \to \pi^+\pi^+\pi^-$	$(5.583 \pm 0.024) \cdot 10^{-2}$
$K^+ \to \pi^+\pi^- e^+\nu$	$(4.247 \pm 0.024) \cdot 10^{-5}$

Table 2.1: K^+ decay channels, backgrounds for the $K^+ \to \pi^+\nu\bar{\nu}$ decay search, with the corresponding branching ratios [43].

is undetectable, therefore it appears only as missing energy.

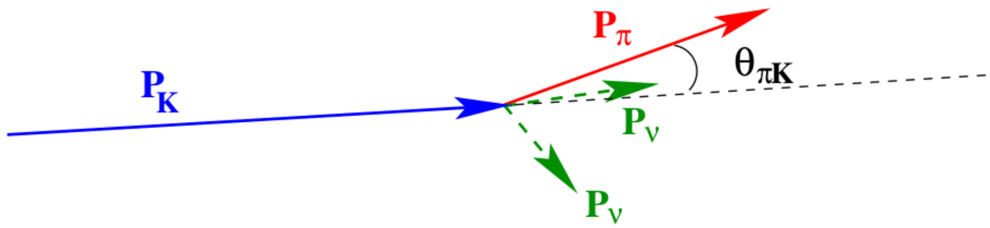

Figure 2.1: Schematic experimental view of the $K^+ \to \pi^+\nu\bar{\nu}$ process.

The NA62 experiment is designed to:

- collect a huge amount of K^+ decays, in order to have enough statistics to surpass the $K^+ \to \pi^+\nu\bar{\nu}$ Standard Model sensitivity;
- precisely reconstruct the $K^+ \to \pi^+\nu\bar{\nu}$ decay kinematics, measuring the momenta of the charged kaon and the charged pion;
- distinguish the charged pion with respect to other charged particles produced in K^+ decays (muons and electrons);
- detect any other possible K^+ decay product not compatible with the $K^+ \to \pi^+\nu\bar{\nu}$ decay, e.g. photons.

Meeting all these requirements will allow the NA62 experiment to collect a sample of $K^+ \to \pi^+\nu\bar{\nu}$ decays, keeping the background contamination from other processes under control, in order to perform the $Br(K^+ \to \pi^+\nu\bar{\nu})$ measurement.

The main variable used for the kinematic reconstruction is the *squared missing mass*:

$$m^2_{miss} = (P_K - P_\pi)^2 \tag{2.1}$$

where P_K (P_π) is the measured charged kaon (pion) four-momentum.

The distribution of the m^2_{miss} variable for the $K^+ \to \pi^+\nu\bar{\nu}$ decay and for the main K^+ decay channels, obtained with Monte Carlo (MC) simulation, is shown in Figure 2.2.

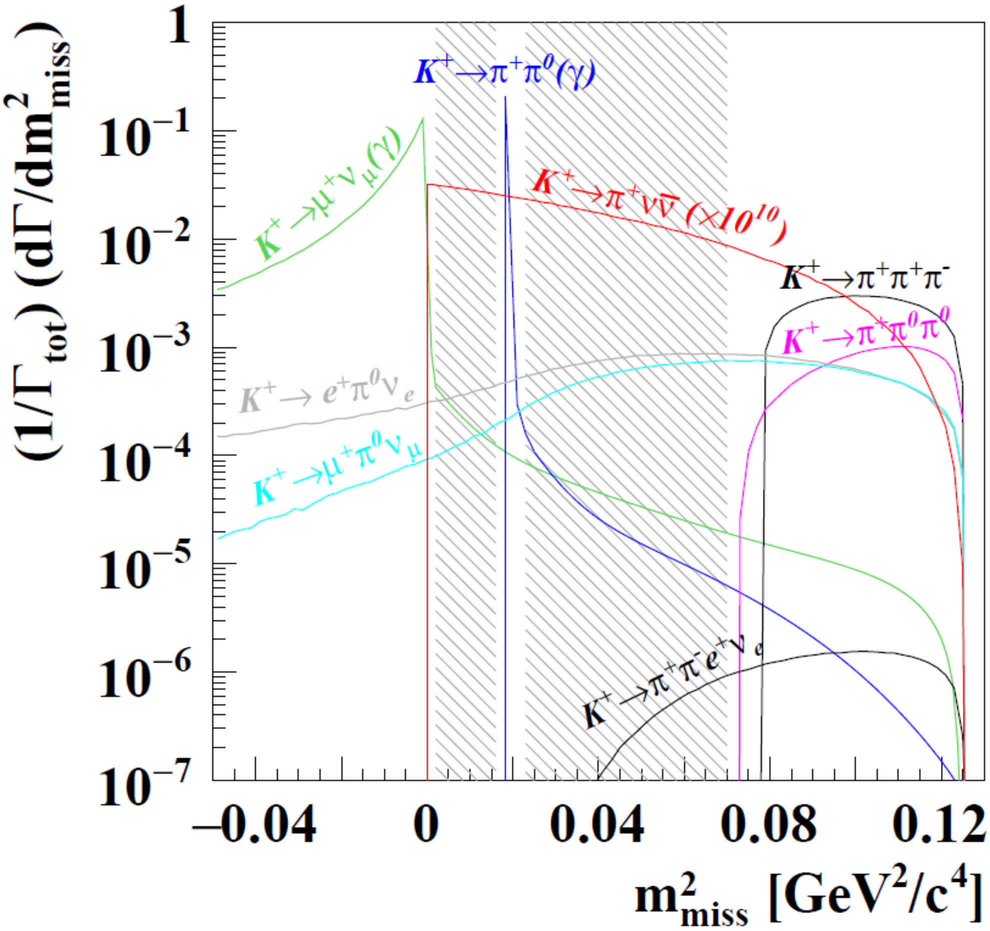

Figure 2.2: Expected theoretical distributions of the m^2_{miss} variable before applying acceptance and resolution effects, for different K^+ decay channels. The $K^+ \to \pi^+\nu\bar{\nu}$ decay channel (red line) is multiplied by 10^{10} for visibility. The hatched areas include the signal regions. Figure from [34].

2.2 NA62 apparatus: a global view

NA62 is a fixed target experiment installed in the CERN North Area, along a proton beam line extracted from the CERN Super Proton Synchrotron (SPS) accelerator (Figure 2.3).

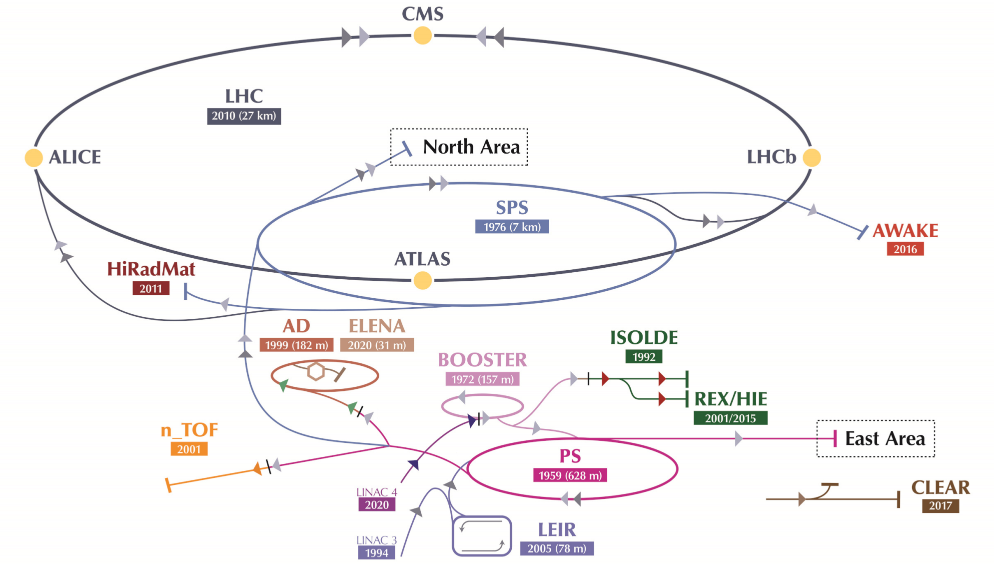

Figure 2.3: Scheme of the CERN accelerators complex. The beam line extracted from the SPS that is exploited by the North Area experiments, as NA62, is also shown.

A schematic view of the NA62 apparatus is represented in Figure 2.4.

The kaon production target is a 40-cm long beryllium rod: a 400-GeV proton beam extracted from the SPS impinges on the target in spills of three seconds effective duration. Typical intensities during data taking range from 1.7 to 1.9×10^{12} protons per pulse (*ppp*). The resulting secondary hadron beam of positively charged particles is comprised of 70% π^+, 23% protons, 6% K^+, $< 1\%$ μ^+, with a nominal momentum of 75 GeV/c (1% rms momentum bite).

Beam particles are characterized by a differential Cherenkov counter (KTAG) and a three-station silicon pixel array (Gigatracker, GTK). The KTAG uses N_2 gas at 1.75 bar pressure (contained in a 5-m long vessel) and is read out by photomultiplier tubes grouped in eight sectors. It tags incoming kaons with 70 ps time resolution. The GTK stations are located before, between, and after two pairs of dipole magnets (a beam achromat), forming a spectrometer that measures beam particles momentum, direction, and time with resolutions of 0.15 GeV/c, 16 μrad and 100 ps, respectively. The typical beam particle rate at the third GTK station (GTK3) is about 450 MHz.

This last station is immediately preceded by the final collimator.

GTK3 marks the beginning of a 117 m-long vacuum tank. The first 80 m of the tank define a fiducial volume (FV) in which 13% of the kaons decay. The beam has a rectangular transverse profile of 52 $\times$ 24 mm^2 and a divergence of 0.11 mrad (rms) in each plane at the FV entrance.

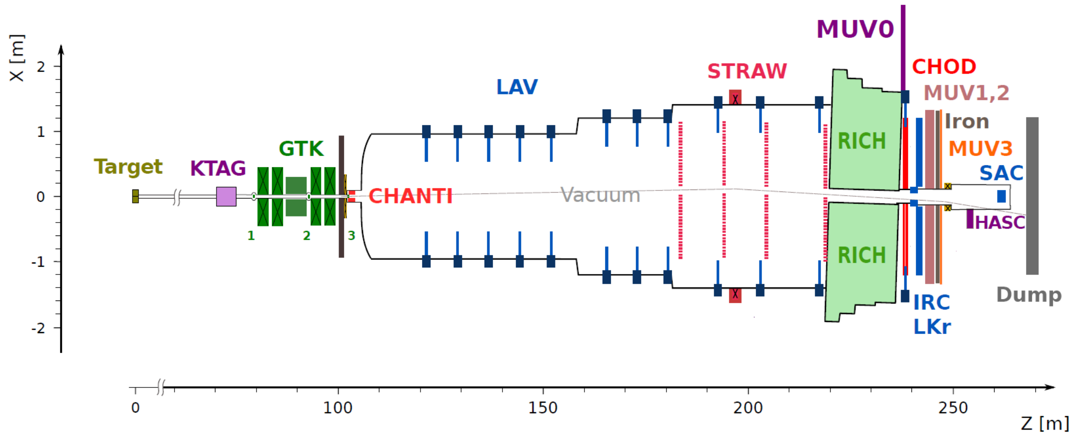

Figure 2.4: Schematic top view of the NA62 beam line and detector. See the text for the description of the sub-detectors. The final fixed collimator installed in 2018 is visible, between GTK and CHANTI. Dipole magnets are displayed as boxes with superimposed crosses. The grey line shows the trajectory of an un-decayed beam crossing the experiment in vaccum and avoiding interactions with detector materials. A dipole magnet between MUV3 and SAC deflects the charged particles of the beam out of the SAC acceptance. The beam line defines the Z-axis of the experiment's right-handed laboratory coordinate system. The origin is the kaon production target and beam particles travel in the positive Z-direction. The Y-axis is vertical (positive up) and the X-axis is horizontal (positive left). Figure from [80].

The time, momentum and direction of charged particles produced by kaon decays-in-flight are measured by a magnetic spectrometer (STRAW), a ring-imaging Cherenkov counter (RICH) and two scintillator hodoscopes (CHOD and New-CHOD). The STRAW, comprised of two pairs of straw chambers on either side of a dipole magnet, measures momentum-vectors with a resolution of σ_p/p between 0.3% and 0.4%. The RICH, filled with neon at atmospheric pressure, tags the decay particles with a timing precision of better than 100 ps and provides particle identification. The NewCHOD, a matrix of tiles read out by SiPMs, and the CHOD, composed of two orthogonal planes of scintillating slabs reused from the NA48 experiment [82], are used for triggering and timing, providing a time measurement with 200 ps resolution.

Other sub-detectors suppress decays involving photons or multiple charged particles (electrons, pions or muons) or provide complementary particle identification. Six stations of plastic scintillator bars (CHANTI) detect, with 99% efficiency and 1 ns time resolution, extra activity, including inelastic interactions in GTK3. Twelve stations of ring-shaped electromagnetic calorimeters (LAV1 to LAV12), made of lead-glass blocks, surround the vacuum tank and downstream sub-detectors to achieve hermetic acceptance for photons emitted by K^+ decays in the FV at polar angles between 10 and 50 mrad. A 27 radiation-length thick, quasi-homogeneous liquid krypton electromagnetic calorimeter (LKr) detects photons from K^+ decays emitted at angles between 1 and 10 mrad. The LKr also complements the RICH for particle identification. Its energy resolution in NA62 conditions is $\sigma_E/E = 1.4\%$ for energy deposits of 25 GeV. Its spatial and time resolutions are 1 mm and between 0.5 and 1 ns, respectively, depending on the amount and type of energy released. Two hadronic iron/scintillator-strip sampling calorimeters (MUV1,2) and an array of scintillator tiles located behind 80 cm of iron (MUV3) supplement the pion/muon identification system. MUV3 has a time resolution of 400 ps. A lead/scintillator shashlik calorimeter (IRC) located in front of the LKr, covering an annular region between 65 and 135 mm from the Z axis, and a similar detector (SAC) placed on the Z axis at the downstream end of the apparatus, ensure the detection of photons down to zero degrees in the forward direction. Additional counters (MUV0, HASC) installed at optimized locations provide nearly hermetic coverage for charged particles produced in multi-track kaon decays.

All detectors are read out with TDCs, except for LKr and MUV1, 2, which are read out with 14-bit FADCs. The IRC and SAC are read out with both. All TDCs are mounted on custom-made (TEL62) boards, except for GTK and STRAW, which each have specialized TDC boards. TEL62 boards both read out data and provide trigger information. A custom electronic chain interprets calorimeter signals for triggering. A dedicated board combines logical signals (primitives) from the RICH, CHOD, NewCHOD, LKr, LAV and MUV3 into a low-level trigger (L0) whose decision is dispatched to sub-detectors for data readout [83]. A software trigger (L1) exploits reconstruction algorithms similar to those used offline with data from KTAG, LAV and STRAW to further cull the data before storing it on disk [75].

The analysis also uses data taken with a minimum-bias L0 trigger (control trigger), based on CHOD information downscaled by a factor of 400, to measure the kaon flux and for other studies as the trigger efficiency measurement or the background estimation.

2.3 Kaon beam

The primary proton beam is extracted at 400 GeV/c from the CERN SPS accelerator and directed to a 400 mm long, 2 mm diameter beryllium target (T10), located in a tunnel connecting the SPS to the underground experimental hall. During a SPS spill of about 3 s effective duration a secondary beam is created from the interaction of the protons with the T10 target at 0 production angle. The particle rate in the NA62 positive secondary hadron beam (K12) is 750 MHz, of which about 6% is from K^+, leading to around 5 MHz of K^+ decays in the 65 m long decay region.

The K12 beam line, shown in Figure 2.5, follows the T10 target and is devoted to the charge and momentum selection of the secondary hadron beam. A 95 cm long copper-collimator, with selectable hole size, follows the T10 target, absorbing particles generated in the interaction with the extreme borders. A triplet of quadrupole magnets (Q1-3) followed by an achromat (A1) focuses the beam particles and deflects the beam by 11 cm in the vertical direction (y-axis), selecting 75 GeV/c positively charged particles with about 1% precision. Inside the achromat, the beam passes through two beam dump units (TAX1-2) which absorb particles not satisfying the selection criteria. The TAXes can be adjusted in order to obtain different data taking conditions like muon runs or to perform searches for exotic particles [84].

A series of quadrupoles and collimators (Q4-10 and C1-C7) perform further selection and focussing of the beam. A series of tungsten foils, up to 5mm thick (1.3 X_0), placed between the TAX1 and TAX2, degrade positron energies to reject them in the second achromat (A2), while inducing minimal losses of hadrons due to scattering. The beam crosses steel plates inserted in the B3 dipole magnet through a 4 cm wide field-free bore. The magnetic field in the surrounding iron allows to sweep away off-axis muons of both signs. A horizontal steering magnet (TRIM5), placed at the end of the selection line, applies a 1.2 mrad deflection to the hadron beam on the positive x-axis in order to compensate the effect of the spectrometer magnet about 95m downstream and therefore keeping beam particles within the transportation tube until the dump at the end of the experiment.

2.4 KTAG: the kaon tagger

The KTAG is a differential Cherenkov counter designed to identify kaon mesons in the unseparated hadron beam and to measure their time with a resolution of about 70 ps. This requires the beam to be parallel to the z axis with an angular beam divergence below 100 μrad in each plane; the angular alignment of the detector to the beam axis must reach the same accuracy.

This detector consists of a 1.6 m long volume (0.94 m^3) filled with nitrogen at 1.75 bar (ambient temperature) as radiator coupled with an optical box to detect the Cherenkov light produced by beam particles at a defined angle. This represents, together with the KTAG windows, a total of 3.5%X_0 of material in the path of the beam.

An optical system selects and transmits the light to eight arrays of photomultipliers (referred as octants) placed on a circle (Figure 2.6). The coincidence between

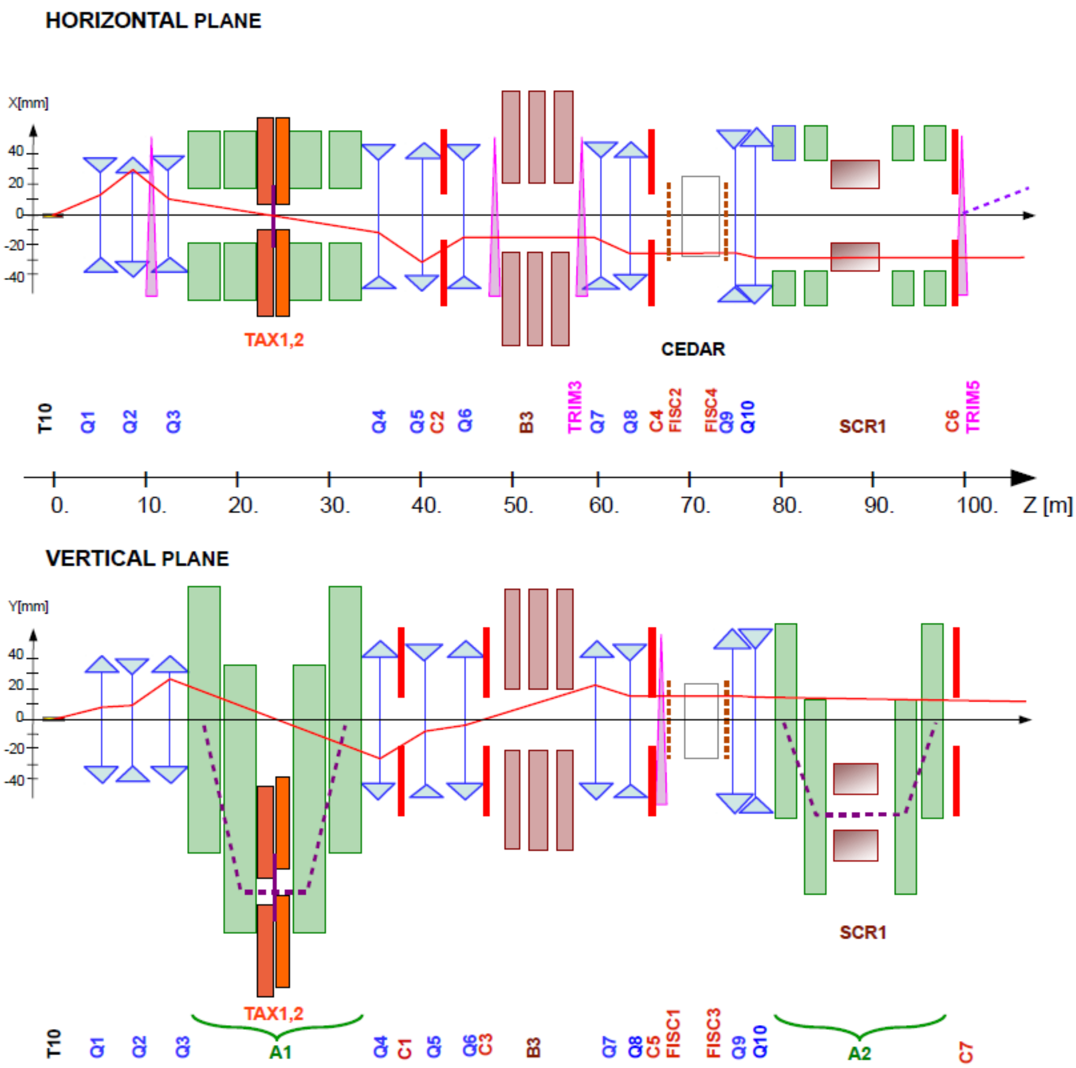

Figure 2.5: Schematic layout and optics of the high-intensity K^+ beam from the T10 target to the entrance of the decay region. In each view, the solid line corresponds to the trajectory of a particle leaving the target from the centre at nominal momentum and at the angle indicated. The dashed line indicates the trajectory of an initially on-axis 75 GeV/c momentum particle. Figure from [75].

signal in several octants (usually at least five) provides the kaon tagging.

The pressure in the KTAG is chosen so that only light from the desired particle type, i.e. kaons, at the known momentum, passes through an annular diaphragm of fixed central radius and varying radial aperture.

Special runs are acquired regularly along the data taking periods to perform

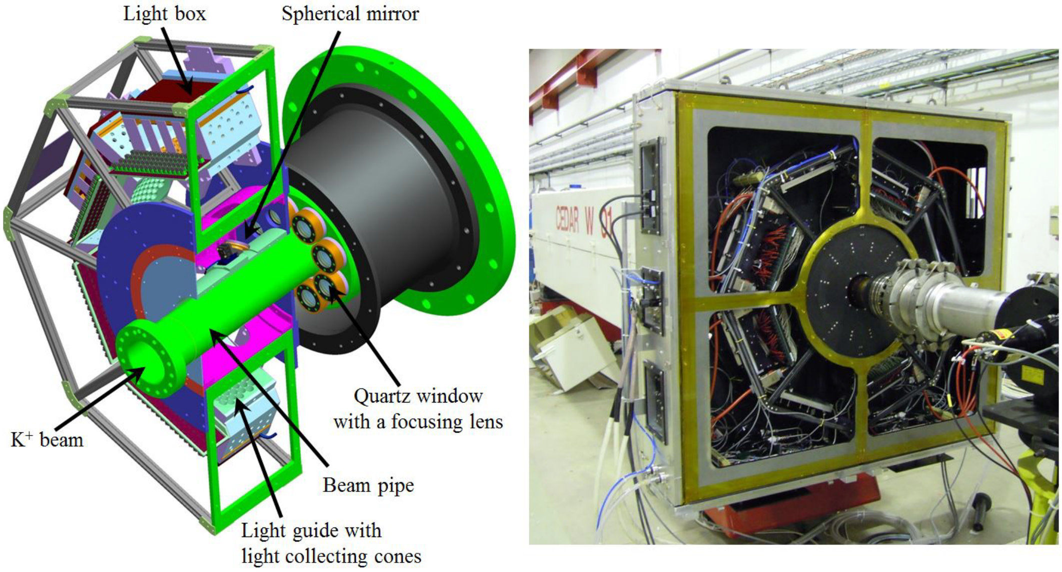

Figure 2.6: Left: drawing of the optical system and photomultipliers of the KTAG. Right: the KTAG detector in the NA62 beam line during a test run in 2012, with four of the eight sectors equipped. Figures from [75].

pressure scans in the detector, determining the effective beam particle composition (kaons, pions and protons as shown in Figure 2.7) and the best working pressure to select kaons at 75 GeV/c momentum, as well as to align the detector optics.

2.5 GTK: the beam tracker

The GigaTracker (GTK) has been designed to measure the momentum of the 75 GeV/c beam particles to 0.2% precision and their direction at the exit of the achromat to 16 μrad precision. This is a fundamental measurement for the reconstruction of the kinematics of the kaon decay (Equation 2.1). The high beam rate (750 MHz and up to 1.5 MHz/mm^2 around the detector centre) requires a hit time resolution better than 200 ps [85].

The GTK consists of three stations of silicon pixel detectors (GTK 1,2,3) installed around A2 achromat as shown in Figure 2.8.

A GTK station consists of a 200 μm thin silicon sensor containing 18000 pixels of 300×300 μm^2. The readout electronics are directly attached to the sensor via bumpbonding. They consist of an assembly of 10 ASICs with fixed threshold discriminator connected to a 97 ps time resolution TDC, measuring the times of threshold crossing in both the leading and the trailing edges to allow an offline time-walk correction. Each chip encodes and transmits the information recorded

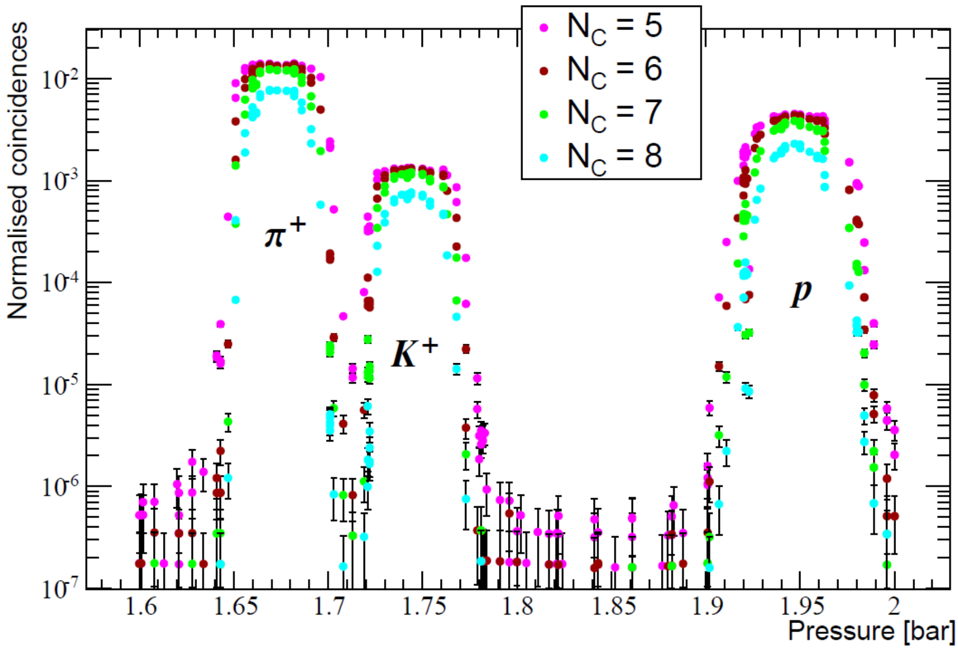

Figure 2.7: Results of a pressure scan with N_2 radiator gas at the nominal diaphragm aperture of 1.5 mm. For each minimum number of KTAG sectors required in coincidence N_C (ranging from 5 to 8), the normalised number of events satisfying the requirement is plotted versus the N_2 pressure. Well separated pion, kaon and proton peaks are visible. Figure from [75].

by the TDCs to a readout board out of the beam area via optical fibers. The whole detector is kept at a temperature of $-15°C$ through a micro-channels cooling plate glued on the readout in order to dissipate the heat generated by the readout electronics and to limit the radiation damage on the sensor. The complete assembly of a GTK station accounts for about 500 μm of silicon (200 μm from the sensor, 100 μm from the readout chips and 200 μm from the cooling plated) equivalent to less than 0.5% X_0.

2.6 CHANTI: a veto for beam interactions

Beam particles interact with a small, but not negligible, probability with the GTK material. Particularly dangerous for the $K^+ \to \pi^+\nu\bar{\nu}$ event selection is the inelastic scattering of beam pions and kaons on the last station of the beam tracker (GTK3), that can mimic a signal event: following the scattering, a pion enters the fiducial volume with momentum and direction compatible with a signal event, while other

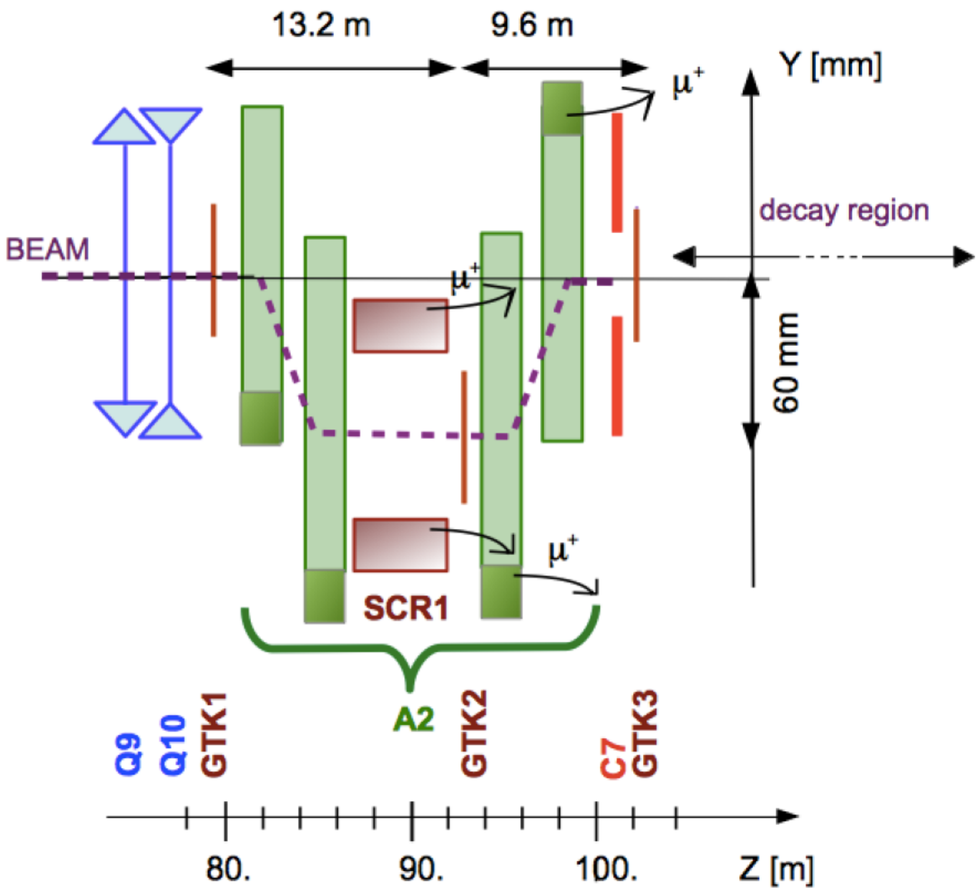

Figure 2.8: Schematic layout of the beam tracking and momentum measurement in the second achromat (A2). The beam is deflected vertically by 60 mm and returned to its nominal direction after the momentum measurement. Muons are swept away by the magnetized scraping collimator SCR1 and the return yokes of the last two magnets of the achromat (dark shaded areas). Figure from [75].

charged particles produced in the scattering are emitted at large angle escaping the apparatus undetected by the downstream detectors. Therefore, the Charged Anticounter detector (CHANTI) is devoted to the detection of particles produced with a range of angles between 28.5 mrad and 1.37 rad with respect to the beam pipe.

The CHANTI is composed of six consecutive squared hodoscope stations $300 \times 300\ mm^2$ in cross section with a $95 \times 65\ mm^2$ hole in the centre to leave room for the beam. The first station is placed 28 mm downstream of GTK3 and the distance between each station and the next one approximately doubles for successive stations, so that the angular region of interest is covered hermetically for particles generated on GTK3. All the CHANTI stations, together with GTK3 are located inside the same vacuum vessel.

The stations are made of scintillator bars with triangular base, the light is extracted by fast wavelength-shifting (WLS) fibres coupled to silicon photomultipliers (SiPMs). Each station has two planes, with the bars oriented vertically and horizontally to form X and Y views. Particles incident from the front of the detector generally traverse two bars. Each of the six stations consists of 48 bars, adding to a total of 288 bars.

By design, the CHANTI is required to have better than 2 ns time resolution in order to limit random losses due to overlapping events. This requirement has been fully satisfied: the detector has a single channel time resolution of 1.14 ns, a spatial resolution of ~ 2.5 mm and a single layer efficiency greater than 0.99 for penetrating charged particles [86].

2.7 Final collimator installed in June 2018

The main background of the $K^+ \to \pi^+ \nu \bar{\nu}$ selection arises from tracks generated before the beginning of the fiducial decay region (also called *upstream* background), entering this volume due to the lack of shielding at the position of the final collimator, corresponding to the aperture of the last dipole of the second achromat. Already in the final part of the 2017 data taking a copper plug was inserted into the dipole to mitigate this issue. In June 2018 the adjustable final collimator has been replaced with a fixed one which extends further transversally (Figure 2.9): this improves the shielding against *upstream* events.

This modification of the hardware configuration strongly affects the offline analysis, therefore the 2018 data have been split into two sub-samples: the data collected before and after the installation of the final collimator, corresponding to two different analyses criteria, as shown in the next chapters.

2.8 Fiducial decay region

The decay region is contained in the first ~ 80 m of a large 117 m long tank, starting 102.4 m downstream of the target, just after the GTK3. This tank is evacuated to a residual pressure of $\sim 10^{-6}$ mbar using up to seven cryo-pumps. The tank hosts 11 LAV detectors and the four spectrometer STRAW chambers, and consists of 19 cylindrical sections made of steel or stainless steel. The vessel diameter increases from 1.92 m in the first section after GTK3 to 2.4 m in the middle section and to 2.8 m in the spectrometer region. The vacuum tank is closed off at its downstream end by a thin aluminium window (2 mm thickness), separating the tank from the neon gas of the 17 m long RICH vessel. The flange around a hole in the centre of

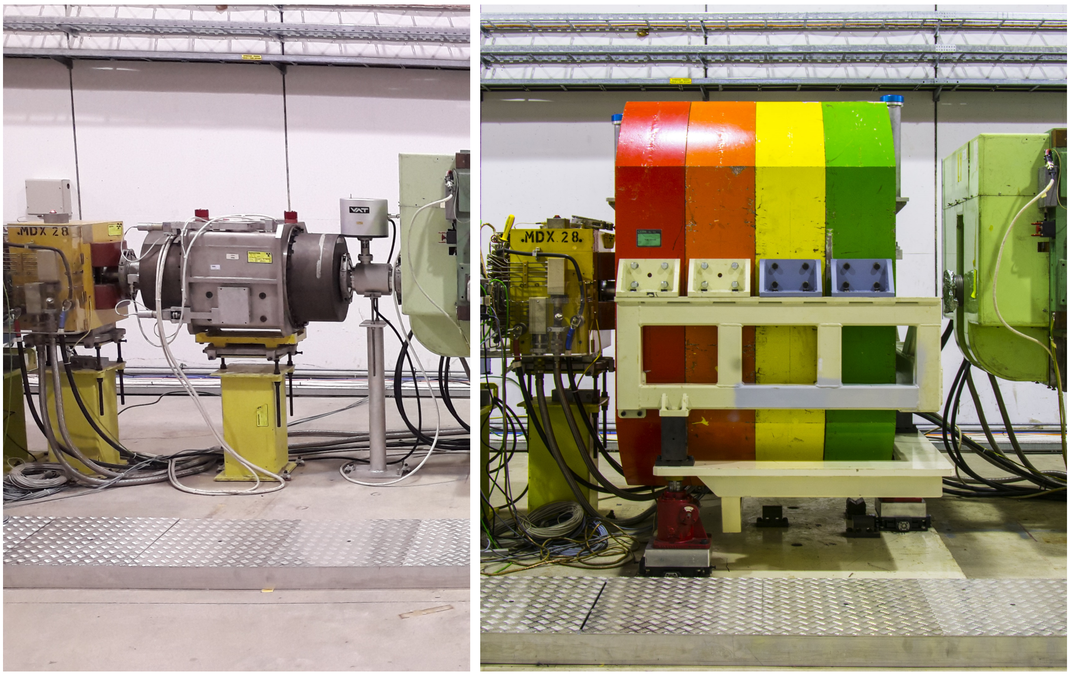

Figure 2.9: Pictures of the adjustable final collimator installed during the 2017 data taking (left) and the final fixed collimator installed in June 2018 (right). Figures from [36].

the window is attached to a thin-walled aluminium beam tube of inner diameter 168 mm, displaced to X = +34 mm and converging to the reference axis at an angle of -1.8 mrad to follow the trajectory of the beam, which is thus transported in vacuum throughout the length of the detectors, as shown in Figure 2.10.

2.9 STRAW: the spectrometer for downstream particles

Downstream of the fiducial decay region, a magnetic STRAW spectrometer is placed in vacuum to track the charged particles produced in the kaon decays. This is the second fundamental element for the kinematic reconstruction of the events (Equation 2.1).

The NA62 STRAW spectrometer is the first tracking system based on straw tubes operating in vacuum. The STRAW detector is composed of four chambers distributed, almost equidistantly, over a length of 35 m along the beam direction, with a dipole magnet (MNP33) between the second and the third station providing an integrated field of 0.9 Tm, that gives a horizontal momentum kick of 270 MeV/c,

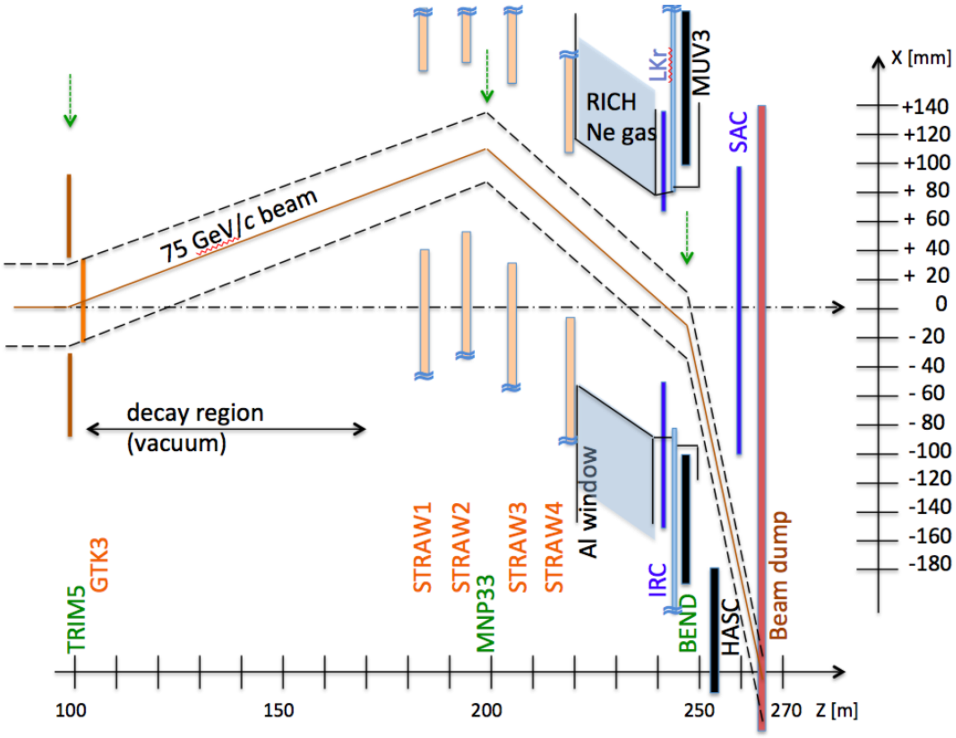

Figure 2.10: Close view of the beam line layout through the decay region and the detectors in the (X, Z) plane. At the entrance of the decay region the beam has a horizontal angle of +1.2 mrad, the beam is then deflected in the spectrometer magnet MNP33 by -3.6 mrad to match the central aperture of the LKr calorimeter. After MUV3, the dipole magnet BEND deflects charged particles associated with the beam away from the SAC and sends them into the beam dump. The dashed lines correspond to the two sigma width of the beam profile. The vertical arrows indicate the bending centre of each magnet. Figure from [75].

deflecting the 75 GeV/c beam by -3.6 mrad.

Each straw chamber contains 1792 straws of 9.82 mm diameter and 2160 mm length and is composed of two modules: one module contains two views measuring X (0°), Y (90°) and the other module contains the U (−45°) and V (+45°) views (Figure 2.11-L), in order to resolve ambiguities in presence of several crossing particles. High detection redundancy is provided through a straw arrangement with four layers per view, which guarantees at least two hits per view, i.e. 8-12 hits per track per chamber (Figure 2.11-R).

The center of each STRAW station is displaced with respect to the apparatus axis in order to accommodate the deflection of the beam induced by the TRIM5 and the MNP33 magnets.

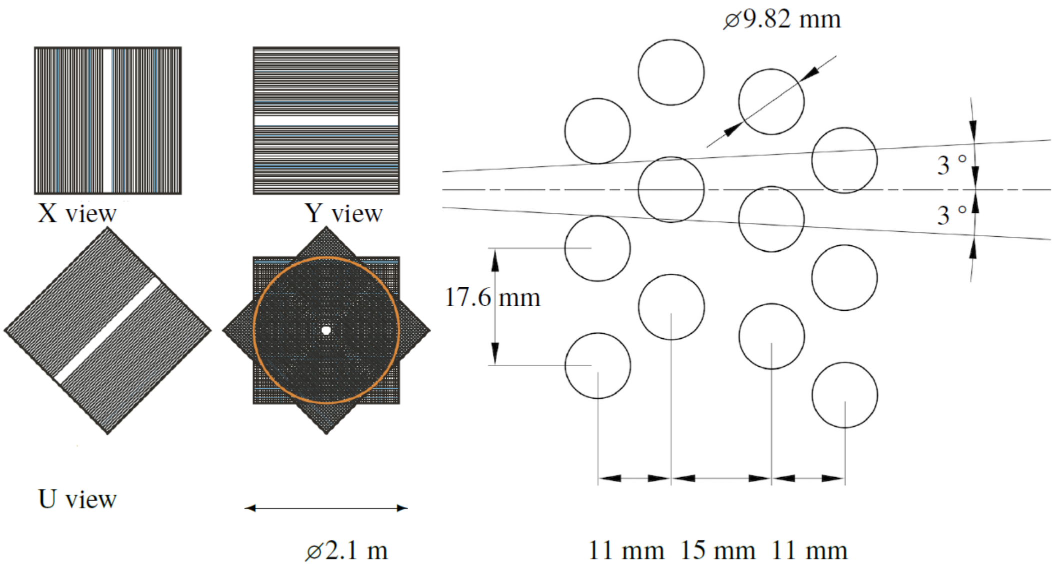

Figure 2.11: Left: one straw chamber is composed of four views (X, Y, U, V) and each view measures one coordinate. Near the middle of each view a few straws are left out forming a free passage for the beam. Right: the straw geometry is based on two double layers per view with sufficient overlap to guarantee at least two straw crossings per view and per track, as needed to solve the left-right ambiguity. The $\pm 3°$ angle corresponds to the angular range of tracks produced in kaon decays and detected within the geometrical acceptance of the spectrometer. Figures from [75].

The chambers active area is a circle of 2.1 m outer diameter centred on the longitudinal z axis, outside a 118 mm diameter material-free passage around the beam path.

The modules are designed to minimize multiple scattering and to give uniform space resolution over the full active area. The straw chambers are constructed of ultra-light material and are installed inside the vacuum tank. They operate with a mixture of gases (70% Ar and 30% CO_2) at atmospheric pressure. The total amount of material in the spectrometer corresponds to 1.8% X_0.

For tracks traversing all four chambers, the time resolution is found to be about 5 ns [75]. The track momentum resolution of the STRAW spectrometer is [75]:

$$\frac{\sigma(p)}{p} = 0.30\% \oplus 0.005\% \cdot p \tag{2.2}$$

and the angular resolution is about 60 μrad, that allows to reconstruct the kaon mass in $K^+ \rightarrow \pi^+\pi^+\pi^-$ events with a precision better than 1 MeV/c^2 [75].

2.10 RICH: the charged particle identification

The rejection of one of the main backgrounds for the $K^+ \to \pi^+\nu\bar{\nu}$ search, the $K^+ \to \mu^+\nu$ decay (Table 2.1), is achieved thanks to the separation between charged pions and muons, together with the kinematic reconstruction of the event. A fundamental role in the π/μ separation is played by the Ring Imaging Cherenkov detector (RICH).

The RICH vessel is a vacuum proof tank, 17 m long and made of structural steel, with the beam pipe (⊘ 168 mm) passing through it (as shown in Figure 2.12). It is divided in 4 cylindrical sections of decreasing diameter (4 ÷ 3 m) and different lengths.

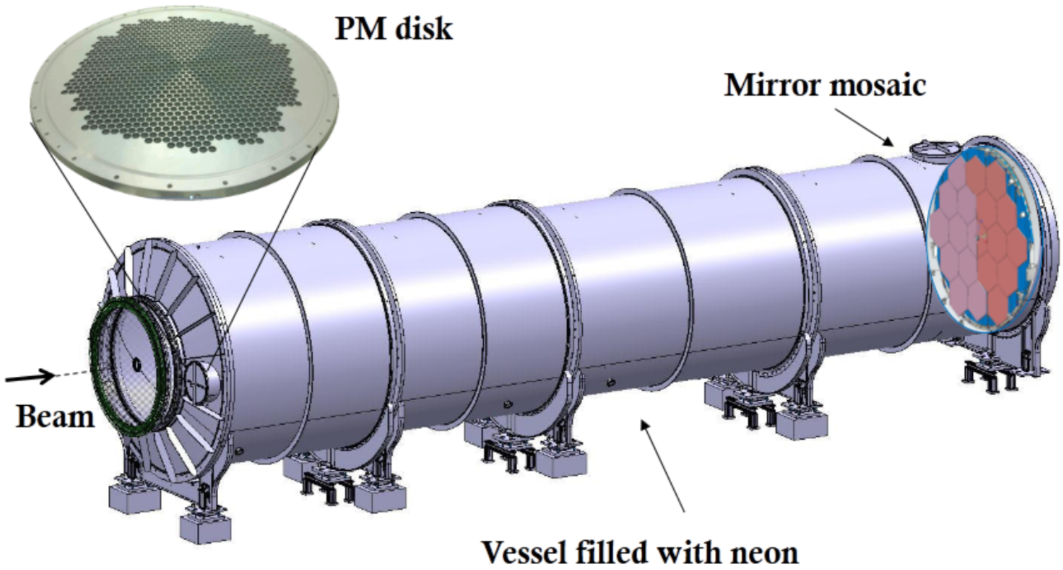

Figure 2.12: The RICH detector. The hadron beam enters from the left and travels through a beam pipe which crosses the detector. A zoom on one of the two disks accommodating the PMs is shown on the top left; the mirror mosaic inside the vessel is visible on the right. Figure from [87].

The vessel is filled with 200 m^3 of Neon (low atomic number to minimize X_0) at pressure slightly above 1 atm. The nominal refractive index is $n = 1 + 62.8 \times 10^{-6}$ at $\lambda = 300$ nm, with a corresponding Cherenkov threshold for charged pions of $p_{thres}(\pi^{\pm}) = m/\sqrt{n^2 - 1} \simeq 12.5\ GeV/c$.

At the end of the vessel there is a mosaic of 20 spherical mirrors with curvature radius of 34 m. 18 of them are hexagonal mirrors with a radius of 35 cm side, while 2 are semi-hexagonal mirrors with the hole for the beam pipe. The glass is 2.5 cm thick, with an aluminium coat and a MgF_2 protective layer. The average reflectivity is $\sim$ 90% for photons with λ in the range 195-650 nm. The support structure is an aluminium honeycomb panel: each mirror is supported by a back dowel, two aluminium ribbons keep the mirror in equilibrium and allow its orientation while a third ribbon prevents rotations. A system of piezo-motors, out of acceptance and remotely controlled, allows the alignment of each mirror, with a precision of $\simeq$ 1 mm ($\simeq$ 60 μrad) [88].

The Cherenkov photons are collected by two disks of 976 photomultipliers (PMs) each. The PMs have 16 mm wide face, 8 mm active region and are packed in hexagonal structure with 18 mm cell size. They are sensitive between $185 \div 690$ nm with a Quantum Efficiency of 20% at $\lambda_{peak} \sim 420$ nm. Winston cones are exploited in front of each PM surface to increase the geometrical coverage.

A more detailed description of the RICH detector can be found in [89], while a dedicated paper on the RICH light detection system has been recently published [87].

The RICH basic performance has been measured directly on physics data [87] [88]. The single hit time resolution is estimated to be $\sigma(T_{hit}) = 0.24$ ns, that leads to a global RICH time resolution of $\sigma(T_{RICH}) = 0.07$ ns in a positrons sample with an average number of hits in the RICH detector $\langle N_{hits} \rangle = 14.1$. The single hit space resolution is estimated to be $\sigma(S_{hit}) = 4.66$ mm, that leads to the following precision of the Cherenkov ring radius measurement in the same positrons sample: $\langle R_e \rangle = 189.6$ mm, $\sigma_{R_e} = 1.47$ mm.

The π/μ separation in the RICH is obtained exploiting the Cherenkov effect properties: the ring radius measured by the RICH (that is related to $\beta = v/c$ of the charged particle), combined with the momentum measured by the STRAW spectrometer, gives separated distributions for different particles, since the charged particle mass can be expressed as [90]:

$$m^2 = m^2(p, R) = p^2 \cdot \left(\frac{F^2 \cdot n^2}{F^2 + R^2} - 1 \right) \tag{2.3}$$

where n is the refractive index and $F = 17020$ mm the focal length.

The RICH ring radius versus track momentum for particles with different mass hypothesis is shown in Figure 2.13.

In the $K^+ \to \pi^+ \nu \bar{\nu}$ analysis of 2017 data [34], the following RICH efficiency for signal and background has been obtained in the momentum range 15-35 GeV/c [90] [91]:

$$\epsilon(\pi) \simeq 83\% \; at \; \epsilon(\mu) \simeq 0.2\% \tag{2.4}$$

Owing to the good timing performance the RICH detector is able to participate to the level-0 trigger chain providing the reference time [83], with an efficiency better than 99%.

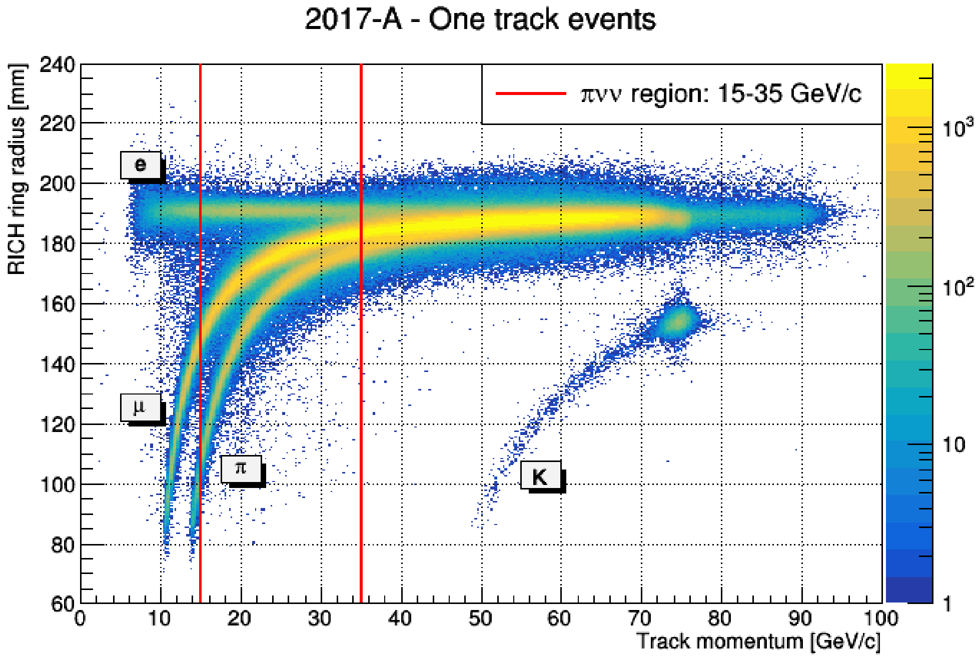

Figure 2.13: RICH reconstructed radius as a function of the track momentum, for one-track selected events in 2017 data. The different distributions of positrons, muons, pions and kaons are visible. The momentum region of RICH usage in the 2017 analysis (15-35 GeV/c) is delimited by red lines. Figure from [91].

2.11 CHOD and NewCHOD: the hodoscopes for charged particles

The NA62 setup includes a scintillator detector system called the charged particle hodoscopes: the CHOD and the NewCHOD, installed downstream of the RICH and upstream of the LKr calorimeter.

The Charged Hodoscope (CHOD), often referred as NA48-CHOD since it is inherited from the NA48 experiment [82], consists of two consecutive planes of 64 vertical and 64 horizontal plastic scintillator rods of 20 mm (0.10 X_0) thickness, as shown in Figure 2.14. Each rod is read out at one end by a photomultiplier through a plexiglass light guide. Both planes are assembled in 4 quadrants, each containing 16 counters. The scintillator lengths vary from 1210 mm (inner counters) to 600 mm (outer counters) forming an octagon of 1210 mm apothem. The widths are 65 mm in the central region close to the beam, where the particle flux is higher, and 99 mm in the outer region. The radius of the central hole crossed by the beam pipe is 128 mm.

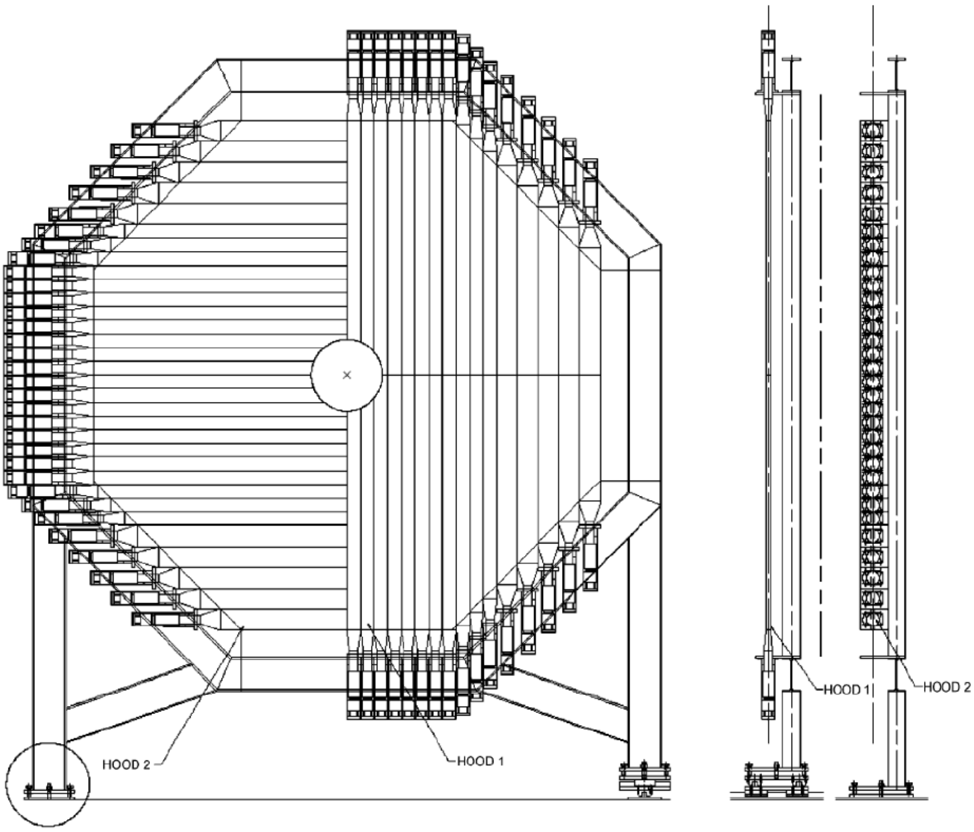

Figure 2.14: Drawing of the CHOD detector. Half sections of the horizontal and vertical planes are shown, with the beam traversing at the centre of the detector. Figure from [75].

The timing performance of the CHOD is remarkable with a resolution of about 200 ps [75], therefore it allows to improve the resolution on the track time provided by the STRAW. During data acquisition, the CHOD signals are independently employed in the generation of the minimum bias trigger.

Even if the CHOD provides excellent timing, the long strips are not able to cope with the high rate of the experiment. The crossing of several particles, close in time, leads to a large number of fake coincidences between horizontal and vertical plans, limiting the trigger selection capability. Then a new hodoscope, the NewCHOD has been built with a rectangular tile structure. The NewCHOD (Figure 2.15) consists of 152 plastic scintillator tiles of 30 mm thickness covering a circular crown surface with inner (outer) radius of 140 mm (1070 mm). The total thickness of the detector in the active area is 0.13 X_0.

The scintillation light is collected and transmitted by wavelength shifting fibers to a set of 304 SiPM pairs.

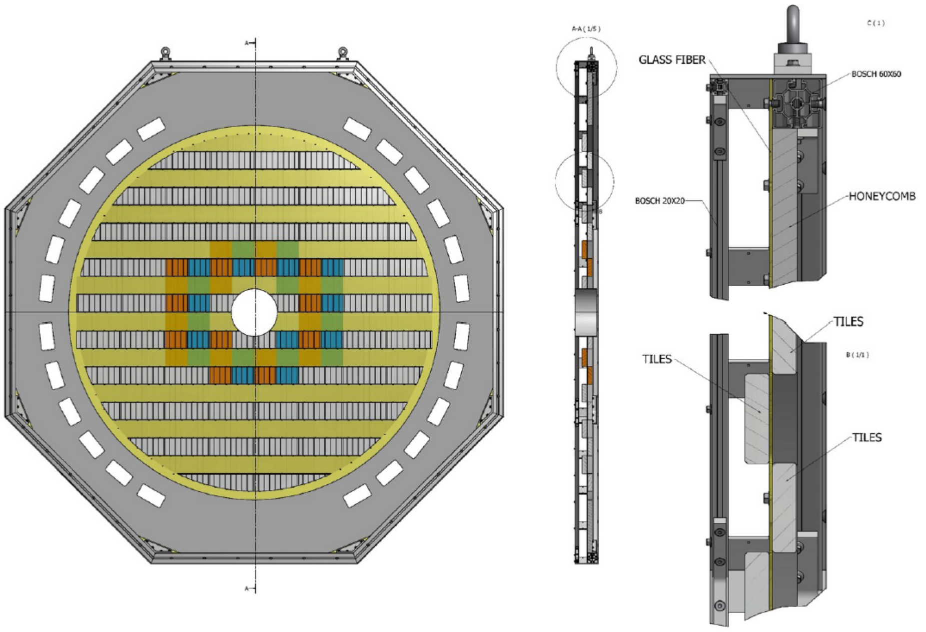

Figure 2.15: The NewCHOD detector is mounted on the front face of 12^{th} station of LAV (left). The 152 scintillator tiles of the NewCHOD detector are mounted front and back of thin G10 support panel (bottom right). The structure is stiffened at the periphery with honeycomb and aluminium construction profiles (top right). Figure from [75].

Starting from the 2017 data taking, the NewCHOD has been equipped with constant fraction discriminators (CFDs), with a significant improvement of the time resolution (below 500 ps). The detector geometry provides a simplified description of the event topology as the number and the distribution of the crossing charged particles.

2.12 LKr: the electromagnetic calorimeter

The last milestone for the background suppression, together with the event kinematic reconstruction and the charged particle identification, is the photon rejection. A key detector for both the charged particle identification and the photon rejection is a quasi-homogeneous electromagnetic calorimeter filled with 9000 liters of liquid krypton (LKr) at 120 K, that was built for the NA48 experiment and is described in details in [82].

The calorimeter extends from the beam pipe (r $\simeq$ 8 cm) to a radius of 128 cm; its depth is 127 cm, corresponding to 27 X_0.

The sensitive area is about 7 m^3, divided into 13248 longitudinal double ionization cells (2×2×127 cm^3) with a central anode as charge collector. Cathodes and anodes are made of thin Cu-Be ribbons almost aligned with the beam axis and with an accordion shape, in order to minimize the response dependence on the particle impact position (Figure 2.16). A 3 kV bias voltage is applied to the electrodes, making each cell working as an ionization chamber.

The signal generated by a particle crossing the detector is amplified and shaped by pre-amplifiers placed inside the cryostat. Immediately outside the detector, the pulse is converted into a differential signal and further shaped by transceiver boards, in order to be transferred, without distortions, to the readout. The signals are read out by boards with fast analog-to-digital converters (FADC) providing the magnitude and the time of the energy deposit.

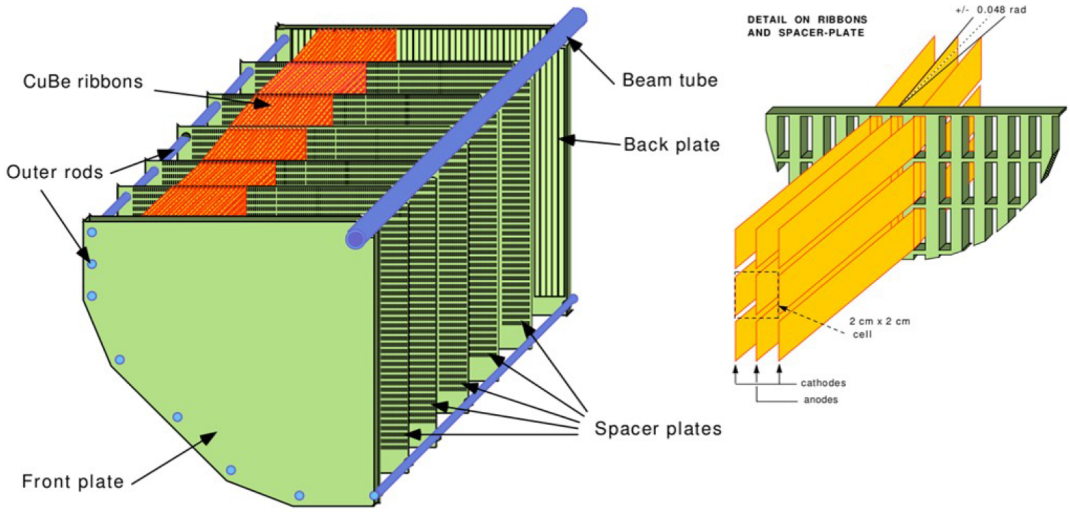

Figure 2.16: Left: schematic of the calorimeter structure (one quadrant). Right: detail of the calorimeter cells. Figure from [75].

Clusters are defined as the group of cells with deposited energy in a box around a peak in time and space. The cluster energy is then the sum of energies in each cluster cell and its position is the center of gravity of the cluster, computed as the weighted sum of the coordinates of each cell with the energy deposited in it.

The energy resolution can be parametrized as:

$$\frac{\sigma(E)}{E} = \frac{4.8\%}{\sqrt{E}} \oplus \frac{11\%}{E} \oplus 0.9\% \tag{2.5}$$

with E expressed in GeV. The first term contains the statistical fluctuation, the second is the noise term due to the electronics and the constant term for non-linearity and calibration effects.

The spatial resolution in both x and y coordinates can be written as:

$$\sigma_x = \sigma_y = \left(\frac{4.2}{\sqrt{E}} \oplus 0.6 \right) mm \tag{2.6}$$

where E is still expressed in GeV.

The typical time resolution is around 0.55 ns for electromagnetic clusters with a minimum energy of 3 GeV.

At the analysis level, calibrations for energy fine tuning of the LKr clusters are computed and applied with a routine developed and maintained by the author of this thesis. Details on the calibrations procedure are given in appendix A.

2.13 MUVs: vetoes for muons

The π/μ separation is achieved by the combined use of the RICH, LKr, hadron calorimeters (MUV1 and MUV2) and a muon detector (MUV3). The muon veto detectors are schematically shown in Figure 2.17.

The hadron calorimeters (MUV1 and MUV2) are sampling calorimeters made from alternating layers of iron and scintillator corresponding to about 8 nuclear interaction lengths.

The MUV1 consists of 24 iron plates of 2.7 cm thickness interleaved with 23 layers of 0.9 cm thick scintillator strips. Each active layer is composed of 44 scintillators 6 cm wide and spanning the whole detector length. The innermost scintillators, 8 in the horizontal and 10 in the vertical plane, are divided in two parts, each spanning (up to) half of the detector length, in order to accommodate the higher rate and the hole for the beam tube. Two wavelength-shifting fibers (WLS), glued inside the strips, perform the light collection and transmission to photomultipliers on both sides of the scintillator. For shorter strips the light readout is performed only on the outer side, while on the inner end reflective foils are glued on the fibers. In order to minimize the light losses, each scintillator is wrapped in aluminised mylar foils. The detector in total has 176 channels.

The MUV2 detector is the refurbished front module of the NA48 hadron calorimeter [82]. Similarly to the MUV1 detector, it is built as a sandwich calorimeter and consists of 24 iron plates of 25 mm thickness, each followed by plastic scintillators. Each scintillator plane consists of 44 scintillating strips with each strip spanning half the calorimeter. The strips are 1300 mm long, 119 mm wide and 4.5 mm thick. The two central strips of each half-plane are shaped on one end to enclose the central hole for the beam pipe. The strips are alternately aligned in the horizontal and vertical directions in consecutive planes. As in the MUV1 detector, the strips with identical alignment are coupled to the same PM but in this case using plexiglass light guides read out by PMs. In total the MUV2 has 88 readout channels.

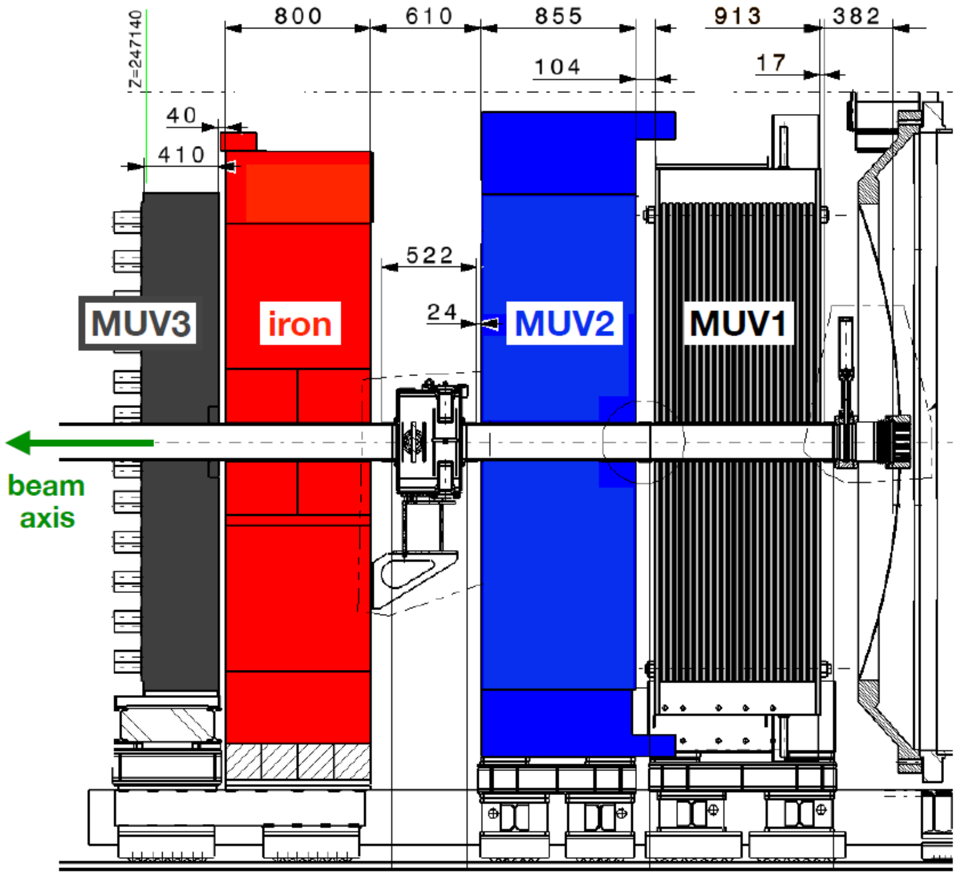

Figure 2.17: Schematic view of the NA62 muon veto system. Figure from [76].

The MUV3 detector, located downstream of the hadron calorimeter behind a 80 cm thick iron wall, provides fast L0 trigger signals and is used for muon identification. It detects charged particles traversing the whole calorimeter system (LKr, MUV1,2 and the iron wall) with a total thickness of over 14 interaction lengths. The MUV3 has a transverse size of 2640×2640 mm^2 and is built from 50 mm thick scintillator tiles, including 140 regular tiles of 220×220 mm^2 transverse dimensions and 8 smaller tiles adjacent to the beam pipe, to sustain the high particle rate near the beam. Each tile is read out by two PMs facing towards the tile. The signal from each PM is fed to a constant fraction discriminator (CFD) and then sent to the TEL62 readout board. A significant number of beam pions happen to decay into muons, which escape the beam pipe after the CHOD and illuminate the inner region of the MUV3: in order to minimize accidental losses due to such events, the fast muon veto has to provide a time resolution of about 500 ps.

2.14 LAV, IRC, SAC: a hermetic photon veto system

Even if the LKr already covers a significant part of the angular acceptance for the photon detection, it is not enough considering the level of precision needed in the NA62 experiment to keep the background coming from $K^+ \to \pi^+\pi^0$ process under control: the full angular acceptance is required to be hermetically covered.

The photons emitted at larger angle with respect to the LKr acceptance are detected by 12 stations of annular electromagnetic calorimeters, the *large angle vetoes* (LAV), while at smaller angles an intermediate ring calorimeter (IRC) and a small angle calorimeter (SAC) provide full coverage, as shown in Figure 2.18.

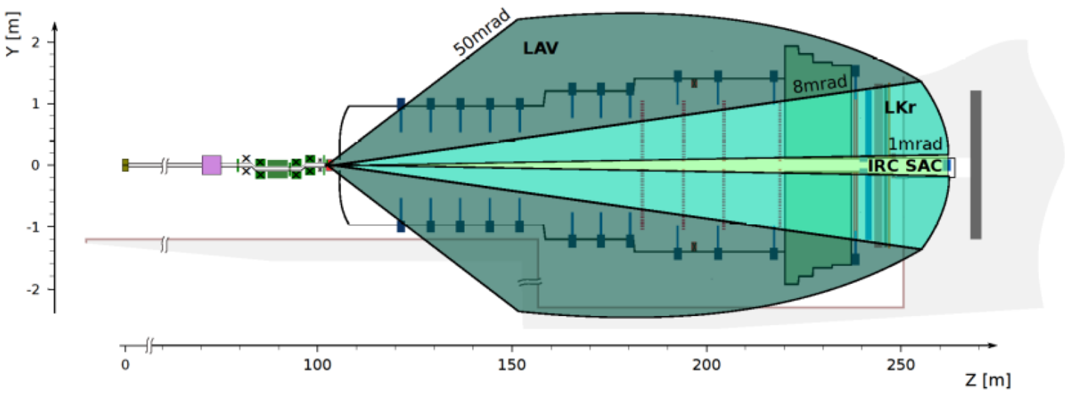

Figure 2.18: Schematic view of the angular coverage of the NA62 photon veto system (LAV, LKr, IRC, SAC). Figure from [36].

The LAV stations have been built of lead glass blocks, refurbished from the electromagnetic calorimeter of the OPAL experiment [92]. Each station contains from 4 to 5 layers of lead glass blocks (75% PbO), slightly misaligned to avoid inefficiencies due to photons travelling in the gap between two blocks. Electromagnetic showers in the lead glass are detected via the emitted Cherenkov light. The front and rear faces of the blocks measure about 10×10 cm^2 and 11×11 cm^2 , respectively. The blocks are 37 cm in length and each block is read out at the back side by a 76 mm diameter photomultiplier (PM), which is optically coupled via a 4 cm long cylindrical light guide. A LAV station is made by arranging these modules around the perimeter of the sensitive volume of the experiment, with the blocks aligned radially to form an inward-facing ring (Figure 2.19). Multiple rings are used in each station in order to provide the depth required for the efficient detection of incident particles. The modules in successive rings are staggered in azimuth while the rings are spaced longitudinally by about 1 cm. Particles incident on any station are intercepted by blocks in at least three rings, for a total minimum effective depth of 21 X_0. Most of the incident particles are intercepted by four or more blocks (at least 27 X_0). The time resolution for 1 GeV photons is about 1 ns. A test beam of a LAV station prototype was performed in 2009, using a tagged electron beam. The prototype showed an inefficiency of about 10^{-4} for a beam energy of 200 MeV and about 10^{-5} for 500 MeV electrons.

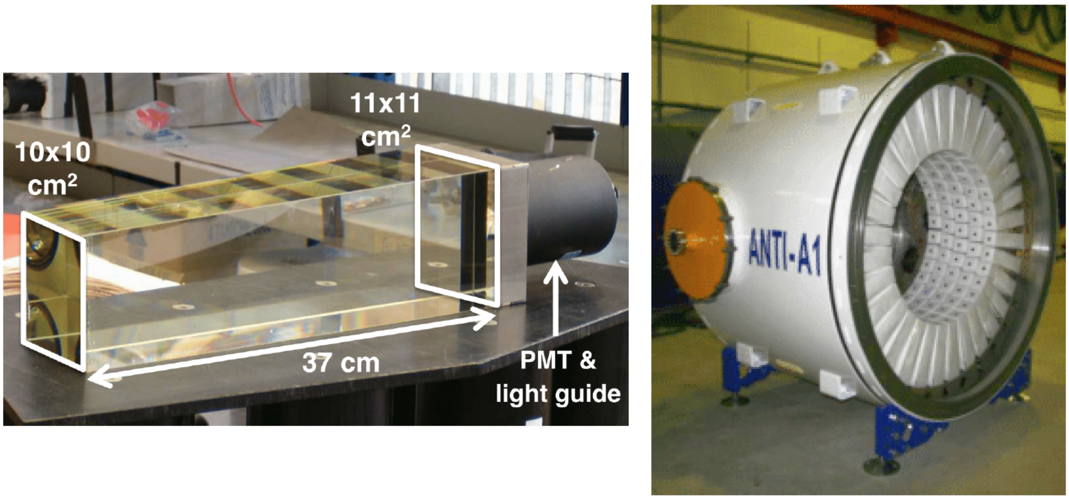

Figure 2.19: Left: A module from the OPAL calorimeter, without wrapping and with reinforcement plates at the interface between the glass and the steel flange. Right: Completed LAV1 station before insertion in the beam line. Figures from [75].

The energy sharing of the photons from a $\pi^0 \to \gamma\gamma$ decay can be, in rare cases, very unbalanced. In these events the very low energetic photon can escape the NA62 apparatus undetected, flying between two LAV stations, while the other may have such a large boost to remain within the beam tube. The small angle veto (SAV) system extends the photon detection coverage around and within the beam tube by employing two Shashlyk calorimeters, IRC and SAC.

The IRC is a lead/scintillator Shashlyk calorimeter in the shape of an eccentric cylinder surrounding the beam pipe upstream of the LKr. The detector has an outer diameter of 290 mm and is centered on the z axis. The central bore has a diameter of 120 mm with an offset of 12 mm towards positive x to account for the beam deflection by the spectrometer magnet (Figure 2.10). The IRC is divided into two longitudinal modules, with the upstream and downstream modules of 89 and 154 mm depth, respectively. The modules are spaced by 40 mm. To minimize the material in front of the sensitive volume, the IRC incorporates the corresponding segment of the beam vacuum tube as its inner support cylinder. The upstream and downstream modules contain 25 and 45 ring-shaped layers, respectively. Each layer consists of a 1.5 mm thick lead absorber and a 1.5 mm thick scintillator plate. The total depth for both modules is 19 X_0. The light is collected by optical fibers grouped in four bundles each coupled to a photomultiplier, read out using both TDC and FADC systems.

The SAC consists of 70 plates of lead interleaved with injection-molded plastic scintillator, both with transverse dimensions of 205×205 mm^2 and a thickness of 1.5 mm. The scintillation light is read out by 240 WLS fibres of 1 mm diameter. Each fibre is bent into a U shape and threaded through two holes, allowing readout of both ends at the back of the detector. As for the IRC, the light is collected by optical fibers grouped in four bundles each coupled to a photomultiplier. Given the scintillator plates have no transverse segmentation, the four readout channels are optically connected and the SAC is effectively a single-channel detector with a total depth of 19 X_0. The detector is installed inside the beam vacuum towards the end of the beam pipe after the dipole magnet, which deflects the remaining charged particles to the beam dump (Figure 2.10). To guarantee that photons incident on the SAC along the z axis do not traverse the detector along a WLS fibre for more than 10 cm (half of the active length) without encountering any of the lead converters, the SAC is aligned at a 23 mrad angle to the z axis in the horizontal plane. The four channels of the SAC are read out using both TDC and FADC electronics.

2.15 MUV0 and HASC: additional vetos for multitrack events

The MUV0 detector is a scintillator hodoscope designed to detect π^- emitted in $K^+ \to \pi^+\pi^+\pi^-$ decays with momenta below 10 GeV/c, deflected towards positive x by the spectrometer magnet (which adds to the deflection of the kaon beam induced by the TRIM5 magnet), and leaving the lateral acceptance near the RICH.

The hadronic sampling calorimeter (HASC) is used for the detection of π^+ emitted in $K^+ \to \pi^+\pi^+\pi^-$ decays with momentum above 50 GeV/c and propagating through the beam holes in the centre of the straw chambers. The detector is located downstream of MUV3 and the BEND dipole magnet (Figure 2.10) which sweeps these pions out of the kaon beam towards negative x.

2.16 NA62 trigger chain

The kaon decays in the fiducial volume happen with a rate of $O(10\text{ MHz})$ and several detectors are involved to produce trigger information: a multi-level trigger system is therefore needed in order to minimize the data collection dead-time and maximize efficiency and reliability.

The lower trigger level, denoted as Level 0 (L0), is implemented in hardware and works on data from faster sub-detectors at the full event rate, reducing it by a factor 10 [83] and driving the readout of data at 1 MHz to an online farm of commercial processors (PC farm), on which further High Level Trigger (HLT) selections are performed in software. The HLT includes a first level (L1) working on single sub-detector information, reducing the rate to 100 kHz and triggering the completion of the readout for the remaining data-heavy sub-detectors (the beam spectrometer and the calorimeters), and a second level (L2) working on the full detector information. The L2 trigger has not been used in the 2016-2018 data taking.

The information coming from the different sub-detectors is combined in different trigger masks, depending on the signature of the events of interest. The trigger mask dedicated to $K^+ \to \pi^+\nu\bar{\nu}$ events is the *Mask1*, called *PNN trigger*. The trigger conditions during the 2018 data taking are the same as for 2017, described in [34].

The L0 of the PNN trigger requires a signal in the RICH to tag a charged particle. The time of this signal, called trigger time, is used as a reference to search for a coincidence within 6.25 ns for the following conditions:

- signal in one to four NewCHOD tiles;
- no signals in opposite NewCHOD quadrants to suppress $K^+ \to \pi^+\pi^+\pi^-$ decays;
- no signals in MUV3 to reject $K^+ \to \mu^+\nu$ decays;
- less than 30 GeV energy deposited in LKr and no more than one cluster to reject $K^+ \to \pi^+\pi^0$ decays.

The L1 of the PNN trigger requires:

- a kaon identified in KTAG;
- signals within 10 ns of the trigger time in at most two blocks of each LAV station;
- at least one STRAW track corresponding to a particle with momentum below 50 GeV/c and forming a vertex with the nominal beam axis upstream of the first STRAW chamber.

A minimum-bias trigger, called *CTRL trigger*, is also implemented to be independent from all the other trigger masks and it is based on CHOD information downscaled by a factor of 400; the trigger time is given by the CHOD signal. Data collected by the minimum-bias trigger are used to determine the kaon flux and for other studies as the trigger efficiency measurement or the background estimation.

From now on, the samples collected by the PNN trigger are called *PNN data*, while the samples collected by the CTRL trigger are called *CTRL data*.

2.17 Monte Carlo simulations

All the relevant kaon decay modes are simulated in the NA62 apparatus via Monte Carlo (MC) methods, based on the *GEANT4* toolkit [93] to describe detector geometry and response. The kaon decays are generated in the kaon rest frame using the appropriate matrix elements and form factors. The simulation also includes a description of the collimators and dipole and quadrupole magnets in the beam line. Certain aspects of the simulation are tuned using input from data, namely signal formation and readout detector inefficiencies.

For the $K^+ \to \pi^+\nu\bar{\nu}$ analysis, accidental activity is added to the KTAG Cherenkov counter and to the GTK beam tracker assuming the average beam intensity during the data taking, and using a library of pileup beam particles built from data, while no accidental activity is simulated in the detectors downstream of the last station of the beam tracker. Simulated data are processed and analyzed using the same reconstruction and calibration procedures as for real data.

Chapter 3

The $K^+ \to \pi^+\nu\bar{\nu}$ and the normalization selections

The structure of the analysis of the 2018 data is inherited from the analysis of 2017 data, well described in [34]. However, several aspects have been optimized or improved, with the goal of increasing the signal acceptance while keeping the same (or better) signal over background (S/B) ratio.

In this chapter the full $K^+ \to \pi^+\nu\bar{\nu}$ selection criteria are described, with particular emphasis on the modifications and the improvements with respect to the 2017 data analysis, that represent an important fraction of this thesis work.

The selection of the normalization channel is described as well. In order to build a normalization selection as much as possible similar to the signal selection, the $K^+ \to \pi^+\pi^0$ channel has been chosen as normalization: the two selections share the charged particle identification criteria and the algorithm for the matching between the downstream (K^+) and the upstream (π^+) tracks, while only the kinematic requirement and the photon and multiplicity (i.e. extra activity with respect to the downstream pion track) rejection are different. This leads to the cancellation of several systematic effects in the normalization process. Moreover, the $K^+ \to \pi^+\pi^0$ branching ratio (Table 2.1) is 9 orders of magnitude larger than the signal and it is precisely measured, therefore the statistical and the external uncertainties introduced in the final measurement by the normalization are negligible.

3.1 Data sample

In the full 2016-2018 period of data taking, the NA62 experiment collected around $2.2 \cdot 10^{18}$ protons on target (POT), as shown in Figure 3.1, that correspond to around $6 \cdot 10^{12}$ kaon decays in the fiducial volume (estimate performed before quality requirements); the 2018 period accounts for nearly 2/3 of the total kaon decays (estimations provided in [81]).

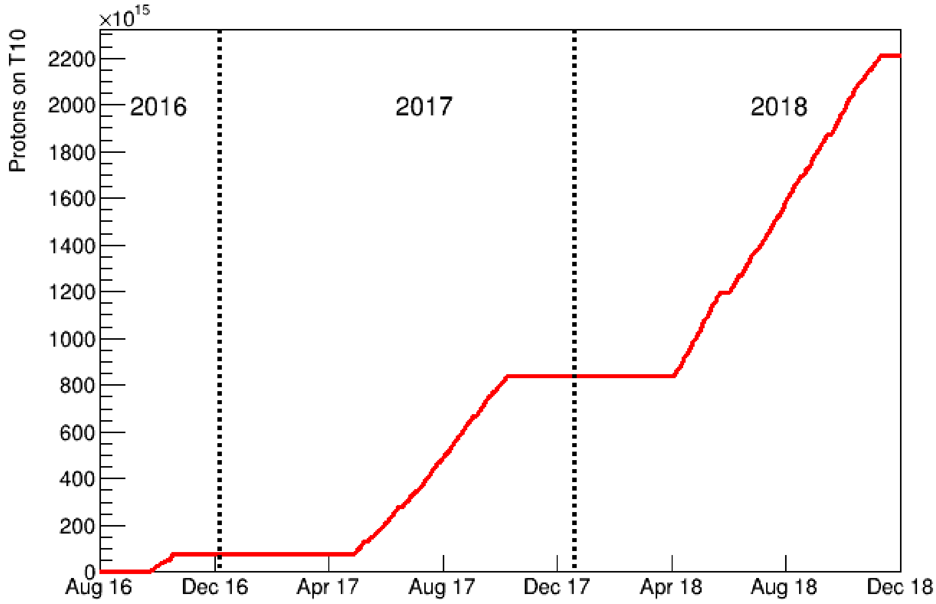

Figure 3.1: Protons on target (POT) collected by the NA62 experiment as a function of the data taking period. Figure from [36].

The 2018 data sample is split into 8 sub-samples: A,B,C,D,E,F,G,H. The period A is the one at the beginning of the data taking (April 2018), while H is the last period, just before the shutdown (November 2018). The beam intensity was kept stable at $60-70\%$ of the nominal (750 MHz), optimized for efficient data taking conditions. Only in the period H the intensity has been increased up to $\sim 80\%$ of the nominal. The effect of the intensity on the analysis has been studied and it is marginal (Table 4.4): therefore all the analysis criteria do not depend upon intensity.

The only relevant different data taking condition between the sub-samples has been the installation of the final fixed collimator (as outlined in the previous chapter) in between the C and D periods. This modification had a remarkable impact on the analysis optimization and, therefore, the overall data sample has been split into two sub-samples:

- 2018-OLDCOL corresponding to the same data taking condition of 2017, before the installation of the final collimator;

- 2018-NEWCOL, after the installation of the final collimator.

.

The 2018-NEWCOL sample represents nearly 70% of the full 2018 sample in terms of collected kaon decays.

3.2 Trigger conditions

The $K^+ \to \pi^+\nu\bar{\nu}$ selection starts at the trigger level, with the following requirements at hardware level, (same as for 2017 data) [34]:

- a signal compatible with the passage of a charged particle in the RICH detector and its time is taken as reference;
- a one-track signal in the NewCHOD (between 1 and 4 hit tiles) within ± 6.25 ns from the reference time;
- no signals in opposite NewCHOD quadrants (to suppress $K^+ \to \pi^+\pi^+\pi^-$ decays) and no signals in MUV3 (to reject $K^+ \to \mu^+\nu$ decays) in the same $\pm$ 6.25 ns time window;
- less than 30 GeV energy deposited in LKr and no more than one cluster, in order to reject $K^+ \to \pi^+\pi^0$ decays.

The level 1 (software) trigger adds a further condition for the photon rejection (signals within 10 ns with respect to the trigger time in at most two blocks of each LAV station), a constraint on the charged track (at least one STRAW track corresponding to a particle with momentum below 50 GeV/c and forming a vertex with the nominal beam axis before the first STRAW chamber) and asks for the presence of a signal in the KTAG compatible with a kaon hypothesis.

In fact, the PNN trigger selects events compatible with a one-track event topology, while vetoing the main K^+ decay channels, as $K^+ \to \mu^+\nu$, $K^+ \to \pi^+\pi^0$, $K^+ \to \pi^+\pi^+\pi^-$.

The normalization events ($K^+ \to \pi^+\pi^0$) are selected using the minimum bias trigger (signal of a charged track in the CHOD). The minimum bias trigger is strongly down-scaled by a factor of 400, given that it is potentially generated by any K^+ decay.

The trigger conditions are replicated in the offline analysis as much as possible, in order to maximize the trigger efficiency and to minimize the effects of the different trigger masks used for the signal and the normalization selections.

3.3 Data processing filter

At the processing step, data are filtered to reduce the output size of the stored data. A dedicated algorithm, using very loose requirements, is used to select $K^+ \to \pi^+\nu\bar{\nu}$

candidates without introducing any bias: the event filter requires the following conditions:

- the event must be triggered by the PNN mask
- no error in the reconstruction and in hardware status of the detectors must be present
- at least 1 and not more than 10 candidates in the STRAW spectrometer must be reconstructed
- at least one track signal in the CHOD must be present: a vertical and a horizontal slab of the same quadrant must be hit
- at least one track in the STRAW spectrometer that satisfies the following requirements:
  - it has hits in all the four chambers;
  - momentum between 8 and 50 GeV/c;
  - the projection of the track after the magnet is in the geometrical acceptance of CHOD, NewCHOD, LKr, MUV3;
  - a CHOD signal (horizontal-vertical pair matched) associated to the track;
  - a KTAG candidate (at least 4 out of 8 sectors hit) in ± 5 with respect to the CHOD time;
  - at least one hit in each GTK station within ± 2 ns, with respect to the CHOD time;
  - no hits in MUV3 within ± 4 ns, with respect to the CHOD time;
  - no LKr clusters not associated with the track (at least 180 mm away from the extrapolation of the track to the LKr plane) within ± 5 with respect to the CHOD time.

These selection criteria guarantee a minimal quality of the downstream track candidate for the charged pion and a soft coincidence (or anti-coincidence) between the most relevant detectors.

The filter conditions for the CTRL data are only a small part of those applied to the PNN trigger stream, since the Control sample is used not only to select the normalization channel, but also for the study of background coming from the main kaon decays. In particular only the conditions on the event reconstruction errors, on the track-CHOD and the track-GTK associations, and on the geometrical acceptance of the track in the main detectors are applied.

3.4 $K^+ \to \pi^+\nu\bar{\nu}$ selection: a global view

The $K^+ \to \pi^+\nu\bar{\nu}$ selection is build in several steps. All the following sections are aimed to describe them in detail, here only a short global illustration is given.

The first step is the selection of a downstream charged particle track, starting from the STRAW spectrometer candidate tracks and requiring associated signals (in time and space) in the relevant downstream detectors.

The parent kaon is then identified in the upstream detectors and associated with the downstream candidate track to form a candidate decay vertex. The vertex point is then defined as the median between the two tracks at their *closest distance of approach* (CDA). The vertex must be inside the decay fiducial volume, defined below.

Once the kaon and the pion tracks are identified, the kinematics of the decay is also reconstructed, with the computation of squared missing mass m^2_{miss} (Equation 2.1).

Kaon decays in distinct channels lead to different values of m^2_{miss} : this allows the definition of kinematic regions for signal, background and control, shown in Figure 3.2, for the 2017 data sample.

The analysis adopts a blinded procedure, therefore the signal and control regions are kept masked.

The downstream particle must then be identified as a π^+, exploiting the RICH, calorimeters and MUV3 information, in order to reject kaon decays with muons and positrons in the final state (e.g. $K^+ \to \mu^+\nu$). Final states containing photons or multiple charged tracks are also disregarded.

3.5 Downstream track selection: π^+

The π^+ track is selected looking for a coincidence in time and space between signals in the downstream detectors STRAW, CHOD, NewCHOD, RICH, LKr.

Starting from the STRAW, the track candidate should satisfy all the requirements applied at the filter level (in particular quality checks and projection in geometrical acceptance of the other downstream detectors) and be compatible with a positively charged particle. Moreover the track projection should be outside of the photon vetoes (LAV, IRC, SAC) acceptance. The track is then associated to a CHOD signal using a discriminant based on space and time coincidence (the weights of the two contributions are applied taking into account the experimental resolutions), while for the NewCHOD the candidate closest to the track projection impact point is associated to the track; the NewCHOD candidate is then required to be in time (± 5 ns) with the CHOD candidate. In the LKr, an energy deposit (cluster) is associated to the track if its position is within 100 mm from the track projection

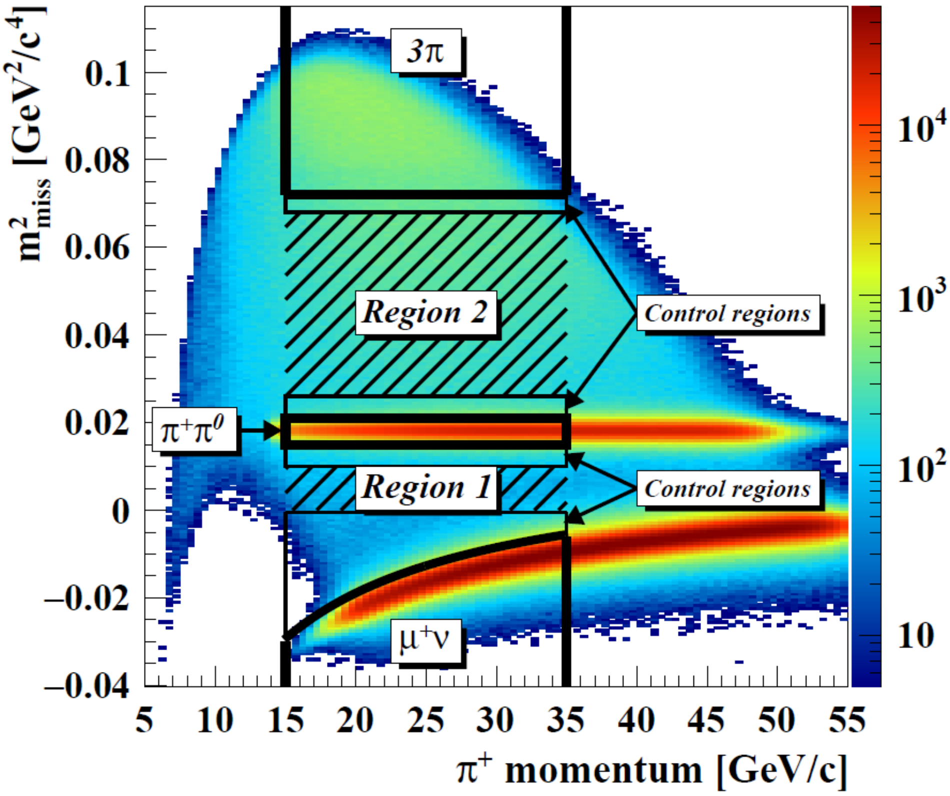

Figure 3.2: Reconstructed m^2_{miss} as a function of the π^+ momentum for Control sample events, assuming the K^+ and π^+ mass for the parent and decay particle, respectively. The signal regions 1 and 2 (hatched areas), as well as $K^+ \to \pi^+\pi^+\pi^-$, $K^+ \to \pi^+\pi^0$ and $K^+ \to \mu^+\nu$ background regions (solid thick contours) are shown. The control regions are located between the signal and background regions. The definition of the regions refers to the analysis of the 2017 data. Figure from [34].

impact point and the cluster time is inside ±2 ns of CHOD time. The LKr cluster time and position are given by the cell in the cluster with the highest energy deposit. The sum of the energies of the cluster cells is assumed to be the energy deposited by the particle in the LKr calorimeter.

The last detector to be associated to the track is the RICH. Using the slope of the track, the expected ring center at the RICH PMs plane is computed. Starting from this, two different approaches are used to build RICH ring candidates with the hit PMs. In the first approach all the hits compatible with a single track are grouped, the ring time is computed as the average of the hits time and then a likelihood discriminant is computed assuming different mass hypotheses (e^+, μ^+, π^+, K^+, *noise*), that is used for particle identification purpose, as illustrated in Section 3.10.2. In the second approach, all the hits included in an annulus centered in the expected ring center are taken into account and a χ^2 fit procedure is used to compute the ring center coordinates and radius; the possibility to discard the worst hit is foreseen if the first χ^2 is too high. The annulus is chosen large enough to cover the full area where hits from different kind of particle are expected, following a dedicated study performed in the analysis of 2017 data, related to the estimation of background with positrons in the final state. The best compromise for correct positron ring reconstruction and minimizing accidental hits is accomplished by using an annulus between 80 and 240 mm from the extrapolated center. In this second approach the ring time is computed as the average of the hits time used for the ring fit. The track is successfully associated to the RICH detector if both the reconstruction procedures find a ring in time within ±3 ns from the CHOD candidate time.

Finally, the track time is defined as the RICH time provided by the second approach.

If a STRAW track is not associated with all the detectors as illustrated, it is rejected. Moreover, its momentum must be in the range 15-45 GeV/c, in order to avoid STRAW reconstruction inefficiencies at low momenta and to require at least ∼30 GeV of missing energy due to the $\nu\bar{\nu}$ pair.

3.6 Parent K^+ selection and $K^+ - \pi^+$ matching

The parent beam particle is identified by the KTAG and the GTK detectors, upstream of the fiducial decay volume.

The downstream track is matched to the KTAG candidate closest in time and within ±2 ns, with at least 5 out of 8 sectors hit by Cherenkov photons. Then a GTK candidate (upstream track) is matched requiring a time coincidence with the KTAG and a spatial association with the STRAW track, using a discriminant built as follows.

The $K^+ - \pi^+$ matching algorithm is one of the crucial part of the analysis. This is performed with a discriminant based on the time difference between the GTK and KTAG detectors, $\Delta t(KTAG - GTK)$, and the minimum distance between the STRAW and the GTK tracks, the *closest distance of approach (CDA)*. The weights of the two terms are related to the experimental resolution of the two variables. For a given downstream track, the GTK track with the best discriminant is matched. The two variables $\Delta t(KTAG - GTK)$ and CDA are studied directly with real data using a clean sample of $K^+ \to \pi^+\pi^+\pi^-$ events. The reconstruction of the three pions tracks in the STRAW is sufficient to tag the parent kaon track in the GTK; this track is then associated to one of the two positive charged pions in the final state and $\Delta t(KTAG - GTK)$ and CDA for those two tracks are measured. For comparison, the two quantities are measured also matching one of the π^+ with a random GTK track. This allows to study also the two type of errors that could occur in the $K^+ - \pi^+$ matching procedure: a *wrong association* or an *accidental association*. In fact the beam particle rate in the GTK detector is very high (nominal rate: 750 MHz) therefore the probability to find a *pile-up* track within less than 1 ns from the real parent particle track is not negligible: a *wrong association* happens when a GTK pile-up track gives a matching discriminant better than the real parent kaon track, while an *accidental association* occurs when a GTK pile-up track is matched with the downstream particle because the real parent kaon track is not reconstructed in the GTK. Therefore a minimum quality selection on the discriminant is applied to avoid the *accidental association*, while *wrong associations* are strongly reduced by vetoing the presence of two or more tracks with very good discriminant values. An additional discriminant, with respect to the RICH time instead of the GTK time, has been analogously defined and used in the analysis to reinforce the $K^+ - \pi^+$ association.

The distributions of $\Delta t(KTAG - GTK)$ and CDA in the $K^+ \to \pi^+\pi^+\pi^-$ sample are shown in Figure 3.3. According to those distributions, the following additional conditions are applied in order to further suppress accidental matching:

- $CDA < 4$ mm
- $|\Delta t(KTAG - GTK)| < 0.5$ ns
- $|\Delta t(KTAG - RICH)| < 0.5$ ns
- $|\Delta t(RICH - GTK)| < 0.5$ ns
- $|\Delta t(CHOD - GTK)| < 1.1$ ns

The last timing requirement is more relaxed with respect to the others, because of the worse time resolution of the CHOD.

Once the $K^+ - \pi^+$ matching has been accomplished, the coordinates of the decay vertex are reconstructed as the mean point in between the two tracks at their closest distance of approach.

Events with activity in the CHANTI within 3 ns are rejected, since this would signal nuclear interactions of the beam particles before the the fiducial decay region, that could affect the K^+ reconstruction and the $K^+ - \pi^+$ matching.

3.7 Upstream background rejection

The main background source for the $K^+ \to \pi^+\nu\bar{\nu}$ decays is not associated with particle decays in the fiducial volume, but rather with activity in the upstream beam section. Before discussing the rejection criteria we will go through a general illustration of these events, called *upstream* events.

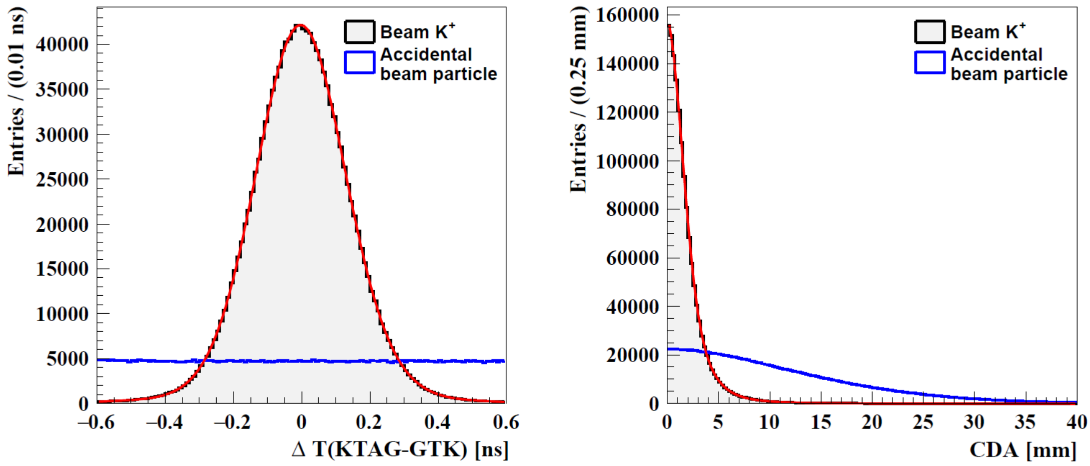

Figure 3.3: Distributions of $\Delta t(KTAG-GTK)$ (left) and CDA (right) for events with parent K^+ (shaded histogram) and accidental beam particle (blue histogram), as obtained from fully reconstructed $K^+ \to \pi^+\pi^+\pi^-$ decays in the data. The red curves superimposed on the histograms describe the functions used to model the time and CDA distributions of the parent K^+. Figure from [34].

3.7.1 *Upstream* events

An *upstream* event is originated by early kaon decays or beam particle interactions before the fiducial region, in these case the event can be a background source for the $K^+ \to \pi^+\nu\bar{\nu}$ search if all the following conditions happen: a π^+ enters in the fiducial decay region and is detected in the downstream detectors, all the other products in the process are missed, the charged pion matches with a K^+ candidate reconstructed in KTAG and GTK detectors.

A schematic view of the most common process for the upstream background events is represented in Figure 3.4, where:

- the π^+ originates from a K^+ decaying in the region upstream of GTK3;
- additional particles produced in the decay are absorbed by material in the beam line (e.g. photons from $\pi^0 \to \gamma\gamma$ in early $K^+ \to \pi^+\pi^0$ decay);
- the KTAG signal produced by the parent K^+ is matched by a pileup beam π^+ (or proton) track, reconstructed in the GTK;
- the π^+ is scattered in the first chamber of the spectrometer by a large angle, therefore the back-extrapolation of the track does not match the beam pipe hole at the entrance of the fiducial volume and produces a fake decay vertex inside the fiducial volume.

Other possible (and less significant) processes that could produce upstream background are illustrated in details in [34].

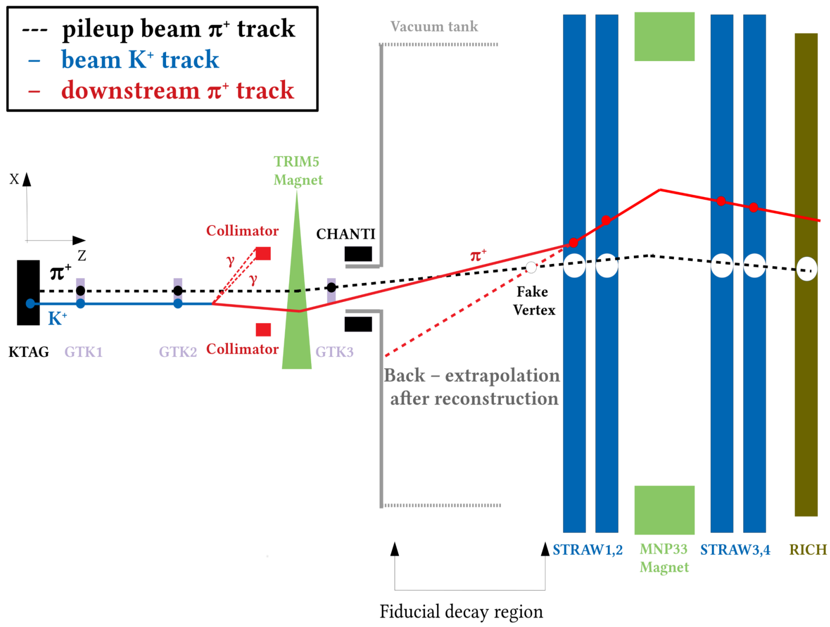

Figure 3.4: Schematic view of the most common process for the upstream background events. The illustrative sketch is not to scale. See the text for the description. Figure from [36].

3.7.2 Cut-based rejection of upstream background

An important suppression of the upstream background is therefore given by the conditions applied in the $K^+ - \pi^+$ association, described in the previous section. In addition, other geometrical variables, different from the variables already used in the matching, are employed to further suppress background. The physical quantities that have been considered are: the position of the track extrapolation at the final collimator $(X, Y)_{Coll}$ and at the first chamber of the STRAW $(X, Y)_{Straw1}$, the position of the reconstructed decay vertex $(X, Y, Z)_{vtx}$, the slope of the track with respect to z axis θ_X, θ_Y and $R_{Straw1} = \sqrt{(X_{Straw1})^2 + (Y_{Straw1})^2}$.

The analysis of the 2017 data excluded events in a box region in the $(X, Y)_{Coll}$ plane (Figure 3.5 Left) and in a trapezoidal shape in the (Z_{vtx}, R_{Straw1}) plane. An additional cut on Z_{vtx} was applied defining the fiducial volume as: $Z_{vtx} \in [105, 165]$ m.

The signal acceptance improvement achieved in the 2018 data analysis is mainly obtained changing the usage of these geometrical variables, exploiting the installation of the final collimator in the 2018-NEWCOL sample. The effect of the final collimator in the $(X, Y)_{Coll}$ distribution for upstream events is clearly shown in Figure 3.5, where it is evident how the events accumulated along the vertical band near the beam-pipe hole are rejected by the larger coverage on the Y direction given by the new collimator.

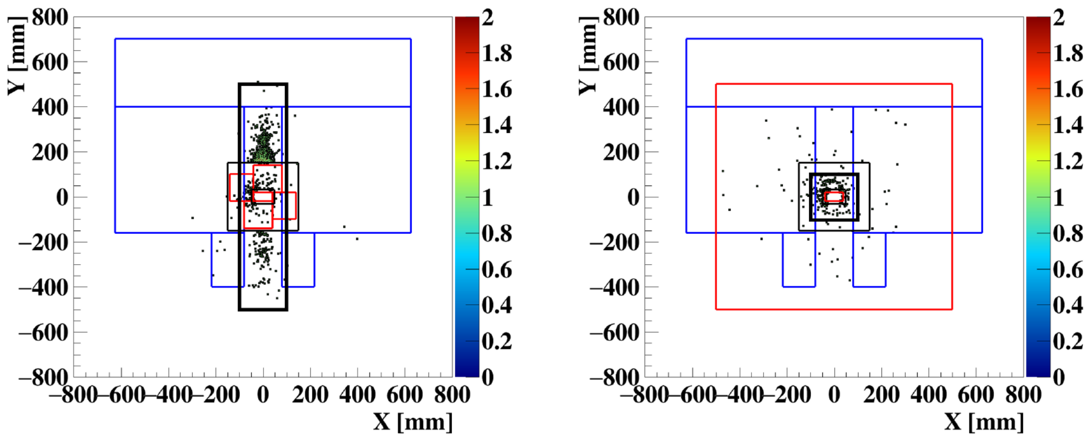

Figure 3.5: Position of the reconstructed π^+ projected at the final collimator for events passing a signal-like selection enriched in upstream events. The data shown are from the 2017 sample (Left) and the 2018-NEWCOL (Right). The central black thick box displays the geometrical cut that rejects the events inside. The blue contour is the transverse profile of the last dipole of the achromat. The red contours correspond to the shape of the final collimators employed in 2017 (Left) and 2018 (Right). The lighter black box shows the acceptance of the CHANTI detector that is effective against upstream events. Figure from [80].

These events are schematically represented in Figure 3.6, where the two sketches show how the charged pion generated in an early kaon decay can penetrate the fiducial decay region in the OLDCOL configuration, while it is stopped by the collimator in the NEWCOL configuration.

In order to better exploit the correlations between the geometrical variables listed before and the improvement given by the new collimator, a multi-variate approach has been introduced. This is not possible in the 2018-OLDCOL sample, therefore in this sample we used the same selection as for the 2017 data, with a modified region in the (Z_{vtx}, R_{Straw1}) plane as described later.

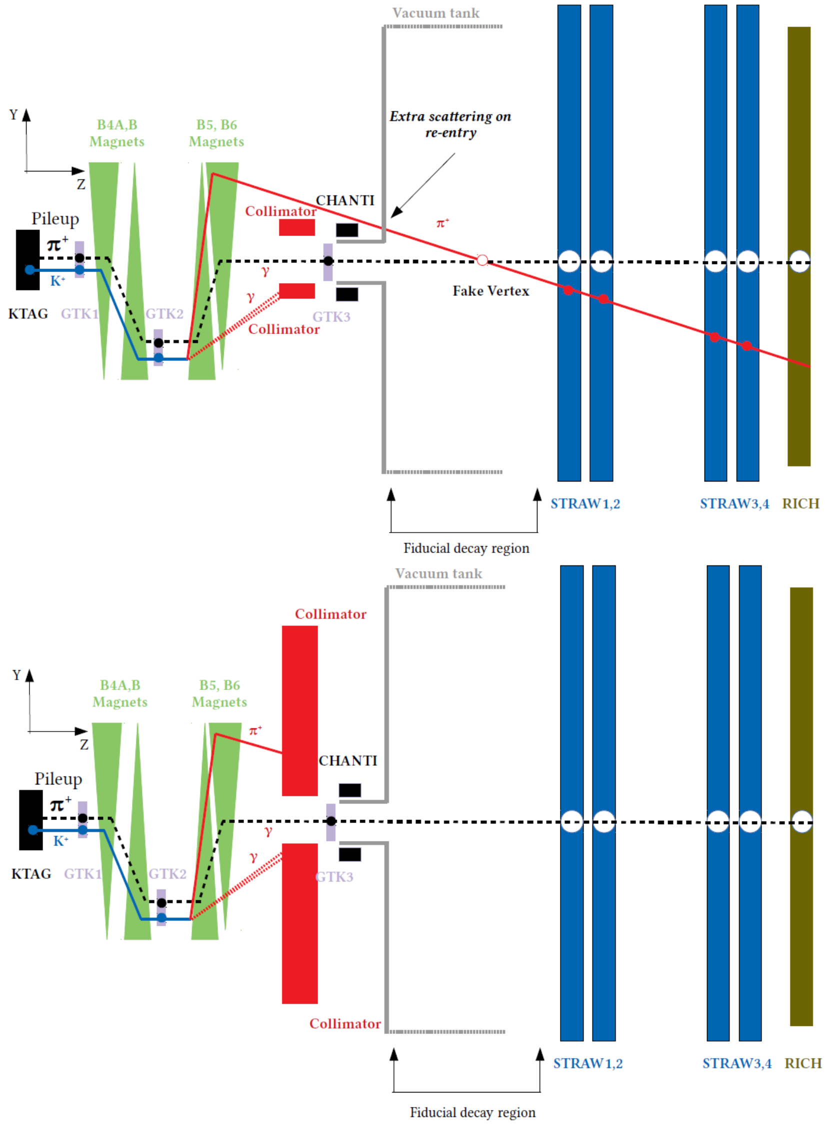

Figure 3.6: An example of an upstream event in which the produced charged pion enters the fiducial decay region in the OLDCOL configuration (Top) and is stopped in the NEWCOL configuration (Bottom). Sketches not to scale. Figure from [36].

3.7.3 BDT algorithm against upstream background

The multi-variate approach against the upstream background, applied only in the 2018-NEWCOL sample, consists in a *Boosted Decision Trees (BDT)* algorithm, that builds a *BDT classifier*, based on the ten geometrical variables listed in Section 3.7.2. A selection on the classifier is performed subsequently.

The fiducial volume is enlarged to $Z_{vtx} \in [105, 170]$ m and the ten variables are then passed to the BTD algorithm for the training: two samples are needed, for signal and background training, together with the corresponding physics samples, that must be disjoint from the training samples.

The signal training sample is selected applying the full $K^+ \to \pi^+\nu\bar{\nu}$ selection to a fraction of the $K^+ \to \pi^+\nu\bar{\nu}$ full Monte Carlo simulations, which afterwards is not used for the computation of the signal acceptance. The complementary fraction of the $K^+ \to \pi^+\nu\bar{\nu}$ Monte Carlo simulations is used for the signal physics sample.

The background training sample is selected on real data as follows. The upstream background is studied on a data sample unlinked to the signal selection, by requiring $CDA > 4$ mm, i.e. inverting the condition on CDA applied in the signal selection. In such a way the sample is enriched of upstream events and can be fully studied without violating the principles of blindness of the analysis, as illustrated in Section 5.5: it is taken as the background physics sample. In order to select an orthogonal sample that can be used as training without changing the features of the variables of interest, the timing coincidences of the $K^+ \to \pi^+\nu\bar{\nu}$ selection are inverted, as shown in Figure 3.7: events satisfying the full $K^+ \to \pi^+\nu\bar{\nu}$ selection with inverted CDA condition are plotted, those inside the red box (i.e. *in time*) represent the background physics sample, while events outside the red box (i.e. *out of time*) represent the background training sample.

Once the training samples are defined, they are passed to the BDT algorithm for the training. This is performed using the *Adaptive Boost* technique and optimizing the parameters of the BDT (number of decision trees; boosting power; maximum number of steps in each decision tree; minimum fraction of the initial statistics needed in a node in order to continue the growing of the tree; number of points in each variable range tested as possible cut), looking for the combination that gives the highest possible signal acceptance, keeping the background contamination at the same level obtained with the cut-based selection and avoiding over-training. The test samples (fraction of the training samples not used for the training) are used to check the performance in order to avoid over-training and to choose the value of the cut to be applied on the BDT discriminant (Figure 3.8).

An additional cross-check for the over-training is performed applying softer cuts on the BDT discriminant with respect to the chosen value, and comparing their performance in the test sample and in the physics sample.

The distributions of the main variables used in the BDT algorithm, in the $K^+ \to \pi^+\nu\bar{\nu}$ MC simulation, after the application of the full $K^+ \to \pi^+\nu\bar{\nu}$ selection, including the cut on the BDT discriminant, are shown in Figure 3.9 and in Figure 3.10.

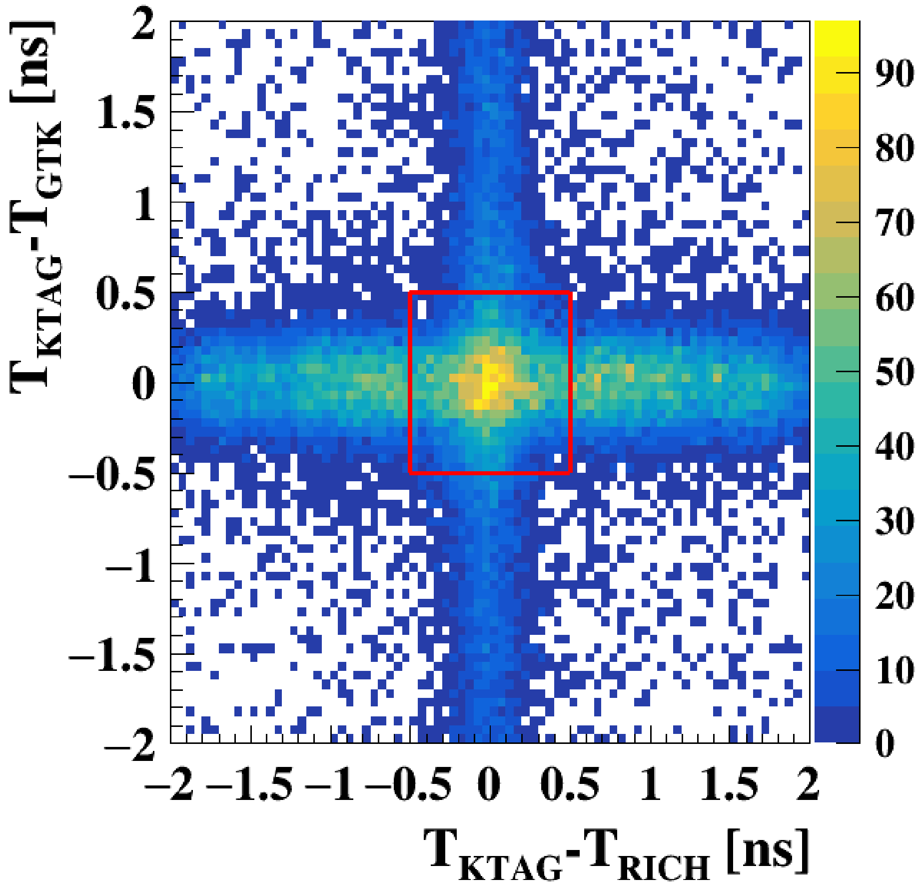

Figure 3.7: Timing distribution of events that pass the full $K^+ \to \pi^+\nu\bar{\nu}$ selection with inverted CDA condition. The red box represents the cuts of the time coincidence applied in the $K^+ \to \pi^+\nu\bar{\nu}$ selection.

3.8 ***Trapezoidal*** cut in the (Z_{vtx}, R_{Straw1}) plane

As already mentioned, in the 2017 analysis there was an additional requirement applied on the (Z_{vtx}, R_{Straw1}) plane: since both variables are used in the BDT algorithm against the upstream background, this condition has been removed for the training of the BDT.

This selection is not only effective against the upstream background but also against the background coming from the $K^+ \to \pi^+\pi^+\pi^-$ decays, that is not taken into account in the BDT training.

Since, as described in Chapter 5, the $K^+ \to \pi^+\pi^+\pi^-$ decays represent one of

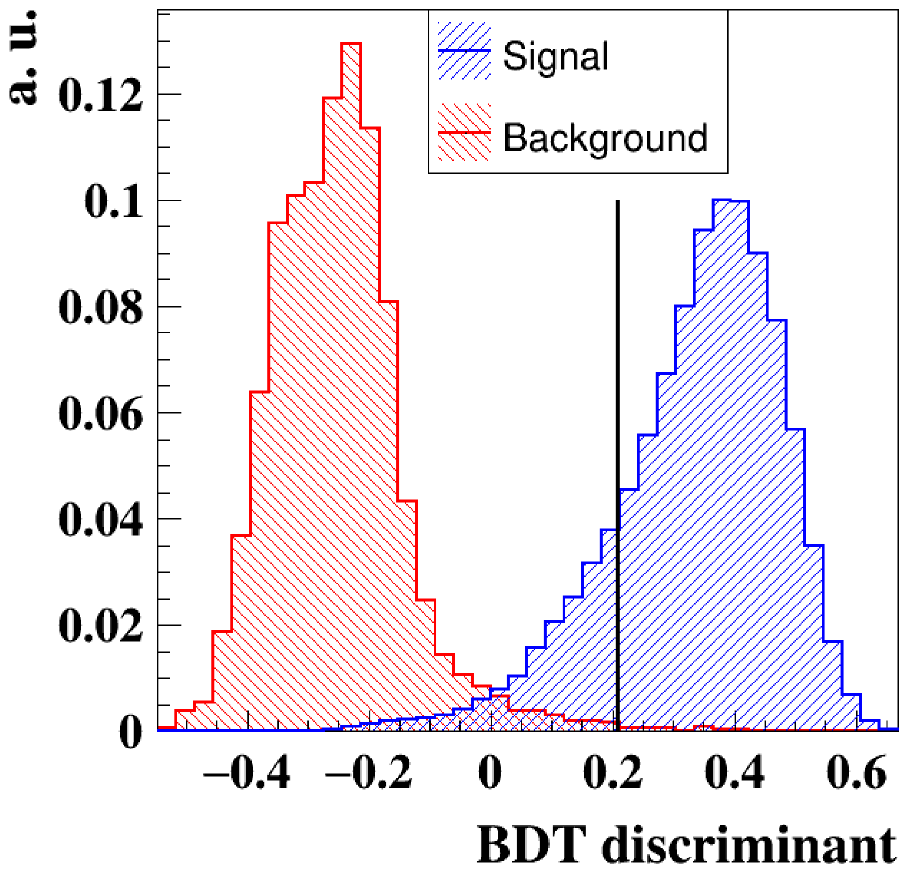

Figure 3.8: BDT discriminant for events in the test samples of the BDT training. Both distributions are normalized to 1. The black line represents the value chosen as cut for upstream events rejection. Figure from [36].

the minor background components, the new trapezoidal cut has been relaxed to obtain a negligible loss of signal acceptance, as shown in Figure 3.11, that is already enough to reject $\sim 30\%$ of $K^+ \to \pi^+\pi^+\pi^-$ events.

While the fiducial volume is defined as $Z_{vtx} \in [105, 170]$ m in the NEWCOL selection and as $Z_{vtx} \in [105, 165]$ m in the OLDCOL selection, the plot in Figure 3.11 shows that there is a negligible amount of signal events in $Z_{vtx} \in [105, 110]$ m after the selection: that is why the trapezoidal cut is applied at $Z_{vtx} > 110$ m.

Even if this selection has been optimized for the NEWCOL configuration, it is used nevertheless for the OLDCOL, for symmetry reasons and since the performance is similar.

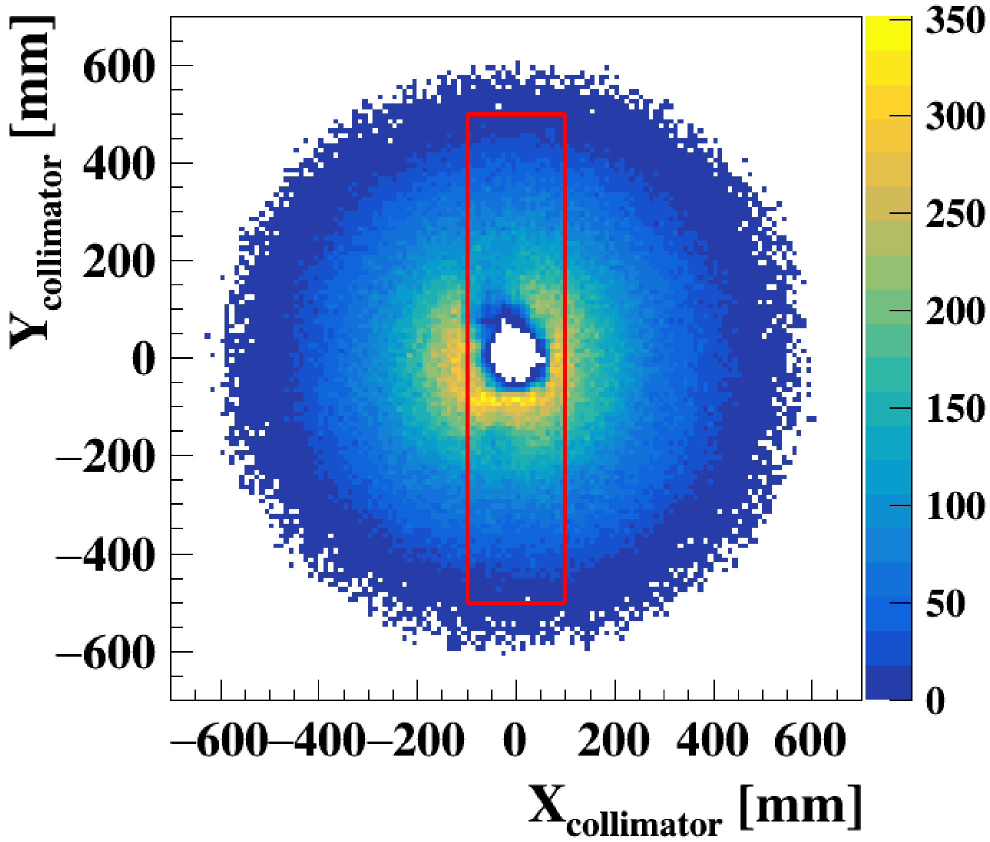

Figure 3.9: Distribution of $(X, Y)_{Coll}$ for MC $K^+ \to \pi^+ \nu\bar{\nu}$ events at the end of the NEWCOL selection (including the application of the BDT selection). The red box represents the cut-based OLDCOL selection: all the events inside the box are rejected, with an important loss of signal acceptance with respect to the BDT approach. Figure from [36].

3.9 Selection on Z_{vtx}

The Z_{vtx} variable is crucial for the rejection of two other background categories, the $K^+ \to \pi^+\pi^0$ and the $K^+ \to \pi^+\pi^-e^+\nu$ decays, also exploiting the correlation with the π^+ momentum and the photon/multiplicity rejection (described later).

Concerning the $K^+ \to \pi^+\pi^0$ decays, to a small π^+ momentum corresponds a high π^0 momentum. In this situation it is more probable to find one low energy photon and one high energy photon coming from the $\pi^0 \to \gamma\gamma$ decay. This increases

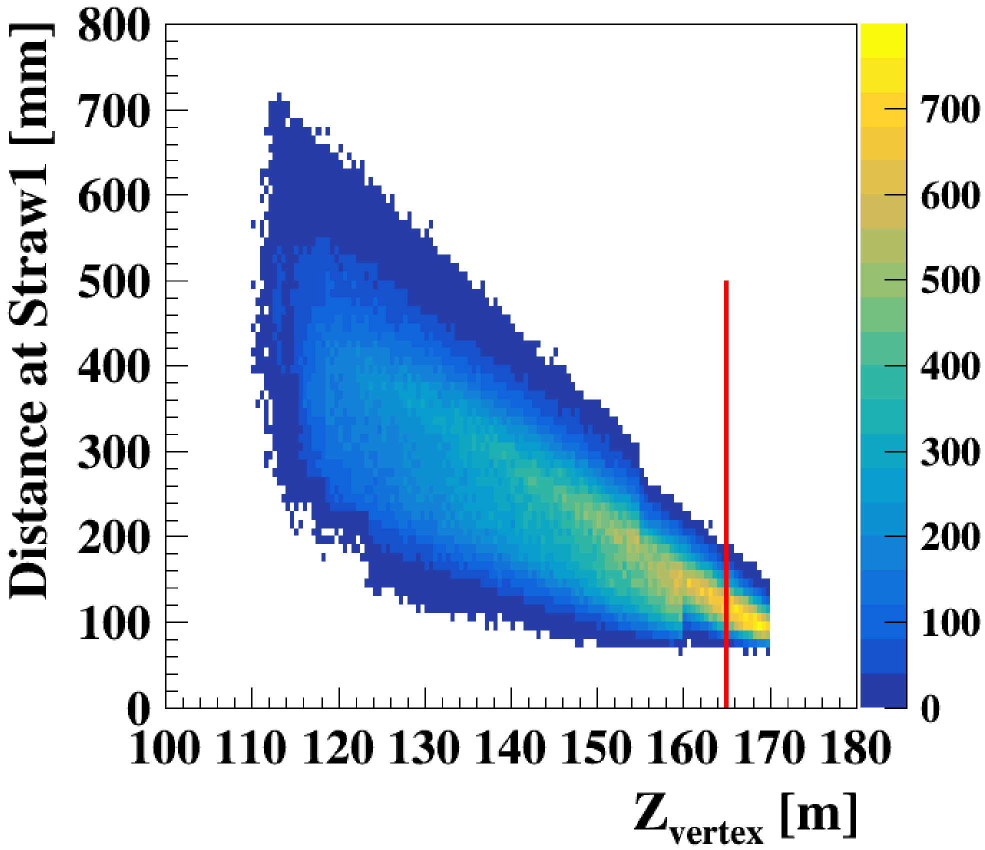

Figure 3.10: Distribution of (Z_{vtx}, R_{Straw1}) for MC $K^+ \to \pi^+\nu\bar{\nu}$ events at the end of the NEWCOL selection (including the application of the BDT selection). The red line represents the cut-based OLDCOL selection: all the events at $Z_{vtx} > 165$ m are rejected, with an important loss of signal acceptance with respect to the BDT approach. Figure from [36].

the probability to loose both photons (that means a possible background event for $K^+ \to \pi^+\nu\bar{\nu}$ selection), in particular if the decay happens at the end of the fiducial decay region, because the high energy photon could travel along the beam-pipe and the small energy photon could go undetected between two LAV stations. In conclusion, the $K^+ \to \pi^+\nu\bar{\nu}$ selection is more contaminated by the $K^+ \to \pi^+\pi^0$ background at small π^+ momentum and high Z_{vtx}. Therefore, in order to suppress this background contribution, the condition $Z_{vtx} < 155$ m is applied if $p_{\pi^+} < 20$ GeV/c.

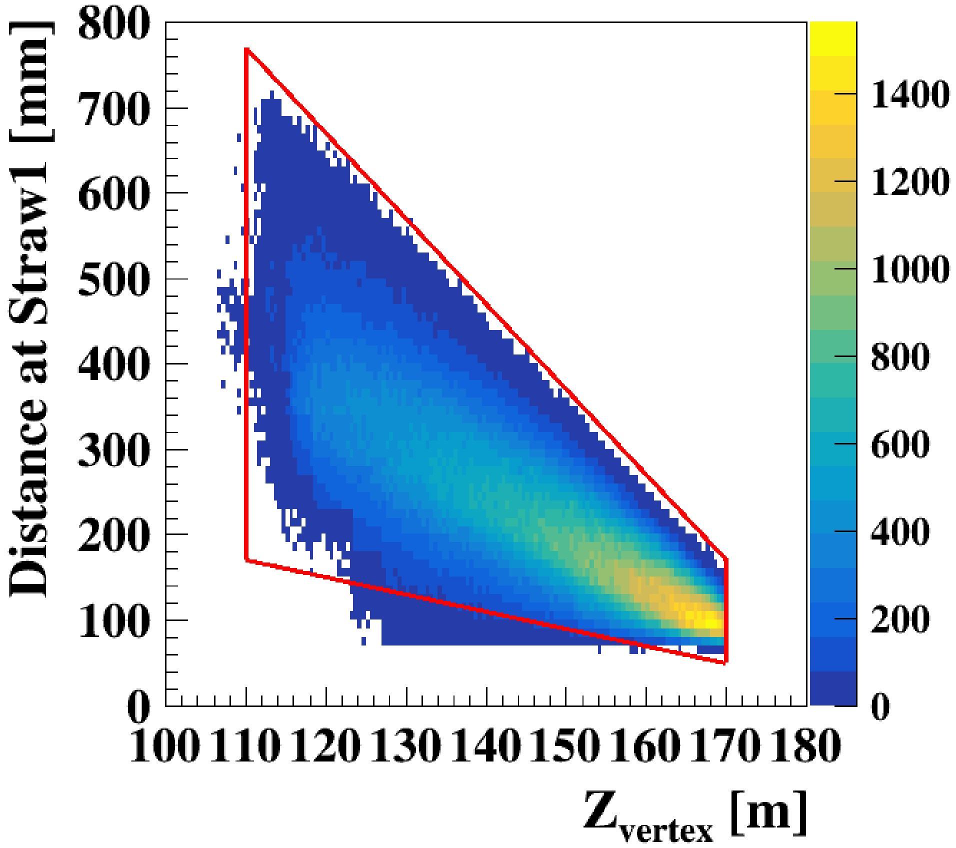

Figure 3.11: Distribution of (Z_{vtx}, R_{Straw1}) for MC $K^+ \to \pi^+\nu\bar{\nu}$ events after the application of the BDT cut. The red lines represent the new trapezoidal cut.

Using similar considerations, the condition $Z_{vtx} < 160$ m is applied if $p_{\pi^+} > 35$ GeV/c for additional suppression of the background coming from $K^+ \to \pi^+\pi^-e^+\nu$ events, as suggested by Monte Carlo studies.

The effect of the different cuts applied on Z_{vtx} is evident in the discontinuities at 155 m and 160 m visible in Figure 3.10.

3.10 Charged particle identification

The charged particle identification (PID), i.e. muon (and positron) rejection, is performed with different conditions based on quantities measured by independent detectors: the RICH, the electromagnetic calorimeter (LKr), the hadronic calorimeters (MUV1 and MUV2) and the scintillator pads for muon detection (MUV3).

3.10.1 MUV3 and calorimeters usage

The first condition is applied at the trigger level, where anti-coincidence with any signal in MUV3 is required in a ± 6.25 ns time window. A similar requirement is applied in the offline selection in order to recover and minimize possible trigger inefficiency (therefore to minimize difference between PNN sample and CTRL sample, where the MUV3 is not used at the trigger level).

The quantities measured by calorimeters are used as a function of the π^+ momentum, to optimize the μ^+ rejection including the RICH PID and the kinematic rejection of the $K^+ \to \mu^+\nu$ decay. In fact, both the RICH and the kinematics are more powerful at low momenta, while they are less effective at high momenta.

Several calorimetric variables, listed below, are combined by a Boosted Decision Trees algorithm, that returns the probability for a particle to be a pion, a muon or a positron [76]:

- ratios between the calorimetric energy deposited and the particle momentum measured in the STRAW (using both the energy deposited in the single calorimeters and their sum)
- longitudinal and transverse development of the calorimetric showers, including the energy sharing between LKr, MUV1 and MUV2
- distance between the particle impact point and the reconstructed cluster position.

The BDT algorithm is trained on samples of π^+, μ^+ and e^+ selected from CTRL data collected during the 2016 run.

Pion identification requires the π^+ probability to be larger than a certain threshold depending on the momentum and is optimised with data. In Figure 3.12 pion and muon selection efficiencies corresponding to $P(\pi) > 0.8$ are reported, as a function of the charged particle momentum.

In order to avoid overtraining due to potential differences between the training and the physics samples, some a-priori cuts, which insist on the same variables used in the BDT, are applied.

The optimization performed in the 2018 analysis leads to the definition of two sets of conditions: the softer set is applied if $p_{\pi^+} < 35$ GeV/c, the tighter set is applied otherwise.

As average performance, the usage of calorimeters and MUV3 provides a muon (background) efficiency of $\epsilon(\mu) \sim 10^{-5}$ for a pion (signal) efficiency of $\epsilon(\pi) \sim 0.82$ in the momentum range used in the $K^+ \to \pi^+\nu\bar{\nu}$ selection.

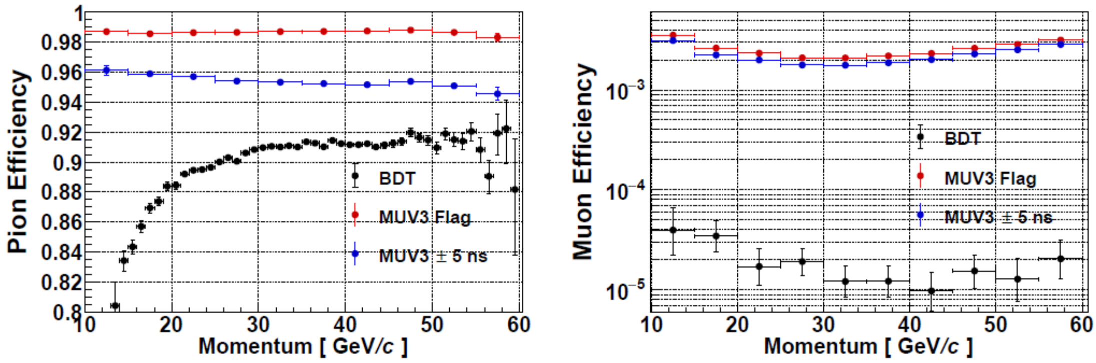

Figure 3.12: Pion and muon efficiencies as a function of the momentum after applying a MUV3 veto and with the pion identification using the calorimeters BDT probability ($P(\pi) > 0.8$). Figure from [76].

3.10.2 RICH usage

As already mentioned in the description of the downstream track reconstruction, two different approaches are used for the Cherenkov ring reconstruction in the RICH detector.

In the first approach, starting from the STRAW track, the ring center is extrapolated and then, assuming different mass hypotheses (positron, muon, pion, kaon) the expected ring radius is computed inverting the formula in Equation 2.3, using the track momentum measured by the STRAW spectrometer. The different expected rings are then compared with the hits observed in the RICH PMs plane and a likelihood value for each mass hypothesis is determined. All the likelihood values are then divided by the highest value, in order to normalize the most likelihood hypothesis to 1 and all the others to a value between 0 and 1. In order to classify a particle as a pion, a likelihood discriminant is defined as the likelihood value of the most probable not-pion hypothesis: $Lh(!\pi)$, that should satisfy the condition $Lh(!\pi) < \alpha$, with $\alpha < 1$. The value of the threshold α is optimized in bins of π^+ momentum. This approach is very powerful in terms of π^+/μ^+ separation, but it strongly depends on the STRAW spectrometer, not only for the momentum measurement, but also for the ring center determination.

The second approach is less STRAW-dependent, since starting from the RICH hits, the ring center and radius are determined with a χ^2 fit procedure that does not depend on other detectors. Then the charged particle mass is measured using Equation 2.3, where the track momentum is still measured by the STRAW spectrometer. A cut on the measured mass is used to distinguish pions from muons.

The rings reconstructed with both methods are shown in Figure 3.13 for a $K^+ \to \pi^+\nu\bar{\nu}$ candidate in 2017 data. The $Lh(!\pi)$ distributions in pions and muons control samples (2017 data) are shown in Figure 3.14, while the mass reconstructed with the RICH detector in the same control samples is shown in Figure 3.15.

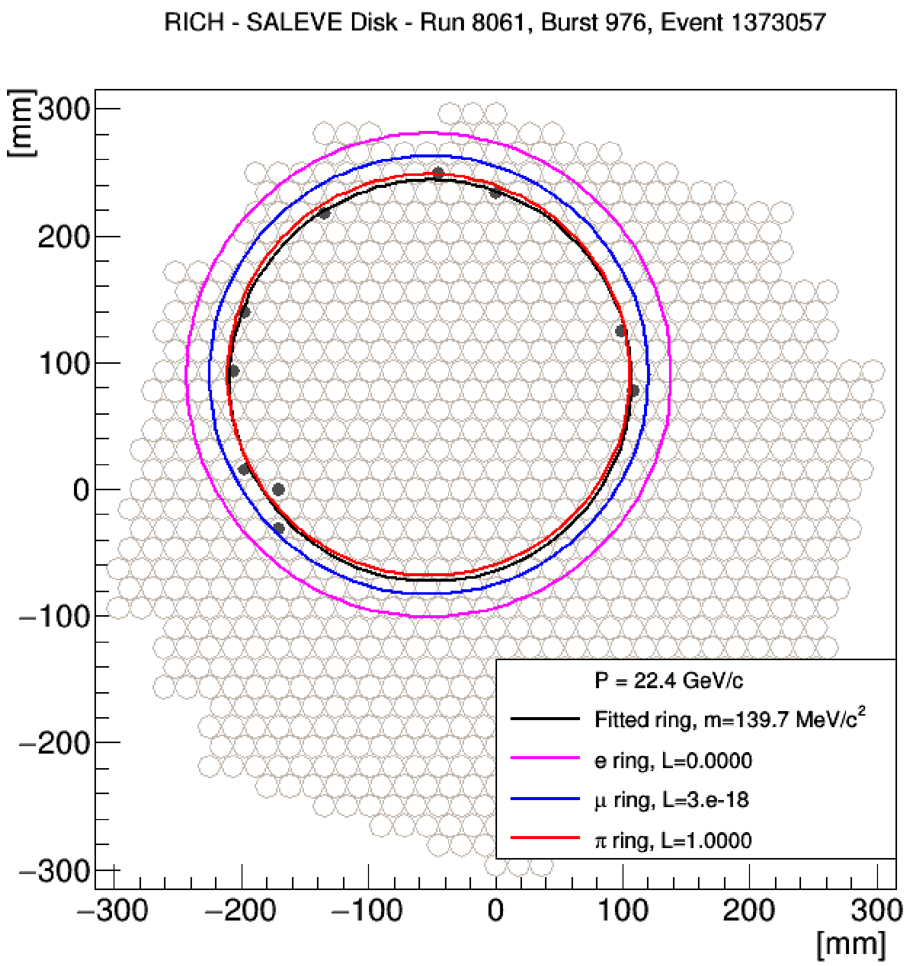

Figure 3.13: One of the two RICH PM disk planes, where a $K^+ \to \pi^+\nu\bar{\nu}$ candidate in 2017 data is displayed. The hits from Cherenkov photons are represented by black circles with a radius equal to the single hit resolution (4.7 mm). The ring reconstructed by the fit algorithm (black) is compared to the expected rings for positrons (magenta), muons (blue) and pions (red). Figure from [91].

With respect to the 2017 analysis, the selections used for both RICH approaches in the 2018 analysis have been optimized with respect to the π^+ momentum, choosing three different combinations of requirements. The tightest one is applied in the range 25-35 GeV/c, a softer one is applied in the range 15-25 GeV/c, since the muon contamination is suppressed by the kinematic selection criteria: the softest

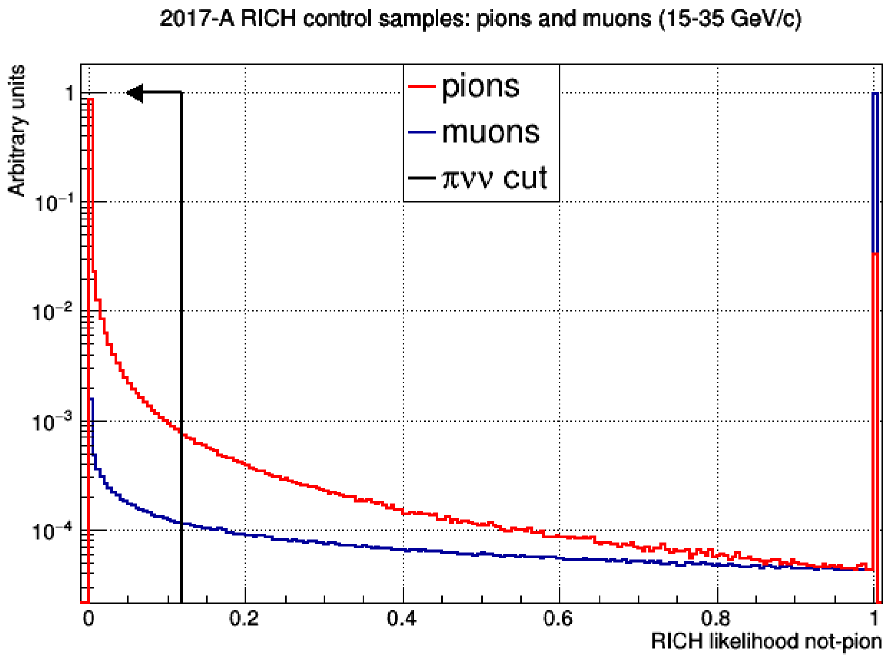

Figure 3.14: $Lh(!\pi)$ reconstructed by the RICH detector, for muons (blue) and pions (red), in 2017 data, in the momentum range 15-35 GeV/c; the cut applied in the 2017 analysis is shown in black. Both distributions are normalized to 1. Figure from [91].

one is applied in the range above 35 GeV/c, since the RICH π/μ separation power decreases at high momenta, as shown in Figure 2.13. For each bin the optimization is performed in the control samples, setting the level of background rejection needed and finding the combination of cuts on the two mentioned variables that yields the highest signal efficiency.

The optimization leads to the following average performance for the RICH π/μ separation in the momentum range 15-45 GeV/c, including also the 35-45 GeV/c momentum region, where the RICH is less efficient (to be compared with Equation 2.4):

$$\epsilon(\pi) \simeq 85\% \; at \; \epsilon(\mu) \simeq 0.3\% \tag{3.1}$$

3.11 Photon and multiplicity rejection

The photon and multiplicity rejection is a crucial part of the selection, in particular for the suppression of the background coming from $K^+ \to \pi^+\pi^0$ decay.

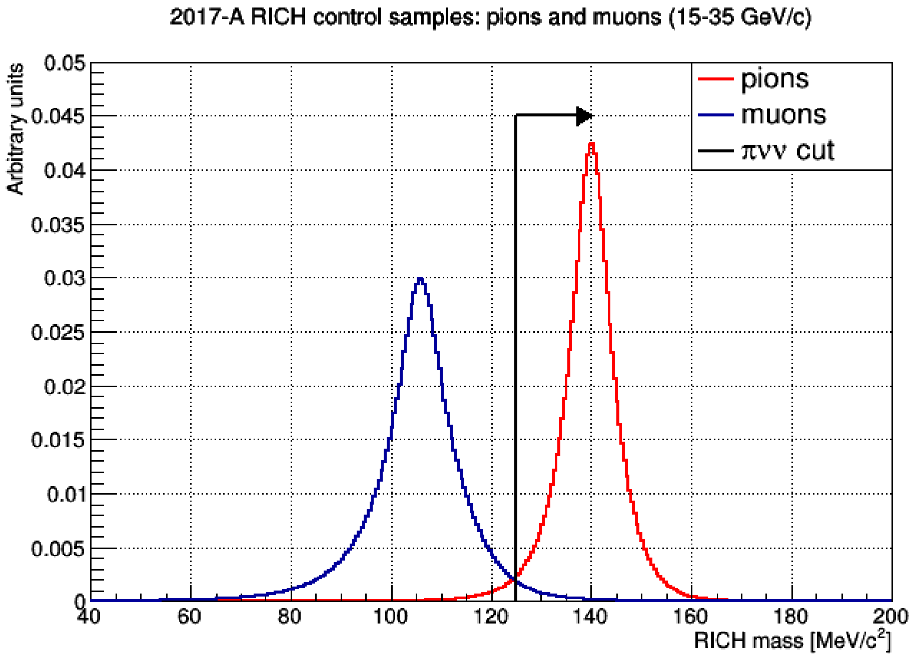

Figure 3.15: Charged particle mass reconstructed by the RICH detector, for muons (blue) and pions (red), in 2017 data, in the momentum range 15-35 GeV/c; the cut applied in the 2017 analysis is shown in black. Both distributions are normalized to 1. Figure from [91].

3.11.1 Photon rejection

The photon rejection is accomplished with the LAV, LKr, IRC and SAC detectors, depending on the angle at which the photon is emitted in the kaon decay, as shown in Figure 2.18.

An LKr cluster is associated to a photon if it is at least 100 mm far from the track impact point at the LKr plane, within a time window defined as a function of the cluster energy, from ±5 ns below 1 GeV, to ±50 ns above 15 GeV. These large time windows are used in order to keep the photon detection inefficiency at high energy under 10^{-5}, and are due to pileup clusters that can overlap in space with the photon cluster, leading to a wrong reconstruction of the photon clusters time, that can be shifted by tens of ns.

The signal in IRC and SAC detectors is read using both TDC and FADC systems; a signal read by the TDC within ±7 ns leads to the rejection of the event, while for the signal read by the FADC also a minimum energy of 1 GeV is required to apply the rejection.

Concerning the LAV, the time window used to look for the coincidence is ±3 ns.

Appropriate combinations of the TDC leading and trailing edges of the high and low threshold channels are exploited to define the LAV signal [75]. An improvement of the signal efficiency (more precisely in the *random veto efficiency*, as described in Section 4.4) with respect to the 2017 analysis has been obtained considering only the signal in the LAV stations located downstream of the reconstructed decay vertex. This is the only change in the photon rejection criteria with respect to the 2017 analysis [34].

3.11.2 Multiplicity rejection

Multiplicity rejection vetoes charged particles emitted by photons interacting in the material before reaching the calorimeters (first category) and events with more than one charged particle in the final state, e.g. $K^+ \to \pi^+\pi^+\pi^-$ decays, where tracks are only partially reconstructed in the STRAW (second category).

For the first category, the rejection criteria exploit the time and spatial coincidence of isolated signals reconstructed in at least two of the NewCHOD, CHOD and LKr detectors, since signal from charged particles is expected in the detectors downstream of the STRAW. Signals in the MUV0 and HASC detectors in time coincidence are also included.

For the second category, the charged particles leave signal only in the two STRAW chambers before the magnet or in the other two STRAW chambers after the magnet, so-called *segments*, compatible with a particle coming from a kaon decay in the fiducial volume.

An improved algorithm for *segments* reconstruction in the 2018 analysis brought to an increase in the signal efficiency, as described in Section 4.4.

3.11.3 π^0 rejection performance

The hermeticity of the NA62 detector provides a global inefficiency of π^0 rejection $\eta_{\pi^0} \sim 2 \cdot 10^{-8}$ (average in the full momentum range 15-45 GeV/c).

An independent measurement of the π^0 rejection inefficiency has been performed for the search of $\pi^0 \to$ *invisible* process in the $K^+ \to \pi^+\pi^0$ decays [71]: η_{π^0} is measured via Monte Carlo simulation, starting from the inefficiency of a single photon rejection of each photon detection condition, and combining them to obtain an event weight equal to the probability that all the photons escape detection. The result, shown in Figure 3.16, is consistent with the $K^+ \to \pi^+\nu\bar{\nu}$ analysis result within the uncertainty and strongly depends on the momentum. A π^+ above 40 GeV/c corresponds to a π^0 momentum below 35 GeV/c and to a higher probability that one of the photons escapes detection by passing through one of the regions not instrumented between two LAV stations. A π^+ momentum below 20 GeV/c corresponds to a higher probability that one of the two π^0-daughter photons traverses the beam pipe at a grazing angle and converts to an $e^+ - e^-$ pair escaping detection.

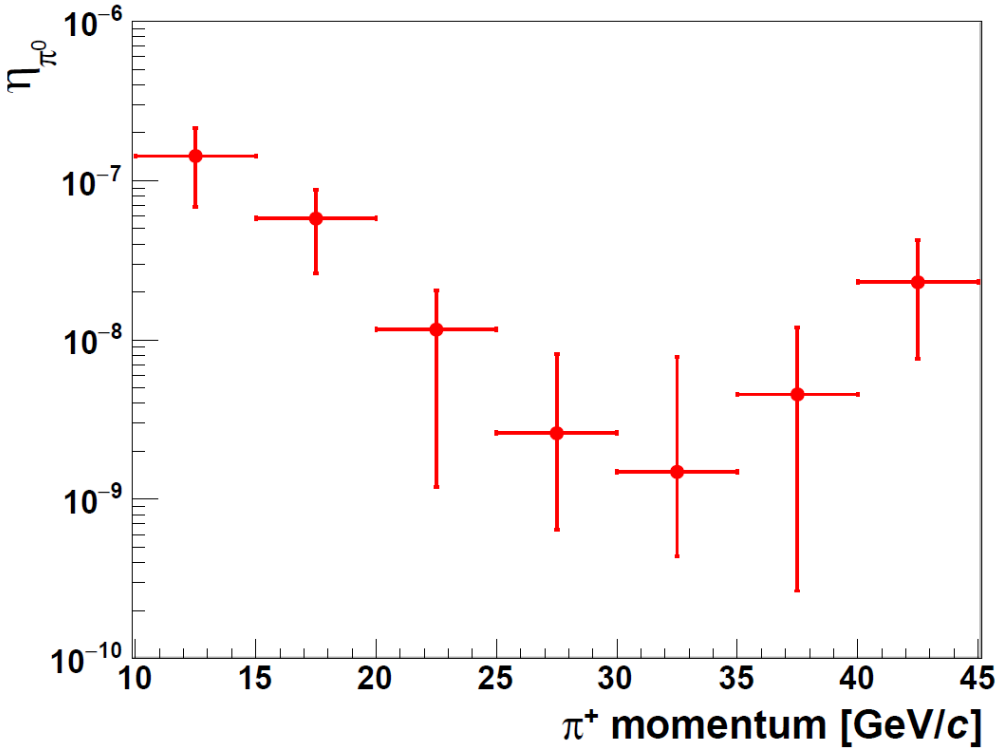

Figure 3.16: Expected π^0 veto inefficiency (η_{π^0}) as a function of the charged pion momentum. Figure from [71].

3.12 Definition of kinematic regions

The last part of the $K^+ \to \pi^+\nu\bar{\nu}$ selection consists in the definition of the kinematic regions in which the signal is searched.

The kinematic distributions (m^2_{miss} variable defined in Equation 2.1) of the signal and of the main kaon decay channels have been already shown in Figure 2.2 and in Figure 3.2.

The (p_{π^+}, m^2_{miss}) distribution of the $K^+ \to \pi^+\nu\bar{\nu}$ events in the MC simulation after the full selection, except for the kinematic region definitions, is shown in Figure 3.17, together with the definition of the two signal regions:

- R1: $p_{\pi^+} \in [15, 35]$ GeV/c and $m^2_{miss} \in [0.000, 0.010]$ GeV^2/c^4
- R2: $p_{\pi^+} \in [15, 45]$ GeV/c and $m^2_{miss} \in [0.026, 0.068]$ GeV^2/c^4

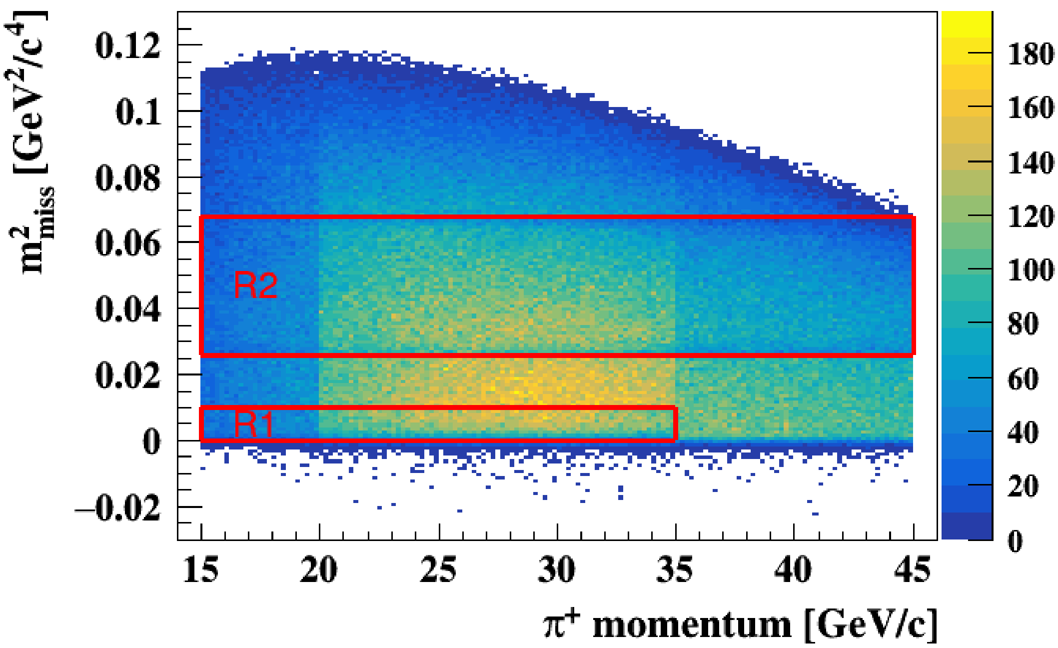

Figure 3.17: Distribution of the Monte Carlo $K^+ \to \pi^+\nu\bar{\nu}$ events in the kinematic plane m^2_{miss} vs P_π, at the end of the 2018-NEWCOL selection, except for the application of the kinematic regions cuts, that correspond to the red boxes: signal region 1 (R1) and signal region 2 (R2). Figure from [36].

Compared to the 2017 analysis, R2 has been extended up to 45 GeV/c, leading to a sizeable improvement of the signal efficiency, while this has not been possible for R1, due to the background contamination from $K^+ \to \mu^+\nu$ decays (Section 5.2).

The discontinuities of the signal distribution along the π^+ momentum bins demonstrate the optimization of the signal selection in bins of π^+ momentum.

The other regions of the phase space are covered by control and background regions, as shown in Figure 3.18. The control regions are always defined between the background and the signal regions, in order to validate the background estimations in the signal regions before unblinding them.

The regions are defined as in Table 3.1.

The $K^+ \to \pi^+\pi^+\pi^-$ background and control regions are defined taking into account the lower limit on m^2_{miss} of the three-body decay that gives [43]:

$$m^2_{miss}(K^+ \to \pi^+\pi^+\pi^-) \geq 4(m_{\pi^\pm})^2 \simeq 0.0779\ GeV^2/c^4 \tag{3.2}$$

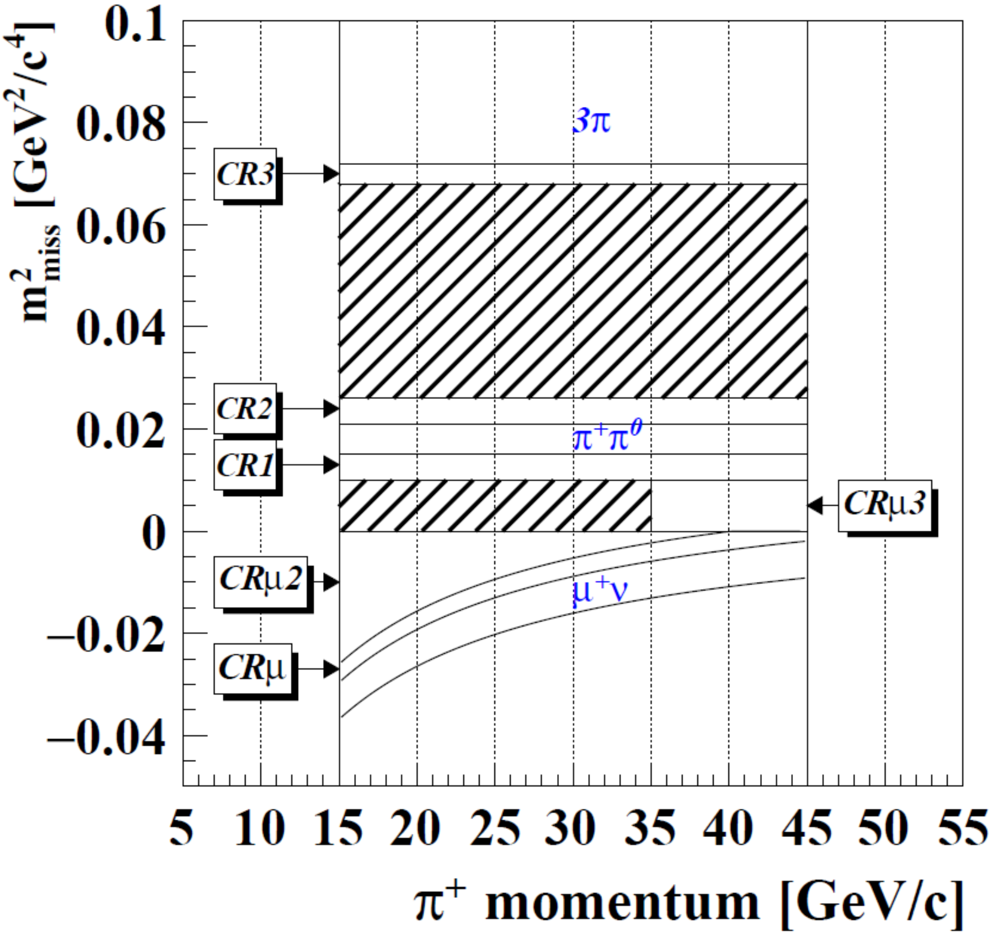

Figure 3.18: Graphical representation of background and control regions in the (p_{π^+}, m^2_{miss}) plane. The hatched areas are Signal Region 1 (lower m^2_{miss}) and Region 2 (higher m^2_{miss}).

and resolution effects on m^2_{miss} measurement.

The $K^+ \to \pi^+\pi^0$ background and control regions are defined using the fact that for this decay the m^2_{miss} variable is related only to the π^0 mass [43]:

$$m^2_{miss}(K^+ \to \pi^+\pi^0) = (m_{\pi^0})^2 \simeq 0.0182\ GeV^2/c^4 \tag{3.3}$$

and applying bands of $\pm 3\sigma$ for the background region and $\pm 8\sigma$ for the control regions, where $\sigma \simeq 10^{-3}\ GeV^2/c^4$ is the experimental resolution of the m^2_{miss} variable in those regions.

Concerning the $K^+ \to \mu^+\nu$ decay, remembering that m^2_{miss} is computed under the assumption of the charged pion mass hypothesis for the downstream track (Equation 2.1), it is possible to express analytically the m^2_{miss} variable as a function of the track momentum, as follows:

$$m^2_{miss}(K^+ \to \mu^+\nu) = m^2_{\mu-miss} = (m^2_{\pi^+} - m^2_{\mu^+})\left(1 - \frac{p_{K^+}}{p_{\pi^+}}\right) \quad (3.4)$$

where p_{K^+} is the nominal kaon momentum, equal to 75 GeV/c.

Since the experimental resolution on the m^2_{miss} variable is worse for small values of m^2_{miss} and improves at high values of m^2_{miss} , it is useful to define the quantity $\sigma_\mu = 1.2 \cdot 10^{-3}\ GeV^2/c^4$, that corresponds to an estimation of the resolution on the m^2_{miss} variable in the $K^+ \to \mu^+\nu$ region, used for the definition of the corresponding control regions.

The formula in Equation 3.4 illustrates the behavior of the m^2_{miss} of $K^+ \to \mu^+\nu$ decays as a function of the track momentum in Figure 3.2: at high momenta the difference between charged pion and muon masses becomes negligible, therefore m^2_{miss} is close to 0 (mass of the neutrino in the $K^+ \to \mu^+\nu$ decay) even if computed under the pion mass hypothesis; on the other hand at low momenta the masses difference strongly affects the m^2_{miss} computation, that deviates significantly from 0.

The regions $CR\mu2$ and $CR\mu3$ are defined to fully cover the rest of the phase space of interest for the $K^+ \to \pi^+\nu\bar{\nu}$ search.

Region	p_{π^+} $[GeV/c]$	m^2_{miss} $[GeV^2/c^4]$
$K^+ \to \mu^+\nu$	$(15, 45)$	$m^2_{\mu-miss} \pm 3\sigma_\mu$
$CR\mu$	$(15, 45)$	$(m^2_{\mu-miss} + 3\sigma_\mu, min(0, m^2_{\mu-miss} + 6\sigma_\mu))$
$CR\mu2$	$(15, 40)$	$(min(0, m^2_{\mu-miss} + 6\sigma_\mu), 0)$
$CR\mu3$	$(35, 45)$	$(0.000, 0.010)$
$R1$	$(15, 35)$	$(0.000, 0.010)$
$CR1$	$(15, 45)$	$(0.010, 0.015)$
$K^+ \to \pi^+\pi^0$	$(15, 45)$	$(0.015, 0.021)$
$CR2$	$(15, 45)$	$(0.021, 0.026)$
$R2$	$(15, 45)$	$(0.026, 0.068)$
$CR3$	$(15, 45)$	$(0.068, 0.072)$
$K^+ \to \pi^+\pi^+\pi^-$	$(15, 45)$	> 0.072

Table 3.1: Regions in the (p_{π^+}, m^2_{miss}) plane. The quantities $m^2_{\mu-miss}$ and σ_μ are defined in the text.

Only for the signal regions definition, two additional conditions are used to constrain the kinematic reconstruction of the decay, using two different ways of computing the m^2_{miss} variable with respect to Equation 2.1:

$$m^2_{miss}[beam] = (P^{beam}_K - P_\pi)^2 \quad (3.5)$$

$$m^2_{miss}[RICH] = (P_K - P_\pi^{RICH})^2 \quad (3.6)$$

where in P_K^{beam} the nominal beam parameters are used instead of the measurement from the GTK detector. In the P_π^{RICH} computation only the direction of the pion momentum is given by the STRAW spectrometer, while the momentum module is measured by the RICH inverting the Equation 2.3 under the pion mass hypothesis. This procedure is also called *signal regions* $m^2_{miss} - 3d$ *definition* and it used to take under control the effects of the resolution on the measurements of kaon and pion momenta in GTK and STRAW, respectively. Since the resolution of those variables is worse with respect to the standard m^2_{miss} and depends on the track momentum, the $m^2_{miss} - 3d$ definition is set as reported in Table 3.2.

Region	m^2_{miss}	$m^2_{miss}[beam]$	$m^2_{miss}[RICH]$
$R1,\ p < 20\ GeV/c$	$(0.000, 0.010)$	$(-0.005, 0.0135)$	$(0.000, 0.010)$
$R1,\ p \in [20, 25]\ GeV/c$	$(0.000, 0.010)$	$(-0.005, 0.0135)$	$(0.000, 0.020)$
$R1,\ p > 25\ GeV/c$	$(0.000, 0.010)$	$(0.000, 0.0135)$	$(-0.005, 0.020)$
$R2$	$(0.026, 0.068)$	$(0.024, 0.068)$	$(0.020, 0.070)$

Table 3.2: Definition of signal regions with extra constraints on $m^2_{miss}[beam]$ and $m^2_{miss}[RICH]$. m^2_{miss} expressed in GeV^2/c^4.

In order to have the possibility to cross-check the effect of the $m^2_{miss} - 3d$ definition of signal regions, another control region called CR-3d is defined as:

- events with $m^2_{miss} \in [0.000, 0.010]\ GeV^2/c^4$ and $p_{\pi^+} \in [15, 35]\ GeV/c$ but not in R1; or
- events with $m^2_{miss} \in [0.026, 0.068]\ GeV^2/c^4$ and $p_{\pi^+} \in [15, 45]\ GeV/c$ but not in R2.

The control region CR-3d is not displayed in Figure 3.18, since it should be inside the signal regions R1 and R2 in the (p_{π^+}, m^2_{miss}) plane.

3.13 Events after the $K^+ \to \pi^+\nu\bar{\nu}$ selection

The events meeting the criteria of the $K^+ \to \pi^+\nu\bar{\nu}$ selection in the full 2018 data sample are reported in Figure 3.19, where all the control and the signal regions are still blinded, together with the signal acceptance obtained with Monte Carlo simulation (from Figure 3.17). The events inside the background regions are fundamental for the estimation of the background contamination in the signal region, as described in Chapter 5.

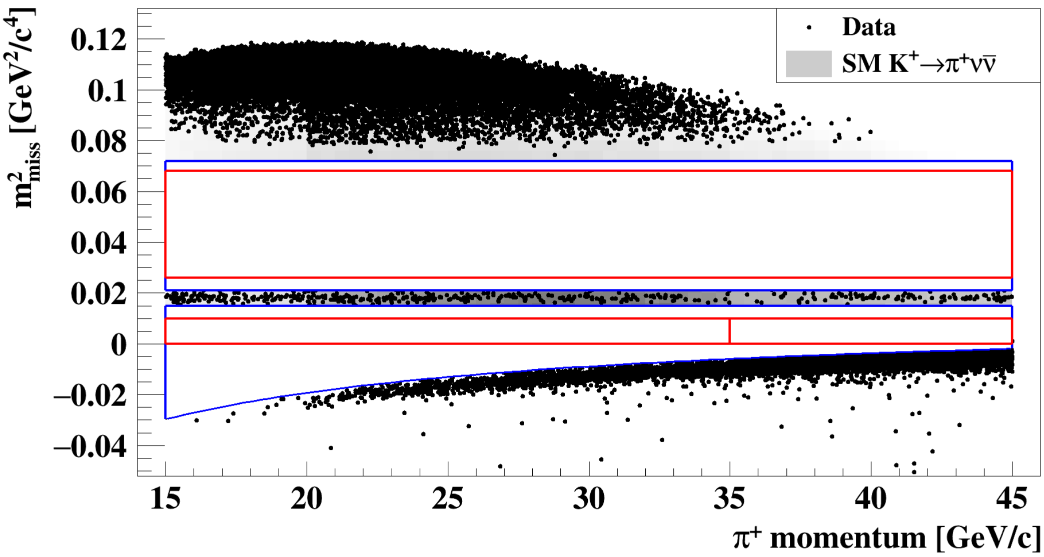

Figure 3.19: Events from the full 2018 data sample that pass the full $K^+ \to \pi^+ \nu\bar{\nu}$ selection in the (p_{π^+}, m^2_{miss}) plane, with control and signal regions blinded. The grey area represents the $K^+ \to \pi^+ \nu\bar{\nu}$ acceptance from the Monte Carlo simulation. Figure from [36].

3.14 Normalization selection

The normalization channel $K^+ \to \pi^+\pi^0$ is selected using as much as possible the same criteria as for the signal, in order to cancel systematic effects that are symmetric for the two selections: only the photon and multiplicity rejection criteria are not applied and a *normalization* kinematic region is defined as:

$$Norm.\ region = (CR1) \bigcup (K^+ \to \pi^+\pi^0\ bkg\ region) \bigcup CR2 \qquad (3.7)$$

Moreover, the normalization selection is not applied to the PNN data, but it is applied to the CTRL data.

Chapter 4

The $K^+ \to \pi^+\nu\bar{\nu}$ Single Event Sensitivity

This chapter is dedicated to the signal estimation, based on the selection described in Chapter 3.

In order to determine the expected number of signal events, the measurement of the *Single Event Sensitivity (SES)* is needed, defined as the branching fraction that the process should have in order to expect 1 signal event under the achieved experimental conditions:

$$Br_{\pi\nu\nu} = N_{\pi\nu\nu} \cdot SES \tag{4.1}$$

where $Br_{\pi\nu\nu}$ and $N_{\pi\nu\nu}$ are the branching ratio and the number of events of the $K^+ \to \pi^+\nu\bar{\nu}$ process.

From the experimental point of view, the SES is computed as follows:

$$SES = \frac{1}{N_K \cdot \sum_j (A_{\pi\nu\nu\ j} \cdot \epsilon^{trig}_{\pi\nu\nu\ j} \cdot \epsilon^{RV}_{\pi\nu\nu\ j})} \tag{4.2}$$

where N_K is the effective number of collected kaon decays and the product of the other three terms represents the global efficiency of the signal selection: $A_{\pi\nu\nu}, \epsilon^{trig}_{\pi\nu\nu}, \epsilon^{RV}_{\pi\nu\nu}$; j is the index of the bin (5 GeV/c size) in the π^+ momentum range. The SES measured with this procedure does not depend on the $Br(K^+ \to \pi^+\nu\bar{\nu})$ Standard Model calculation.

The number of expected Standard Model signal events, measured inverting Equation 4.1 and inserting the Standard Model prediction for $Br(K^+ \to \pi^+\nu\bar{\nu})$ (Equation 1.17),

$$N^{exp}_{SM}(K^+ \to \pi^+\nu\bar{\nu}) = \frac{Br^{SM}(K^+ \to \pi^+\nu\bar{\nu})}{SES} \tag{4.3}$$

is therefore affected by the external uncertainty due to the Standard Model Br prediction.

4.1 Effective number of kaon decays

The first physics quantity needed in the $Br(K^+ \to \pi^+\nu\bar{\nu})$ measurement is the number of collected kaon decays in the analyzed sample, used to normalize the number of observed signal candidates. This quantity is computed exploiting an other kaon decay channel, defined as *normalization channel*, that should satisfy the following requirements in order to introduce the smallest possible uncertainty in the final measurement:

- its Br is precisely known
- its selection is as much as possible similar to the signal selection
- the selected sample is large enough to introduce a negligible statistical uncertainty
- the selected sample is as much as possible free of background contamination.

The best normalization channel for the $Br(K^+ \to \pi^+\nu\bar{\nu})$ measurement is the $K^+ \to \pi^+\pi^0$ decay: the two channels are selected using very similar criteria, as described in the previous chapter, leading to the cancellation of several systematic effects in the normalization process; moreover, the $K^+ \to \pi^+\pi^0$ branching ratio (Table 2.1) is 9 orders of magnitude larger than the signal and it is precisely measured (uncertainty at the level of 0.4%). As a consequence the statistical and the external uncertainties introduced in the final measurement by the normalization are negligible.

The PNN trigger is not suitable to select the $K^+ \to \pi^+\pi^0$ decays, since it is based on conditions on the NewCHOD and LKr detectors to veto photons coming from the $\pi^0 \to \gamma\gamma$ decay. The minimum-bias trigger mask (CTRL trigger) is then exploited, with the only disadvantage given by the applied down-scaling factor $D_{trig} = 400$.

The number of collected kaon decays can be measured as:

$$N_K = \frac{N_{\pi\pi} \cdot D_{trig}}{A_{\pi\pi} \cdot Br_{\pi\pi}} \tag{4.4}$$

where $N_{\pi\pi}$ is the number of selected normalization events, $A_{\pi\pi}$ is the acceptance of the normalization selection measured with Monte Carlo simulations and $Br_{\pi\pi}$ is the branching ratio of the normalization channel (Table 2.1).

The efficiency of the CTRL trigger with respect to the normalization selection is measured to be 1 within the uncertainty, therefore it is not included in Equation 4.4.

$A_{\pi\pi}$ is computed using the Monte Carlo simulation of the normalization channel, as the ratio between the number of events that pass the full normalization selection and the number of generated events in the fiducial decay volume: $Z_{decay} \in [105; 170]\ m$.

Since the Monte Carlo simulation does not exactly reproduce all effects (e.g., the accidental activity in the detectors that generates selection inefficiency not properly taken into account in the $A_{\pi\pi}$ factor), the quantity N_K defined in Equation 4.4 represents an effective number of collected kaon decays. The adjective *effective* means that even if it is not the true number of collected kaon decays, all the factors that are not properly taken into account in $A_{\pi\pi}$ enter exactly in the same way in the measurement of $A_{\pi\nu\nu}$, therefore they cancel and do not affect the final $Br(K^+ \to \pi^+\nu\bar{\nu})$ measurement. As an example, effects not properly simulated are:

- inefficiency in the reconstruction of the detectors KTAG, STRAW, RICH, CHOD;
- random veto due to extra activity in CHANTI and MUV3 detectors;
- random veto due to pile-up activity in the GTK detector, only partially reproduced in the Monte Carlo simulations.

All selection conditions related to the above effects are the same for signal and normalization samples, as described in the previous chapter, in order to avoid any impact on the final $Br(K^+ \to \pi^+\nu\bar{\nu})$ measurement.

The systematic uncertainty of the $A_{\pi\pi}$ factor, due to the effects not properly simulated, is estimated to be 10% relative. The same uncertainty, for the same reason, affects the signal acceptance, but then the contribution of those uncertainties to the SES measurement decreases up to 3.5% (Table 4.4), thanks to the cancellation of the effects in the normalization process.

The uncertainty of the N_K measurement given by the background contamination of the normalization sample is smaller than 1%, therefore negligible compared to the uncertainty due to the acceptance estimation, and it is included in the error budget of the SES measurement (Table 4.4).

The results of the N_K measurement for the two 2018 data sub-samples, with the factors entering in Equation 4.4 are summarized in Table 4.1.

	2018-OLDCOL	2018-NEWCOL
$N_{\pi\pi}$	$3.14 \cdot 10^7$	$11.6 \cdot 10^7$
$A_{\pi\pi}$	$(7.62 \pm 0.77)\%$	$(11.8 \pm 1.2)\%$
N_K	$(0.8 \pm 0.1) \cdot 10^{12}$	$(1.9 \pm 0.2) \cdot 10^{12}$

Table 4.1: Results of the measurements of the physics quantities in Equation 4.4.

4.2 Acceptance of the signal selection

The global efficiency of the signal selection is given by the product of the three terms in Equation 4.2: $A_{\pi\nu\nu}, \epsilon^{trig}_{\pi\nu\nu}, \epsilon^{RV}_{\pi\nu\nu}$.

All the considerations illustrated in the previous section concerning the acceptance of the normalization sample apply to the term $A_{\pi\nu\nu}$ in Equation 4.2, also measured with Monte Carlo.

The increase of this factor with respect to the analysis of the 2017 data is the main reason of the improvement in the $K^+ \to \pi^+\nu\bar{\nu}$ sensitivity achieved by the NA62 experiment in the 2018 analysis, and most of the efforts in the selection optimization illustrated in the previous chapter are aimed to that.

The acceptance measurement is performed splitting the signal regions in 5 GeV/c size π^+ momentum bins, in order to optimize the momentum dependent selection criteria. The plot in Figure 3.17 shows the distribution of the Monte Carlo $K^+ \to \pi^+\nu\bar{\nu}$ events in the kinematic plane m^2_{miss} vs p_π, at the end of the selection, but before any cut on the kinematic regions. The distributon is not smooth in the different momentum bins as a consequence of the optimization of the selection described in the previous chapter.

The results of the signal acceptance measurement in each π^+ momentum bin are reported in Table 4.2 and 4.3, together with the other contributions to the global signal efficiency. They are also illustrated in Figure 4.1, separately for the two signal regions. Integrating over the full π^+ momentum range gives as global acceptance: $A_{\pi\nu\nu} = (4.0 \pm 0.4)\%$ for the 2018-OLDCOL selection, $A_{\pi\nu\nu} = (6.4 \pm 0.6)\%$ for the 2018-NEWCOL selection.

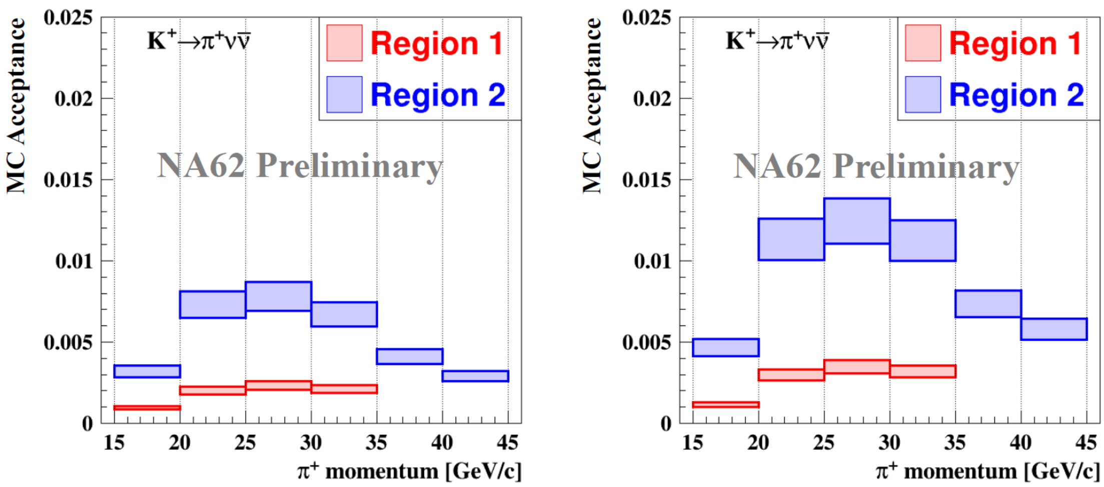

Figure 4.1: Signal selection acceptance measured with MC simulation, for 2018-OLDCOL selection (Left) and 2018-NEWCOL selection (Right), in bins of π^+ momentum for the two signal regions. Figure from [36].

The comparison between data and MC for the normalization selection is shown in Figure 4.2: the not perfect data-MC agreement leads to a systematic uncertainty of 10% relative applied to the measurements of the selection acceptances.

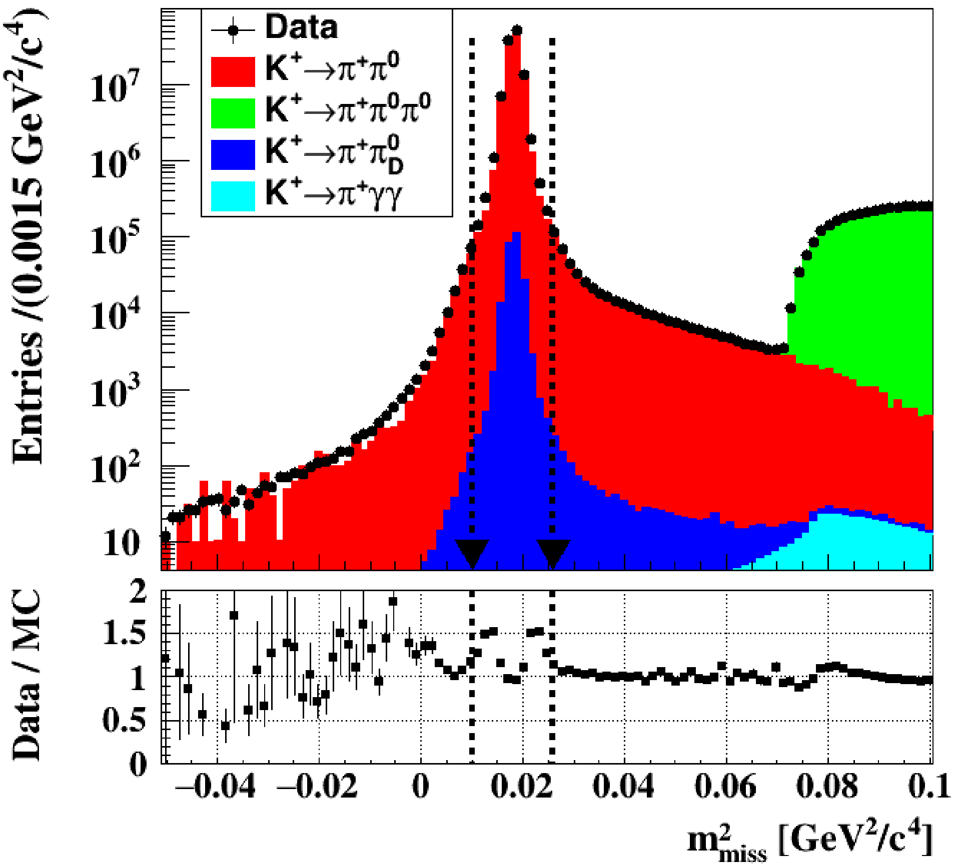

Figure 4.2: Comparison between data and MC simulations for the normalization selection. Figure from [36].

Most of the effects that cause the data-MC disagreement (such as π^+ identification and reconstruction, detectors efficiencies, K^+ identification and reconstruction, loss of acceptance due to beam-related effects) are similar for signal and normalization selections, therefore they cancel out in the SES computation and do not affect the SES measurement. The systematic uncertainty of the SES due to the MC-based acceptance determination is assigned cheking the stability of the SES varying the selection criteria in the region with the highest discrepancy. This uncertainty is 3.5% relative, as reported in Table 4.4.

4.3 Trigger efficiency

The term $\epsilon_{\pi\nu\nu}^{trig}$ in Equation 4.2 is the efficiency of the PNN trigger mask. Since the normalization selection exploit the CTRL trigger, the trigger inefficiencies do not cancel in the normalization process.

The efficiency of the PNN trigger mask is given by the efficiency of the single detectors involved both at L0 and L1, and are measured as a function of the π^+ momentum with the same procedure of the 2017 analysis, described in [34]: each contribution is studied separately being independent quantities and then they are multiplied.

The trigger performance at L0 is measured exploiting a $K^+ \to \mu^+\nu$ sample and a $K^+ \to \pi^+\pi^0$ sample with the $\gamma\gamma$ pair (coming from the π^0 decay) detected in the LAV stations, both selected with the minimum biased trigger.

Excluding the LKr, the main source of trigger inefficiency comes from the MUV3 veto criteria, in fact the effective veto timing window can be larger online than offline due to online time resolution. The uncertainty of the measured value is at the level of 0.5%, is mostly systematic and is due to the deviation of the efficiency from linearity. The global L0 efficiency with the LKr excluded is about 0.98.

Since the trigger response for the LKr is momentum dependent, and the considered $K^+ \to \pi^+\pi^0$ sample contains events with more energetic π^+ with respect to the standard π^+ momentum distribution of the $K^+ \to \pi^+\nu\bar{\nu}$ events, a conversion procedure is needed. The LKr trigger efficiency is measured as a function of the energy that the π^+ deposits in the LKr calorimeter (E_{LKr}): the dependence on E_{LKr} is converted into a dependence on the π^+ momentum, p_{π^+}, with a conversion factor extracted from the E_{LKr}/p_{π^+} distribution of a sample of pions selected from $K^+ \to \pi^+\pi^+\pi^-$ decays.

The global L0 efficiency including the LKr decreases with the increasing of the pion momentum, from ~ 0.95 in the bin 15-20 GeV/c, to ~ 0.85 in the bin 40-45 GeV/c, as expected. This effect is due to the 30 GeV cut applied at L0 on the energy deposited in LKr, that could be triggered by charged pions with higher energies.

Samples of $K^+ \to \mu^+\nu$ selected from minimum-bias data and of $K^+ \to \pi^+\pi^0$ selected from data triggered by the PNN L0 conditions, and then recorded irrespective of the L1 trigger decision, are used to measure the L1 efficiency. After applying the $K^+ \to \pi^+\nu\bar{\nu}$ selection criteria, L1 inefficiency are mostly due to LAV requirements, that introduce intensity-dependent losses of events because the online LAV time resolution requires a larger veto timing window than the one used offline.

The global L1 efficiency is measured to be ~ 0.98, almost flat in the full π^+ momentum range, except for a drop to ~ 0.94 in the last momentum bin (40-45 GeV/c).

The results of the global trigger efficiency (L0+L1) integrated over the full momentum range, are reported in Table 4.2 and 4.3. The relative systematic uncertainty $\sim 5\%$ is related to possible asymmetric effects between the PNN trigger and the CTRL trigger used for the normalization channel. It is measured as the difference of the number of events in the $K^+ \rightarrow \mu^+\nu$ background region, observed after the signal selection without the RICH criteria, in the PNN and the CTRL samples (applying the appropriate re-scaling to compensate the down-scaling factor of the CTRL trigger mask).

4.4 Random veto efficiency

The *Random Veto (RV)* is a signal inefficiency due to accidental activity in some detectors that leads to the rejection of signal-like events. As discussed in the computation of the effective number of collected kaon decays, there are several sources of random veto that affect both the signal and the normalization selections, therefore they cancel in the normalization process. Since some selection criteria (e.g. the photon rejection) are applied only in the signal selection, random rejection of the signal related to these conditions is not taken into account in the normalization process and must be properly included in the SES computation (Equation 4.2).

The quantity $(1 - \epsilon^{RV}_{\pi\nu\nu})$ is defined as the probability of a signal event to be reject by at least one of the cuts against the photon or the multiplicity signals, applied to the signal selection and not to the normalization one, due to extra activity in time with the signal event.

In order to measure the random veto efficiency $\epsilon^{RV}_{\pi\nu\nu}$ directly with the data, no extra activity is added to the downstream detectors in the Monte Carlo simulations, to avoid double counting of the effect.

The RV efficiency is directly measured on data exploiting a clean $K^+ \rightarrow \mu^+\nu$ sample selected on CTRL data, since a $K^+ \rightarrow \mu^+\nu$ event has the same experimental signature of a $K^+ \rightarrow \pi^+\nu\bar{\nu}$ event from the point of view of photon or multiplicity rejection: $\epsilon^{RV}_{\pi\nu\nu}$ is defined as the fraction of events that passes the photon and the multiplicity rejection criteria in the selected $K^+ \rightarrow \mu^+\nu$ sample.

The measured value is $\epsilon^{RV}_{\pi\nu\nu} = 0.66 \pm 0.01$ for both 2018-OLDCOL and 2018-NEWCOL sub-samples, flat in the full π^+ momentum range, as reported in Table 4.2 and 4.3. The uncertainty is systematic and it is due to a correction computed with the Monte Carlo simulations in order to take into account the different effect on RV given by the radiative corrections in the $K^+ \rightarrow \mu^+\nu$ and $K^+ \rightarrow \pi^+\nu\bar{\nu}$ events ($\sim 1\%$). The RV efficiency decreases with the increasing of the beam intensity, as shown in Figure 4.3: the measured value is an effective average taking into account the average beam intensity of the data sample.

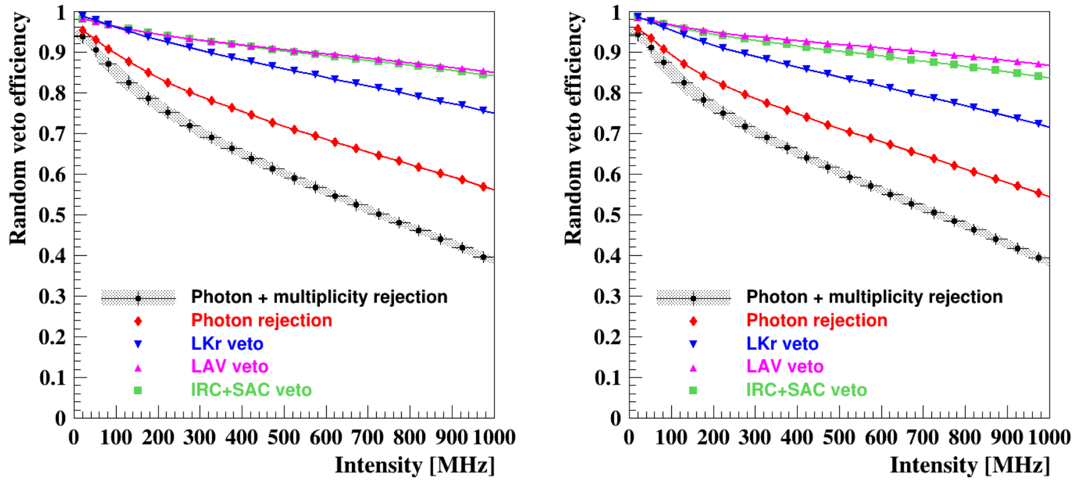

Figure 4.3: Random veto efficiency $\epsilon^{RV}_{\pi\nu\nu}$ as a function of the beam intensity measured in the OLDCOL (Top) and NEWCOL (Bottom) samples. Different contributions are shown: the global efficiency (photon + multiplicity rejection), the efficiency due to the photon rejection, the single contributions (LKr, LAV, IRC and SAC) to the efficiency due to the photon rejection. Figure from [36].

4.5 Single event sensitivity and number of expected SM signal events

Table 4.2 shows the contributions to the signal efficiency in bins of π^+ momentum, together with the SES and the number of expected SM signal events, computed according to Equation 4.2 and 4.3 (N_K taken from Table 4.1), for the 2018-NEWCOL sub-sample.

P_π [GeV/c]	15-20	20-25	25-30	30-35	35-40	40-45
$A_{\pi\nu\nu}$ [$\times 10^{-2}$]	0.58 ± 0.06	1.43 ± 0.14	1.59 ± 0.16	1.45 ± 0.15	0.74 ± 0.07	0.58 ± 0.06
$\epsilon^{trig}_{\pi\nu\nu}$	0.94 ± 0.05	0.92 ± 0.05	0.90 ± 0.05	0.88 ± 0.04	0.86 ± 0.04	0.78 ± 0.04
$\epsilon^{RV}_{\pi\nu\nu}$	0.66 ± 0.01	0.66 ± 0.01	0.66 ± 0.01	0.66 ± 0.01	0.66 ± 0.01	0.66 ± 0.01
SES [$\times 10^{-10}$]	1.48 ± 0.10	0.59 ± 0.04	0.55 ± 0.04	0.63 ± 0.04	1.22 ± 0.08	1.75 ± 0.11
$N^{exp}_{SM}(K^+ \to \pi^+ \nu\bar{\nu})$	0.56 ± 0.04	1.43 ± 0.09	1.53 ± 0.10	1.32 ± 0.09	0.69 ± 0.04	0.48 ± 0.03

Table 4.2: Contributions to the signal efficiency in bins of π^+ momentum, together with the SES and the number of expected SM signal events, for the 2018-NEWCOL sub-sample.

Table 4.3 shows the single terms of the signal efficiency together with the SES and the number of expected SM signal events, integrated over the full π^+ momentum range, for the 2018-OLDCOL and the 2018-NEWCOL sub-samples.

The results related to the 2018-OLDCOL samples are shown only integrated over the full π^+ momentum range, even if they are computed in bins of π^+ momentum as for the 2018-NEWCOL sample, because the statistics is too small for a statistical treatment in bins of momentum.

	2018-OLDCOL	2018-NEWCOL
N_K [$\times 10^{12}$]	0.8 ± 0.1	1.9 ± 0.2
$A_{\pi\nu\nu}$ [$\times 10^{-2}$]	3.95 ± 0.40	6.37 ± 0.64
$\epsilon^{trig}_{\pi\nu\nu}$	0.88 ± 0.04	0.88 ± 0.04
$\epsilon^{RV}_{\pi\nu\nu}$	0.66 ± 0.01	0.66 ± 0.01
SES [$\times 10^{-10}$]	0.54 ± 0.04	0.14 ± 0.01
$N^{exp}_{SM}(K^+ \to \pi^+\nu\bar{\nu})$	$1.56 \pm 0.10 \pm 0.19_{ext}$	$6.02 \pm 0.39 \pm 0.72_{ext}$

Table 4.3: Contributions to the signal efficiency, together with the SES and the number of expected SM signal events, integrated over the full π^+ momentum range, for the 2018-OLDCOL and the 2018-NEWCOL sub-samples. The number of collected kaon decays is also reported.

Considering both the two sub-samples, the SES achieved in the full 2018 data set for the $K^+ \to \pi^+\nu\bar{\nu}$ search is:

$$SES = (0.111 \pm 0.007_{syst}) \cdot 10^{-10} \tag{4.5}$$

that corresponds to a number of expected Standard Model $K^+ \to \pi^+\nu\bar{\nu}$ events:

$$N^{exp}_{SM}(K^+ \to \pi^+\nu\bar{\nu}) = 7.58 \pm 0.40_{syst} \pm 0.75_{ext} \tag{4.6}$$

The total relative uncertainty on the SES is about 6.5% and it is given by the contributions reported in Table 4.4, previously discussed.

Source	Relative uncertainty on SES
trigger efficiency	5%
MC acceptance	3.5%
random veto efficiency	2%
normalization background	0.7%
instantaneous intensity	0.7%
total	6.5%

Table 4.4: Error budget of SES.

4.6 Comparison with the 2017 data analysis

The same numbers shown in Table 4.3 are reported in Table 4.5 as obtained in the 2017 data analysis [34].

The optimization of the analysis performance, in terms of the signal efficiency gain here reported, is the main goal of the present work.

	2017
N_K [$\times 10^{12}$]	1.5 ± 0.2
$A_{\pi\nu\nu}$ [$\times 10^{-2}$]	3.0 ± 0.3
$\epsilon_{\pi\nu\nu}^{trig}$	0.87 ± 0.03
$\epsilon_{\pi\nu\nu}^{RV}$	0.64 ± 0.01
SES [$\times 10^{-10}$]	0.389 ± 0.024
$N_{SM}^{exp}(K^+ \to \pi^+\nu\bar{\nu})$	$2.16 \pm 0.13 \pm 0.26_{ext}$

Table 4.5: Number of collected kaon decays, signal efficiency factors, SES and number of expected SM signal events, from the 2017 analysis results [34].

The most important improvement between the 2017 and the 2018 analyses is obtained for the signal acceptance.

The first comparison must be performed between the 2017 and the 2018-OLDCOL samples, since the hardware configuration of the data-taking is exactly the same: the $\sim +30\%$ increase of the signal acceptance is due to offline improvements in the analysis procedure. In the 2018-NEWCOL sample a further improvement is achieved, thanks to the installation of the final collimator: the different hardware configuration allows a stronger optimization of the offline analysis relaxing the cuts against the *upstream* background, leading to a global increase on the signal acceptance of $\sim +110\%$ with respect to the 2017 analysis.

As shown in the next chapter, all the improvements on the signal efficiency have been obtained keeping the signal over background ratio (S/B) equal or better than in the 2017 analysis. This strategy has been adopted to optimize the 2018 analysis, in order to safely improve the experimental sensitivity of the $K^+ \to \pi^+\nu\bar{\nu}$ search: in fact the figure of merit of the experimental sensitivity is related to $\sim S/\sqrt{B}$, therefore increasing as much as possible S keeping S/B constant is a conservative way to increase the experimental sensitivity, keeping the background contamination under control.

The changes in the selection that lead to the achieved improvement are described in detail in the previous chapter; here only their impact on the signal efficiency is reported, comparing 2017 and 2018-NEWCOL selections:

- the cuts against the *upstream* background, also exploiting a multi-variate approach, leads to gain of $\sim +50\%$ on the signal acceptance

- the signal region R2 extended up to 45 GeV/c π^+ momentum, provides a gain of $\sim +30\%$ on the signal acceptance
- the optimized charged particle identification from both RICH and calorimeters, gives a gain of $\sim +10\%$ on the signal acceptance
- the different definition of the fiducial decay volume, extended up to 170 meters in Z, leads to a gain of $\sim +6\%$ on the signal efficiency, that is not visible in the $A_{\pi\nu\nu}$ term, but it is absorbed in the N_K term
- the improved treatment of LAV veto and STRAW *segments* veto leads to a better ϵ^{RV} with a relative gain of $\sim +3\%$.

Since the $\sim +30\%$ improvement obtained with the 2018-OLDCOL selection is only obtained with the offline analysis, without using the 2017 data as a training sample to achieve the result, it is possible to apply the 2018-OLDCOL analysis to the 2017 data without any additional change: in this case the central value of the number of expected SM signal events in the 2017 sample would be ~ 3 instead of 2.16 with the same (or better) signal over background ratio.

Chapter 5

The backgrounds estimation

The estimation of the background contamination in the signal selection is a crucial part of the analysis, since to claim the observation of the $K^+ \to \pi^+\nu\bar{\nu}$ ultra-rare process (and then measure its branching ratio), the number of observed events must not be compatible with a model in which only the backgrounds sources are included. A good balance between the achieved SES and a low background contamination, with an accurate knowledge of it, is fundamental to increase the experimental sensitivity.

The backgrounds are estimated exploiting a data-driven approach, defining kinematic background and control regions, as described in the dedicated section (e.g. Figure 3.18). For the $K^+ \to \pi^+\pi^+\pi^-$ decay, even if background and control regions are defined, the estimation also relays on Monte Carlo simulation. The $K^+ \to \pi^+\pi^-e^+\nu$ estimation it is purely based on Monte Carlo simulation. For the background coming from $K^+ \to \pi^+\pi^-e^+\nu$ and *upstream* events, is not possible to define kinematic control and background regions, since their kinematic distributions are spread over the signal regions: in those case validation samples are defined (instead of control regions) to cross-check the estimations; the validation samples are obtained inverting at least one of the signal selection criteria. Background coming from other processes are checked and considered negligible with respect to the ones mentioned above.

5.1 $K^+ \to \pi^+\pi^0$ background

The $K^+ \to \pi^+\pi^0$ background is estimated assuming that the kinematic rejection is independent from the rest of the selection, then the number of expected background events is obtained factorizing the rejection powers as follows:

$$N^{exp}_{\pi^+\pi^0}(region)_j = N_{\pi^+\pi^0}(bkg)_j \cdot f^{kin}_{\pi^+\pi^0}(region)_j \tag{5.1}$$

where:

- $N^{exp}_{\pi^+\pi^0}(region)$ is the number of expected background events in the region *region*, to be determined;
- $N_{\pi^+\pi^0}(bkg)$ is the number of events inside the $K^+ \to \pi^+\pi^0$ background region after the signal selection (Figure 3.19);
- $f^{kin}_{\pi^+\pi^0}(region)$ is the kinematic factor that represents which is the fraction of the tails of the background distribution inside the considered *region*;
- j is the index of the bin in which the full π^+ momentum range is split (5 GeV/c size);
- *region* is any region defined in Table 3.1.

The kinematic factor $f^{kin}_{\pi^+\pi^0}$ is measured selecting a $K^+ \to \pi^+\pi^0$ control sample on CTRL data. This selection is orthogonal to the signal selection, in fact one of the selection criteria is inverted: in the $K^+ \to \pi^+\pi^0$ case, two photons coming from the $\pi^0 \to \gamma\gamma$ decay are tagged, while in the signal selection the presence of one photon is enough to reject the event. In order to reproduce the kinematic distribution of the events that pass the signal selection, the control sample must not be biased by the new cuts introduced.

The m^2_{miss} distribution of the selected $K^+ \to \pi^+\pi^0$ control sample is shown in Figure 5.1 integrated over the full momentum range 15-45 GeV/c, since the $K^+ \to \pi^+\pi^0$ distribution is flat on momentum (Figure 3.2).

The kinematic factor $f^{kin}_{\pi^+\pi^0}(region)$ is then determined on this distribution dividing the number of events in the considered *region* by the number of events in the corresponding background region (i.e. around the nominal squared π^0 mass).

The computation of the kinematic factor is performed for the two signal regions and the control regions CR1 and CR2.

An extra scaling factor is applied to the kinematic factor in R2, in order to properly take into account the contribution given by the radiative correction, i.e. the $K^+ \to \pi^+\pi^0\gamma$ decay, that is not included in the $K^+ \to \pi^+\pi^0$ control sample, since those events are rejected by the control sample selection. This factor is estimated in the analysis for the $\pi^0 \to$ *invisible* search [71] and it is +13% relative, with 100% relative systematic uncertainty conservatively applied.

The contribution of the $K^+ \to \pi^+\pi^0$ events when the π^+ decays in flight is negligible due to the gain on the rejection given by the PID criteria.

5.2 $K^+ \to \mu^+\nu$ background

The estimation of the $K^+ \to \mu^+\nu$ background follows an approach similar to the $K^+ \to \pi^+\pi^0$ background estimation. The only difference is related to the fact

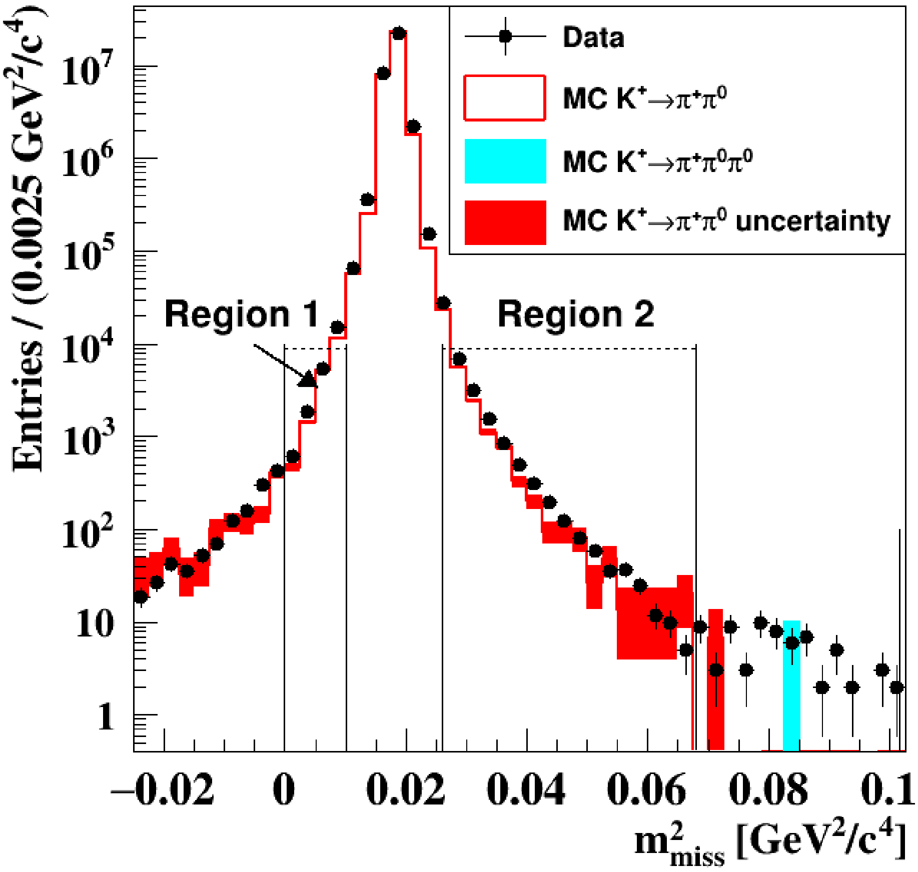

Figure 5.1: Distribution of m^2_{miss} of the $K^+ \to \pi^+\pi^0$ control sample, integrated over the full 15-45 GeV/c π^+ momentum range. The expected distribution from the Monte Carlo simulation is also shown, even if not used for the background estimation. Figure from [36].

that in the $K^+ \to \mu^+\nu$ rejection a crucial role is played by the RICH PID, that is not uncorrelated with the kinematic rejection, therefore the factorization applied in Equation 5.1 is not completely allowed. The correlation between RICH PID and kinematics comes from the reconstruction of the Cherenkov ring in the RICH detector, that relays on the momentum measurement by the STRAW spectrometer, and from the m^2_{miss} -3d definition of the signal regions, where the RICH detector is involved.

In order to proper take into account those correlations and to avoid an over-estimation of the rejection power of the global selection, the estimation of the

$K^+ \to \mu^+\nu$ background is performed using the following relation, slightly different with respect to Equation 5.1:

$$N^{exp}_{\mu^+\nu}(region)_j = N^{NO-RICH}_{\mu^+\nu}(bkg)_j \cdot f^{kin+RICH}_{\mu^+\nu}(region)_j \quad (5.2)$$

where:

- $N^{exp}_{\mu^+\nu}(region)$ is the number of expected background events in the region *region*, to be determined;
- $N^{NO-RICH}_{\mu^+\nu}(bkg)$ is the number of events inside the $K^+ \to \mu^+\nu$ background region after the signal selection, without the application of the RICH criteria;
- $f^{kin+RICH}_{\mu^+\nu}(region)$ is the factor that represents the *RICH and kinematics* rejection, which is the fraction of events in the tails of the background distribution inside the considered *region*, that pass the RICH PID criteria;
- j is the index of the bin in which the full π^+ momentum range is split (5 GeV/c size)
- *region* is any region defined in Table 3.1.

The factor $f^{kin+RICH}_{\mu^+\nu}(region)$ is determined selecting a $K^+ \to \mu^+\nu$ control sample on CTRL data, inverting the Calorimetric PID criteria with respect to the signal selection, i.e. the charged particle is identified as a muon in LKr, MUV1, MUV2, MUV3 detectors.

The m^2_{miss} distribution of the $K^+ \to \mu^+\nu$ control sample is shown in Figure 5.2, split in bins of momentum, since the peak of the $K^+ \to \mu^+\nu$ m^2_{miss} distribution is closer to the signal regions at high momenta, as observed in Figure 3.2. This is the reason why R1 has not been extended up to 45 GeV/c momentum. The drop of the $K^+ \to \mu^+\nu$ m^2_{miss} distribution at the boundary of signal regions is due to the RICH PID requirements, not applied in the background region.

As for the $K^+ \to \pi^+\pi^0$ background, the kinematic factor $f^{kin+RICH}_{\mu^+\nu}(region)$ is determined dividing the number of events in the considered *region* by the number of events in the corresponding background region.

The computation of the kinematic factor is performed for the two signal regions and the control regions CRμ, CRμ2, CRμ3.

An additional correction to the $K^+ \to \mu^+\nu$ background estimation must be taken into account due to the possibility that the muon decays in flight via the $\mu^+ \to e^+\nu\nu$ process. In this case the rejection power of the $K^+ \to \pi^+\nu\bar{\nu}$ selection must be evaluated separately, since several conditions are affected by the $\mu^+ \to e^+\nu\nu$ decay: kinematic rejection, RICH PID, CALO PID (including MUV3 usage). The relative differences with respect to the standard $K^+ \to \mu^+\nu$ decay are computed depending on the position where the $\mu^+ \to e^+\nu\nu$ decay happens (in particular as a function

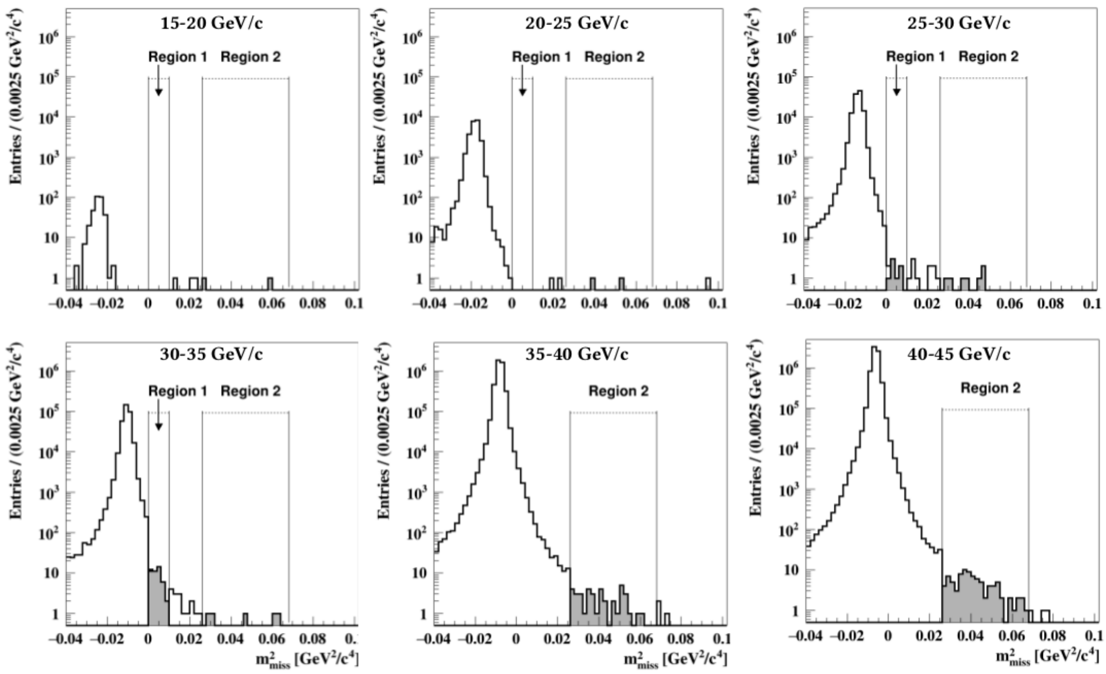

Figure 5.2: Distribution of m^2_{miss} of the $K^+ \to \mu^+\nu$ control sample, with π^+ momentum range split in bins of 5 GeV/c size. Figure from [36].

of the Z coordinate of the decay point $Z_{\mu\to e}$), using MC simulation, measuring the ratio between the single rejection powers for the $\mu^+ \to e^+\nu\nu$ process and the standard $K^+ \to \mu^+\nu$ decay, as follows:

$$N_{\mu\to e}(region) = N_{K_{\mu 2}}(region) \cdot \sum_j [f_j^{\mu\to e}(region)] \tag{5.3}$$

$$f_j^{\mu\to e}(region) = \frac{\epsilon_j^{RICH}(\mu \to e) \cdot \epsilon_j^{CALO}(\mu \to e) \cdot \epsilon_j^{region}(\mu \to e) \cdot P_j(\mu \to e)}{\epsilon^{RICH}(K_{\mu 2}) \cdot \epsilon^{CALO}(K_{\mu 2}) \cdot \epsilon^{region}(K_{\mu 2})} \tag{5.4}$$

where the efficiencies of the single parts of the $K^+ \to \pi^+\nu\bar{\nu}$ selection are indicated with ϵ, j is the index of the 10 m size bins in which the $Z_{\mu\to e}$ range of interest (i.e. 110-220 m) is divided, $P_j(\mu \to e)$ is the probability that a muon, coming from a $K^+ \to \mu^+\nu$ process, decays in $\mu^+ \to e^+\nu\nu$ in each bin. The variables $Z_{\mu\to e}$ and $P_j(\mu \to e)$ are obtained looking at the true values generated in the Monte Carlo simulation, while the ϵ values are obtained applying the different $K^+ \to \pi^+\nu\bar{\nu}$ selection criteria in the simulated samples. The ratio in Equation 5.4 leads to the cancellation of possible uncertainties due to the not perfect data/simulation agreement.

Only the $Z_{\mu\to e}$ range 110-220 m is analyzed because $Z_{vtz} > 110$ m is required by the *trapezoidal* cut, while if the decay happens at $Z > 220$ m, i.e. downstream of the STRAW spectrometer, it does not affect the measurement of the kinematic tails in the standard $K^+ \to \mu^+\nu$ background estimation, in fact those events are already counted in the standard $K^+ \to \mu^+\nu$ estimation.

The different $K^+ \to \pi^+\nu\bar{\nu}$ selection criteria behave differently as a function of $Z_{\mu\to e}$. The m^2_{miss} variable, for instance, is more spread in the signal regions at low $Z_{\mu\to e}$, while it is closer to the $K^+ \to \mu^+\nu$ background region at high $Z_{\mu\to e}$. On the other hand the RICH PID works better at low $Z_{\mu\to e}$, while at high $Z_{\mu\to e}$ (when the muon decays between the third and the fourth STRAW stations) most of its rejection power is lost, since one of the two methods of the RICH ring reconstruction relies on the track direction measured by the STRAW.

The results of the measurements of $f_j^{\mu\to e}(region)$ for CRμ and R1 are shown in Figure 5.3: only the last two bins give a not negligible contribution, i.e. when the $\mu^+ \to e^+\nu\nu$ decay happens between the STRAW dipole magnet and the fourth STRAW chamber. In this case all the selection criteria involved (kinematic, RICH PID, Calorimeters PID) loose rejection power because the track is badly reconstructed after the dipole magnet due to the decay. If the decay occurs before the dipole magnet, the kinematic selection looses even more rejection power, but RICH and calorimetric PID are not affected too much, therefore the global rejection power is strong enough.

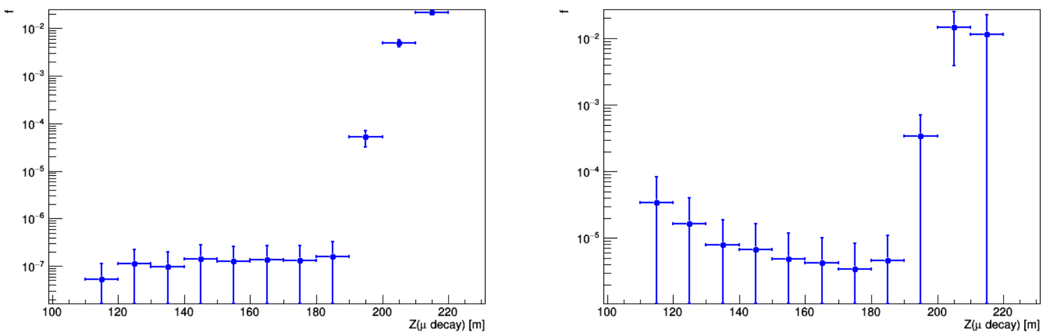

Figure 5.3: Measurements of $f_j^{\mu\to e}(region)$ for CRμ (Left) and R1 (Right).

Integrating over the full $Z_{\mu\to e}$ range, according to Equation 5.3, the following results are obtained:

$$\frac{N_{\mu\to e}(CR\mu)}{N_{K_{\mu 2}}(CR\mu)} = 0.03 \pm 0.01 \; ; \; \frac{N_{\mu\to e}(R1)}{N_{K_{\mu 2}}(R1)} = 0.03 \pm 0.03 \tag{5.5}$$

while the contribution of the $\mu^+ \to e^+\nu\nu$ process to the background in R2 is negligible.

This correction factor of 3% relative is then applied with the corresponding uncertainties to the $K^+ \to \mu^+\nu$ background estimation in R1 and in CRμ. The uncertainties are mostly due to the statistics of the simulation.

5.3 $K^+ \to \pi^+\pi^+\pi^-$ background

The $K^+ \to \pi^+\pi^+\pi^-$ process is a three-body decay, which m^2_{miss} distribution is not peaked to a single value, but it is spread in a wide kinematic region (Figure 3.2). In order to apply an approach similar to the $K^+ \to \pi^+\pi^0$ background estimation, the events contained in the $K^+ \to \pi^+\pi^+\pi^-$ background region after the full signal selection (Figure 3.19) are split in bins of m^2_{miss} and for each bin a proper kinematic factor $f^{kin}_{3\pi}$ is measured.

In this case it is not possible to measure the kinematic factors $f^{kin}_{3\pi}$ on data, therefore Monte Carlo simulations are used. A basic selection requiring only the matching between a π^+ in the final state and the parent K^+ is applied to the MC $K^+ \to \pi^+\pi^+\pi^-$ sample, measuring the reconstructed m^2_{miss} value. This measurement is compared to the $m^2_{miss}(truth)$, that is the m^2_{miss} computed using the true 4-momenta of K^+ and π^+ given by the MC generator: the comparison plot is shown in Figure 5.4, where the improvement on the resolution at high m^2_{miss} values is evident.

This allows to estimate the experimental resolution on the m^2_{miss} variable as a function of the same variable. In particular for each bin of $m^2_{miss}(truth)$ in the $K^+ \to \pi^+\pi^+\pi^-$ region, the distribution of the reconstructed m^2_{miss} is considered (Figure 5.5), and the kinematic rejection factors $f^{kin}_{3\pi}$ are determined as the ratio between the number of events in the tails (i.e. signal and control regions) and the number of events inside a range equal to the considered $m^2_{miss}(truth)$ bin.

An iterative procedure is then used to take into account that a fraction of events in each m^2_{miss} bin is due to the tails of the distributions of the other bins.

These m^2_{miss}-dependent $f^{kin}_{3\pi}$ factors are then multiplied by the number of events in the corresponding m^2_{miss} bin of the $K^+ \to \pi^+\pi^+\pi^-$ background region in data after the complete signal selection has been performed (Figure 3.19). The $K^+ \to \pi^+\pi^+\pi^-$ background estimation is obtained after integrating the background estimates in each m^2_{miss} bin.

5.4 $K^+ \to \pi^+\pi^-e^+\nu$ background

For the $K^+ \to \pi^+\pi^-e^+\nu$ background it is not possible to define background and control kinematic regions, since for this decay the m^2_{miss} distribution is spread over the R2, as shown in Figure 2.2. The number of expected background events in the signal regions is estimated using Monte Carlo simulation, with the same procedure

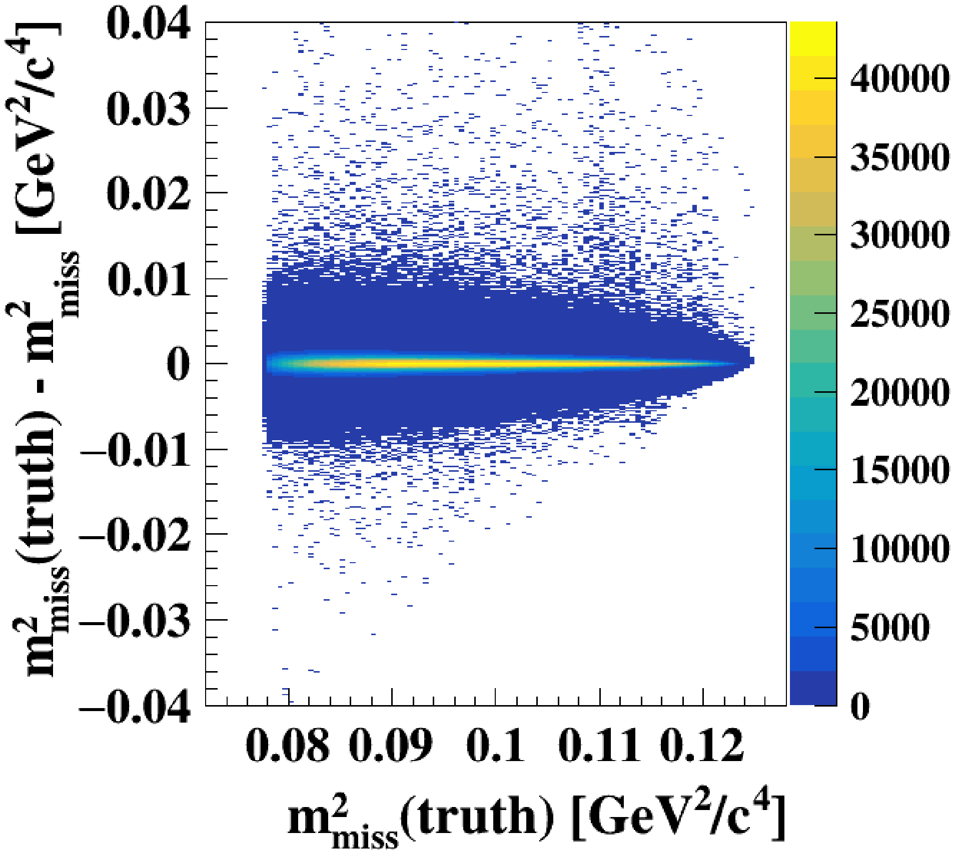

Figure 5.4: Distribution of the difference between true and reconstructed m^2_{miss} versus the true m^2_{miss} in the $K^+ \to \pi^+\pi^+\pi^-$ Monte Carlo sample.

adopted to determined the number of expected SM signal events (Equation 4.2 and Equation 4.3). Since the rejection power of the signal selection is very high, a large amount of Monte Carlo events has been simulated (more than $2.2 \cdot 10^9$ events), in order to measure the acceptance with an acceptable statistical uncertainty.

The absence of control regions to validate the estimation requires the definition of *validation samples*, where the statistics is enough to compare expectation (from MC) and observation (on data). The validation samples are selected inverting at least one of the criteria of the signal selection, in order to enrich the sample with $K^+ \to \pi^+\pi^-e^+\nu$ events. In particular four validation samples are defined as follows:

- Sample 1: signal selection, with inverted multiplicity conditions in the STRAW.

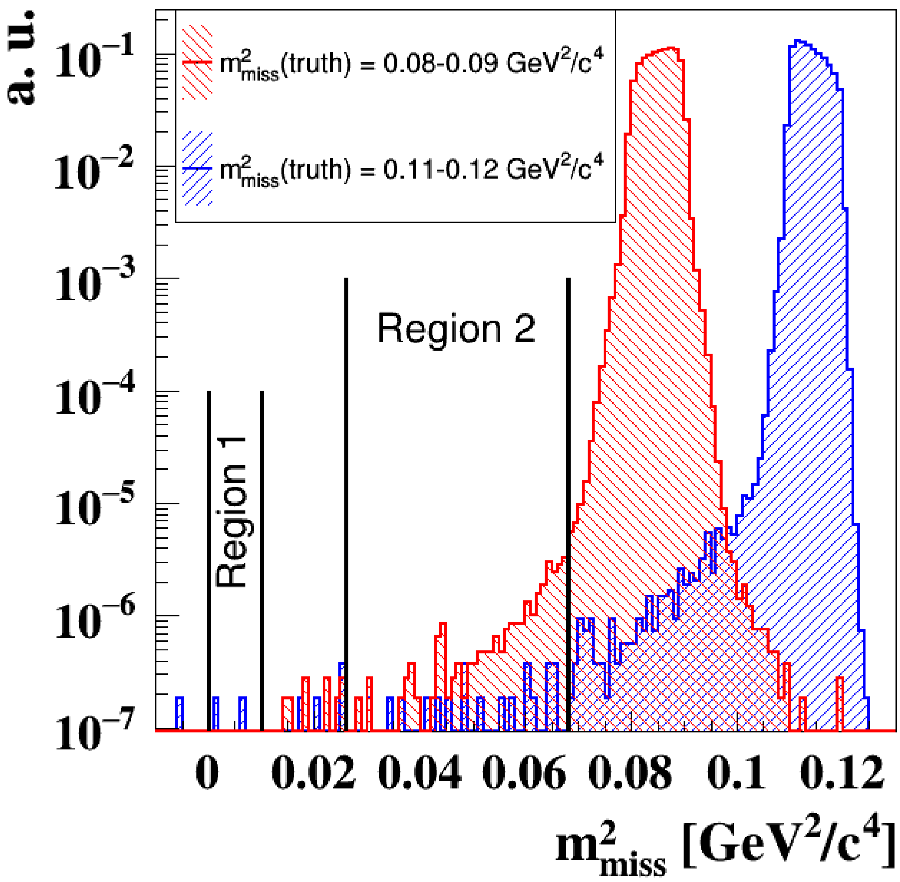

Figure 5.5: Tails of the m^2_{miss} distribution for different bins of $m^2_{miss}(truth)$, obtained in the $K^+ \to \pi^+\pi^+\pi^-$ Monte Carlo sample. Both distributions are normalized to 1. Figure from [36].

- Sample 2: signal selection applied to the π^-, RICH identification criteria not used, inverted multiplicity conditions in the STRAW.
- Sample 3: same as sample 2, but the standard STRAW multiplicity conditions are used.
- Sample 4: same as sample 3, but the RICH identification criteria are used.

The comparison between data and Monte Carlo of the reconstructed m^2_{miss} in the validation sample 2 (Figure 5.6) shows a good agreement within the statistical uncertainty.

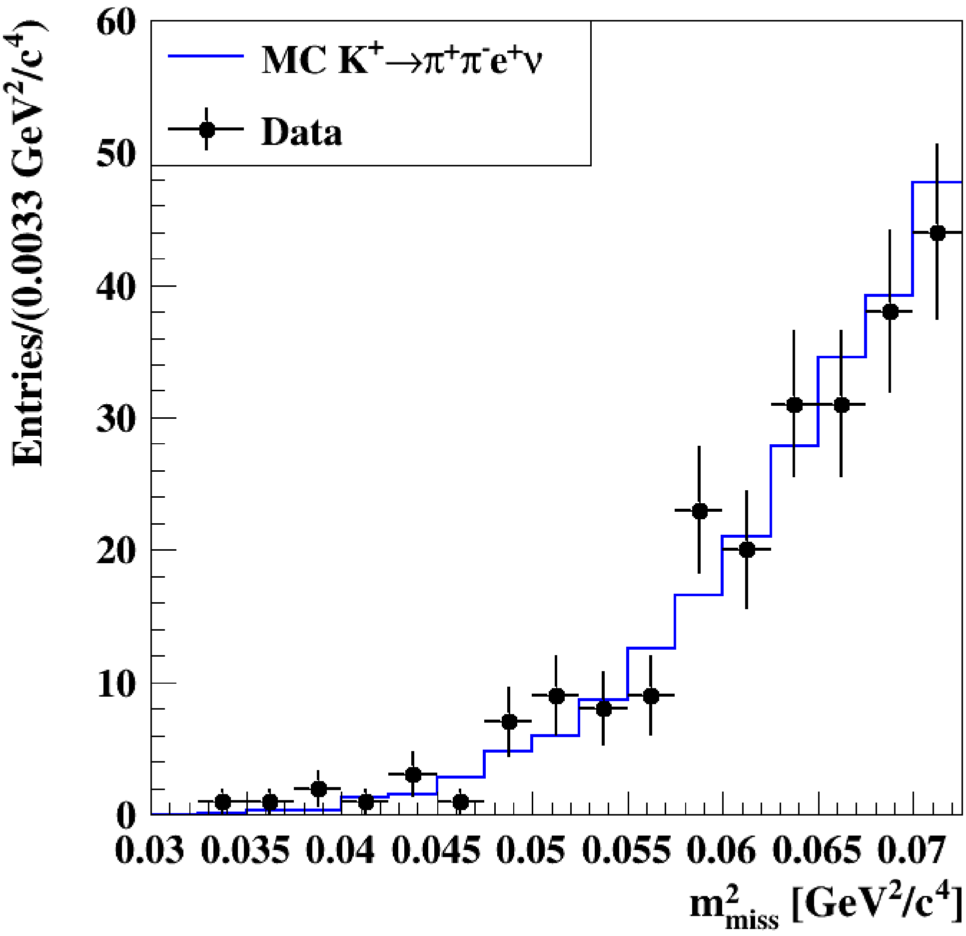

Figure 5.6: Distribution of m^2_{miss} in $K^+ \to \pi^+\pi^-e^+\nu$ validation sample 2, for data and Monte Carlo simulation. Figure from [36].

All the four $K^+ \to \pi^+\pi^-e^+\nu$ validation samples are used to compare the number of expected events from the Monte Carlo simulation to the observed events in data (Figure 5.7); a global p-value is computed to quantify the statistical agreement: p-value = 0.76. The selection criteria of the validation samples are defined so that rejection powers that differ by up to two orders of magnitude can be tested, as shown in Figure 5.7.

5.5 Upstream background

The background arising from the *upstream* events is the most important contribution to the background of the $K^+ \to \pi^+\nu\bar{\nu}$ search. The main features of this category

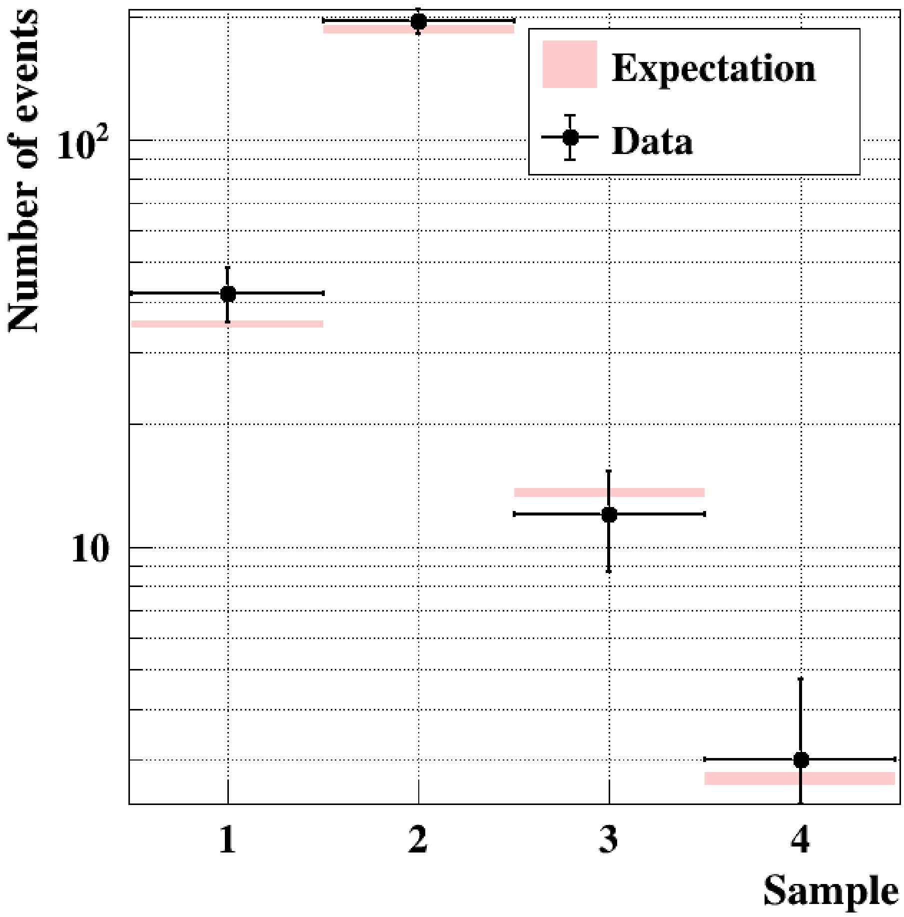

Figure 5.7: Expected events from the Monte Carlo simulation and observed events in data, for the four $K^+ \to \pi^+\pi^-e^+\nu$ validation samples: the global p-value that quantifies the agreement is 0.76. Figure from [36].

of events have been described in Section 3.7, together with the selection criteria defined for their rejection.

A detailed description of the method used for the *upstream* background estimation in the 2017 analysis, similar to the one used in the present analysis, is provided in [94].

The estimation of this background contribution consists in two parts: counting the number of *upstream* events in the $K^+ \to \pi^+\nu\bar{\nu}$ selection before the application of the $K^+ - \pi^+$ matching algorithm, ($N^{events}_{upstream}$), and then measuring the probability (P_{mistag}) that those events are mistagged as a good signal candidate by the $K^+ - \pi^+$ matching algorithm. Both the quantities are measured as a function the $|\Delta t|$

between the detectors involved in the matching (KTAG, GTK, RICH), splitting the 0.0-0.5 ns $|\Delta t|$ window in 10 bins of 0.05 ns size. The two quantities are then combined according to Equation 5.6 in order to measure the number of expected *upstream* background in the final $K^+ \to \pi^+\nu\bar{\nu}$ selection ($N^{bkg}_{upstream}$).

$$N^{bkg}_{upstream} = \sum_j P_{mistag}(|\Delta t_j|) \cdot N^{events}_{upstream}(|\Delta t_j|) \tag{5.6}$$

In order to measure $N^{events}_{upstream}$, an enriched sample of *upstream* events is selected without applying the $K^+ - \pi^+$ matching algorithm and inverting the signal selection condition $CDA < 4$ mm. The number of events in the enriched sample is denoted as $N^{enriched}_{upstream}$.

The CDA distribution of the *upstream* events in the enriched sample is shown in Figure 5.8, where the first bin (0-4 mm) is missing due to the inverted CDA condition. The distribution is modeled with a Monte Carlo simulation in order to cross-check the agreement with data and to find out the number of expected events in the first bin. The number of events in the enriched sample ($N^{enriched}_{upstream}$), scaled by the factor (f^{CDA}_{scale}) that takes into account the first bin missing (obtained by the MC model), represents the measurement of $N^{events}_{upstream}$:

$$N^{events}_{upstream}(|\Delta t_j|) = f^{CDA}_{scale} \cdot N^{enriched}_{upstream}(|\Delta t_j|) \tag{5.7}$$

Once the model of the CDA distribution has been obtained, P_{mistag} is determined applying the $K^+ - \pi^+$ matching algorithm to the enriched sample, assuming that the time distribution of the events that pass the $K^+ \to \pi^+\nu\bar{\nu}$ selection (i.e. $CDA < 4$ mm) is the same as for the events in the enriched sample (i.e. $CDA \geq 4$ mm). The results are reported in Figure 5.9, separating OLDCOL and NEWCOL selections, since the different selection criteria slightly affect them.

In order to increase the statistics for the measurement of f^{CDA}_{scale} and P_{mistag}, some cuts that do not affect the behaviour of the *upstream* events are removed from the selection of the enriched sample: e.g. the cut on GTK extra hits, that in this case produces only random veto. Moreover, for the OLDCOL selection, the 2017 data are also used, since the data taking conditions are the same. These changes are not applied for the measurement of $N^{enriched}_{upstream}$.

Since the *upstream* background is widespread all over the signal regions, validation samples are defined in order to cross-check the estimations, with the same logic adopted for the $K^+ \to \pi^+\pi^-e^+\nu$ background. Given that differences between OLDCOL and NEWCOL selections, also the definition of the validation samples differs for the two selections, as described below.

Definition of *upstream* validation samples for the OLDCOL selection:

- Sample 1: signal selection, inverted *box cut*: $|X_{Coll}| < 100$ mm, $|Y_{Coll}| < 140$ mm

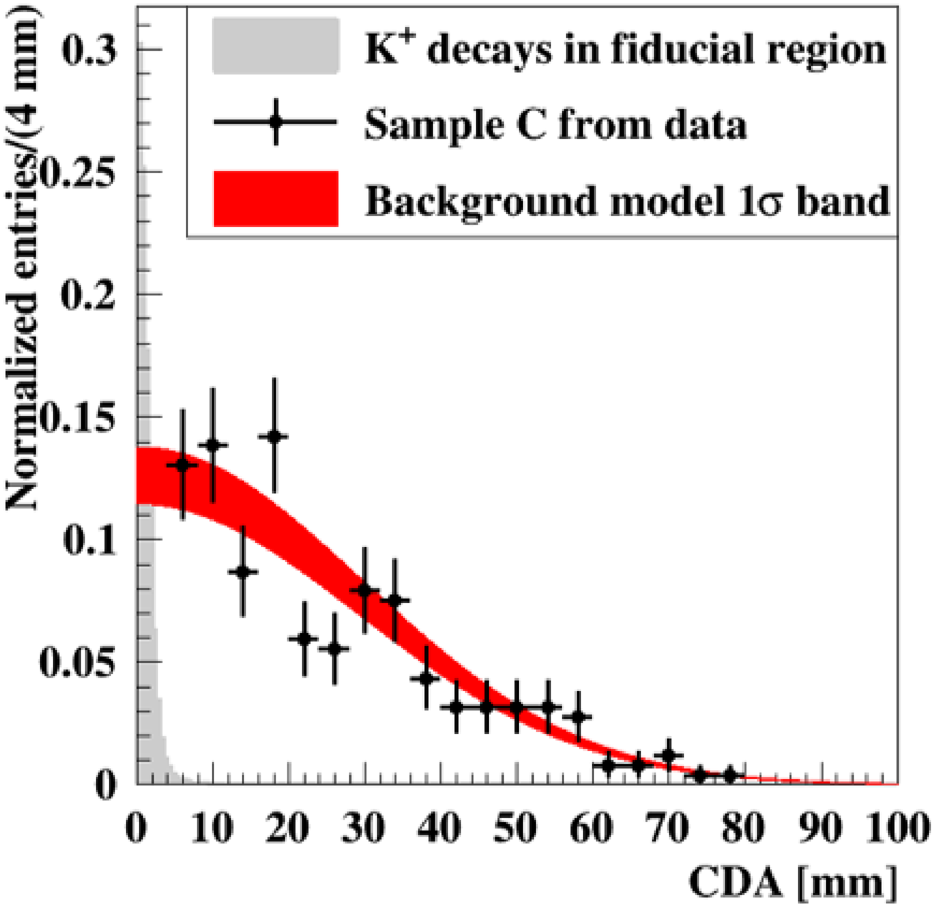

Figure 5.8: Distribution of *CDA* variable in the enriched sample of *upstream* events. The red Gaussian curve represents the model for those data obtained with Monte Carlo simulation.

- Sample 2: same as sample 1, $m^2_{miss} < -0.05\ GeV^2/c^4$
- Sample 3: the signal selection, inverted *box cut*: $|X_{Coll}| < 100$ mm, $|Y_{Coll}| \in [140, 500]$ mm
- Sample 4: same as sample 3, $m^2_{miss} < -0.05\ GeV^2/c^4$
- Sample 5: the signal selection, different kinematic region: $m^2_{miss} < -0.05\ GeV^2/c^4$.

Definition of *upstream* validation samples for the NEWCOL selection:

- Sample 1: signal selection, inverted cut on BDT discriminant (Figure 3.8)

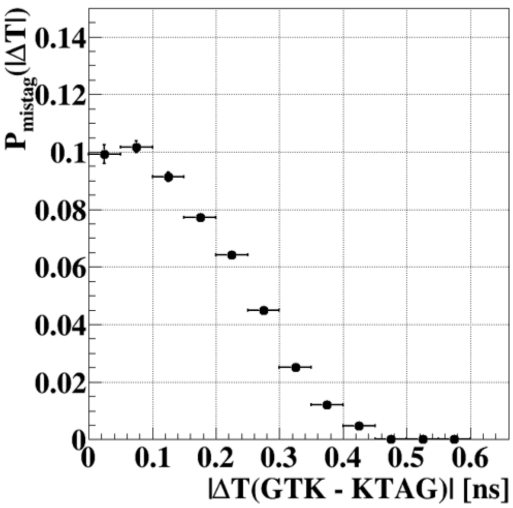

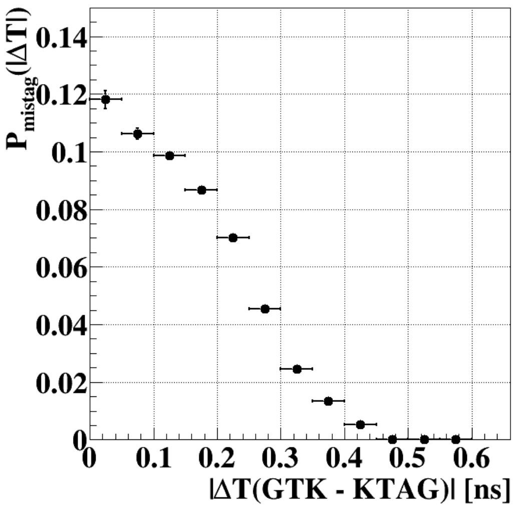

Figure 5.9: Results of P_{mistag} measurements in bins of $|\Delta t(GTK - KTAG)|$ (0.05 ns size) for the OLDCOL selection (Left) and the NEWCOL selection (Right). The uncertainties represented in the plots are only statistical.

- Sample 2: same as sample 1, $m^2_{miss} < -0.05\ GeV^2/c^4$
- Sample 3: signal selection, different kinematic region: $m^2_{miss} < -0.05\ GeV^2/c^4$.

All the *upstream* validation samples are used to compare the number of expected and observed events (Figure 5.10); p-values are also computed to quantify the statistical agreement: p-value(OLDCOL) = 0.58, p-value(NEWCOL) = 0.64, demonstrating the validity of both the cut-based approach (OLDCOL selection) and the BDT approach (NEWCOL selection) against the *upstream* background.

The definition of the validation samples allows to test rejection powers that differ by up to two orders of magnitude, as shown in Figure 5.10.

5.6 Backgrounds estimation results

The summary of the expected background integrated over the full π^+ momentum range and over the full 2018 data sample, is reported in Table 5.1, together with the expected SM signal events for comparison (B/S ratio kept at ~ 0.7, constant with respect to the 2017 analysis [34]). Other sources of background, e.g. $K^+ \to \pi^0 l^+ \nu$ or $K^+ \to \pi^+ \gamma\gamma$, have been considered and measured to be negligible with respect to the ones quoted.

The *upstream* background is the main source of background in the 2018 analysis, since represents the $\sim 60\%$ of the total. The main contribution from kaon decays

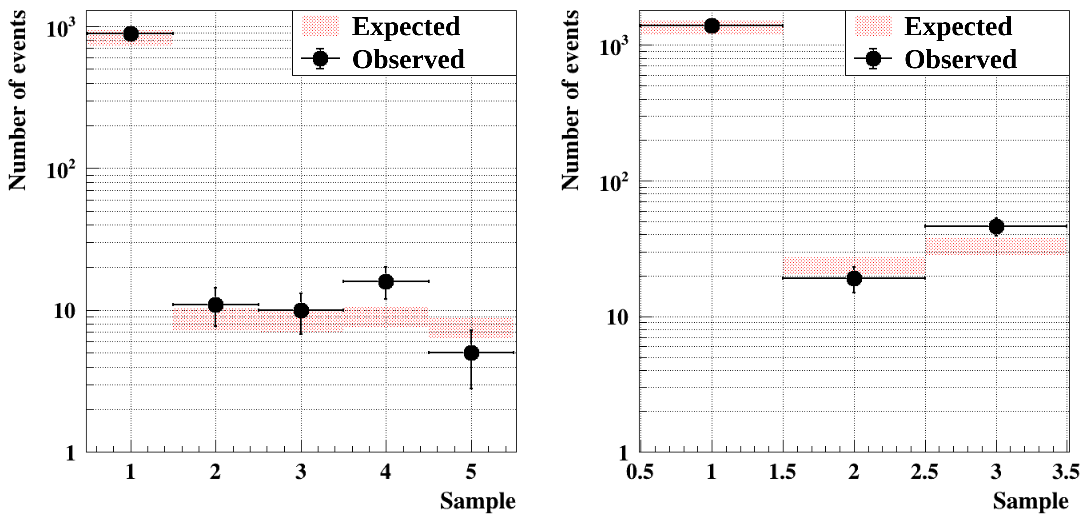

Figure 5.10: Expected and observed events in the *upstream* validation samples for OLDCOL selection (Left) and NEWCOL selection (Right). The p-values that quantify the agreement are: p-value(OLDCOL) = 0.58, p-value(NEWCOL) = 0.64. Figures from [36].

Process	Expected events in Signal Regions
$K^+ \to \pi^+\nu\bar{\nu}$	$7.58 \pm 0.40_{syst} \pm 0.75_{ext}$
$K^+ \to \pi^+\pi^0$	0.75 ± 0.04
$K^+ \to \mu^+\nu$	0.49 ± 0.05
$K^+ \to \pi^+\pi^+\pi^-$	0.24 ± 0.08
$K^+ \to \pi^+\pi^-e^+\nu$	0.50 ± 0.11
Upstream	$3.30^{+0.98}_{-0.73}$
Total background	$5.28^{+0.99}_{-0.74}$

Table 5.1: Number of expected events in Signal Regions in the full 2018 data sample.

is given by the $K^+ \to \pi^+\pi^0$ channel, smaller by more than a factor 4 with respect to the *upstream* background.

Comparing to the 2017 analysis, the main difference in relative terms is given by the increasing of the $K^+ \to \pi^+\pi^+\pi^-$ contribution. This is due to the changes of the *trapezoidal cut* introduced to improve the signal efficiency, nevertheless the background contribution due to the $K^+ \to \pi^+\pi^+\pi^-$ decays is still less than 5% of the total.

The uncertainties assigned to the background contributions are related to the statistical limitation of the samples (data and Monte Carlo) used for the estimations and to the systematic errors introduced by the estimation methods. In particular, the uncertainty on the total background is dominated by the uncertainty of the *upstream* background, that is at the level of $\sim 30\%$ relative. Such uncertainty is due to:

- the statistical limitation of $N^{enriched}_{upstream}$ (9 events in the OLDCOL selection, 38 in the NEWCOL selection), that leads to a Poissonian asymmetric uncertainty of $\sim 15\%$ relative,

- the limited accuracy of the *upstream* events model (Figure 5.8), that affects the measurements of f^{CDA}_{scale} and P_{mistag} with a global uncertainty of $\sim 25\%$ relative.

The background estimations are also reported separately for the 2018-OLDCOL sample (Table 5.2) and in bins of π^+ momentum for the 2018-NEWCOL sample (Table 5.3), to be consistent with the statistical treatment used for the $Br(K^+ \to \pi^+\nu\bar{\nu})$ measurement, that is described in the next chapter. The statistics of 2018-OLDCOL sample is too small to be split in bins of π^+ momentum.

Background	Events in R1+R2
$\pi^+\pi^0$	0.23 ± 0.02
$\mu^+\nu$	0.12 ± 0.02
$\pi^+\pi^+\pi^-$	0.05 ± 0.02
$\pi^+\pi^-e^+\nu$	0.09 ± 0.03
Upstream	$0.54^{+0.39}_{-0.21}$

Table 5.2: Expected number of background events in signal regions, for the 2018-OLDCOL sample, integrated over the full π^+ momentum range.

5.7 Results from the Control Regions

The Control regions are used to validate the background estimations, as defined in Figure 3.18. The expected events in control regions are measured with the same strategy as for the expected events in signal regions. The composition of expected events in the control regions is the following:

Background	15 − 20	20 − 25	25 − 30	30 − 35	35 − 40	40 − 45
$\pi^+\pi^0$	0.180 ± 0.020	0.136 ± 0.016	0.095 ± 0.012	0.050 ± 0.008	0.019 ± 0.004	0.037 ± 0.005
$\mu^+\nu$	0.020 ± 0.011	0.016 ± 0.009	0.050 ± 0.016	0.162 ± 0.031	0.050 ± 0.010	0.070 ± 0.011
$\pi^+\pi^+\pi^-$	0.060 ± 0.029	0.082 ± 0.034	0.031 ± 0.013	0.010 ± 0.006	0.002 ± 0.002	0
$\pi^+\pi^-e^+\nu$	0	0.063 ± 0.045	0.061 ± 0.043	0.116 ± 0.058	0.118 ± 0.059	0.052 ± 0.037
Upstream	$0.84^{+0.78}_{-0.29}$	$0.73^{+0.67}_{-0.27}$	$0.13^{+0.32}_{-0.08}$	$0.73^{+0.52}_{-0.29}$	$0.13^{+0.31}_{-0.08}$	$0.20^{+0.41}_{-0.11}$

Table 5.3: Expected number of background events in signal regions, for the 2018-NEWCOL sample, split in bins of π^+ momentum (5 GeV/c size).

- CRμ and CRμ3: $K^+ \to \mu^+\nu$ decays
- CRμ2: $K^+ \to \mu^+\nu$ decays and *upstream* events
- CR1 and CR2: $K^+ \to \pi^+\pi^0$ and $K^+ \to \pi^+\nu\bar{\nu}$ decays
- CR3: $K^+ \to \pi^+\pi^+\pi^-$, $K^+ \to \pi^+\pi^-e^+\nu$, $K^+ \to \pi^+\nu\bar{\nu}$ decays and *upstream* events
- CR-3d: $K^+ \to \mu^+\nu$, $K^+ \to \pi^+\pi^0$, $K^+ \to \pi^+\nu\bar{\nu}$ decays.

The numbers of expected events in the control regions are reported in Table 5.4 (OLDCOL sample) and in Table 5.5 (NEWCOL sample).

Region	15 − 20	20 − 25	25 − 30	30 − 35	35 − 40	40 − 45	$\pi^+\nu\bar{\nu}$
CR1	0.40 ± 0.07	0.52 ± 0.09	0.37 ± 0.08	0.29 ± 0.08	0.29 ± 0.07	0.24 ± 0.06	~ 0.3
CR2	0.67 ± 0.12	0.84 ± 0.13	0.56 ± 0.12	0.41 ± 0.10	0.39 ± 0.09	0.29 ± 0.08	~ 0.2
CRμ	< 0.01	0.58 ± 0.08	1.90 ± 0.20	4.40 ± 0.50	17.0 ± 2.0	18.0 ± 2.0	~ 0
CRμ3	–	–	–	–	6.4 ± 1.0		< 0.1
CRμ2	1.90 ± 0.20						~ 0
CR3	0.20 ± 0.08						< 0.1
CR-3d	0.40 ± 0.14						~ 0.2

Table 5.4: Expected number of events in control regions, from 2018-OLDCOL sample. Events in CRμ2, CR3 and CR-3d are integrated over the full π^+ momentum range. Events in CRμ3 are integrated in the (35-45) GeV/c π^+ momentum range. The last column displays the approximated number of signal events expected in the control regions, integrated in the full π^+ momentum range.

The events observed after opening the control regions are reported in Table 5.6 (OLDCOL sample) and in Table 5.7 (NEWCOL sample), together with the p-values obtained comparing to the expectations of Table 5.4 and Table 5.5. The p-values are computed according to Equation 40.16 of [43], generating 10^8 pseudo-experiments

Region	15 − 20	20 − 25	25 − 30	30 − 35	35 − 40	40 − 45	$\pi^+\nu\bar{\nu}$
CR1	1.30 ± 0.14	1.04 ± 0.20	0.87 ± 0.23	0.62 ± 0.21	0.44 ± 0.16	0.83 ± 0.16	~ 0.9
CR2	2.25 ± 0.23	1.71 ± 0.25	1.33 ± 0.25	0.84 ± 0.21	0.56 ± 0.16	1.02 ± 0.17	~ 0.8
CRμ	0.05 ± 0.02	2.30 ± 0.30	7.10 ± 0.70	16.0 ± 2.0	65.0 ± 7.0	80.0 ± 8.0	~ 0
CRμ3	−	−	−	−	26.0 ± 3.0		~ 0.3
CRμ2	7.40 ± 0.60						~ 0
CR3	1.19 ± 0.39						~ 0.3
CR-3d	1.52 ± 0.55						~ 0.6

Table 5.5: Expected number of events in control regions, from 2018-NEWCOL sample. Events in CRμ2, CR3 and CR-3d are integrated in the full π^+ momentum range. Events in CRμ3 are integrated in the (35-45) GeV/c π^+ momentum range. The last column displays the approximated number of signal events expected in the control regions, integrated in the full π^+ momentum range.

Region	15 − 20	20 − 25	25 − 30	30 − 35	35 − 40	40 − 45	p-value
CR1	0	0	0	1	0	1	0.29
CR2	0	0	0	1	1	0	0.43
CRμ	0	2	2	8	14	11	0.21
CRμ3	−	−	−	−	6		1.00
CRμ2	2						1.00
CR3	0						1.00
CR-3d	2						0.07

Table 5.6: Observed number of events in control regions, from 2018-OLDCOL sample. Events in CRμ2, CR3 and CR-3d are integrated over the full π^+ momentum range. Events in CRμ3 are integrated over the (35-45) GeV/c π^+ momentum range. The last column displays the global p-value in each region.

with a toy-Monte-Carlo technique. All the p-values show the absence of significant statistical disagreements in any region (the worst p-value is 0.07).

The plot in Figure 5.11 shows the opened control regions in the full 2018 data sample. Observed and expected events in each control region (integrated over the full momentum range and adding OLDCOL and NEWCOL samples) are also reported.

The results of the control regions CR1, CR2, CRμ in the full 2018 data sample (OLDCOL+NEWCOL samples) are reported in Figure 5.12, where expectations and observations are graphically compared in each π^+ momentum bin. The corresponding p-values, computed with the same procedure as in Table 5.6 and Table 5.7 are: p-value(CR1) = 0.36, p-value(CR2) = 0.11, p-value(CRμ) = 0.07.

The events observed in control region CR-3d are represented in Figure 5.13 and

Region	15 − 20	20 − 25	25 − 30	30 − 35	35 − 40	40 − 45	p-value
CR1	2	1	0	2	2	1	0.42
CR2	1	2	0	1	2	0	0.34
CRμ	0	2	11	12	40	72	0.07
CRμ3	−	−	−	−	25		0.87
CRμ2	9						0.59
CR3	0						0.37
CR-3d	3						0.46

Table 5.7: Observed number of events in control regions, from 2018-NEWCOL sample. Events in CRμ2, CR3 and CR-3d are integrated over the full π^+ momentum range. Events in CRμ3 are integrated in the (35-45) GeV/c π^+ momentum range. The last column displays the global p-value in each region.

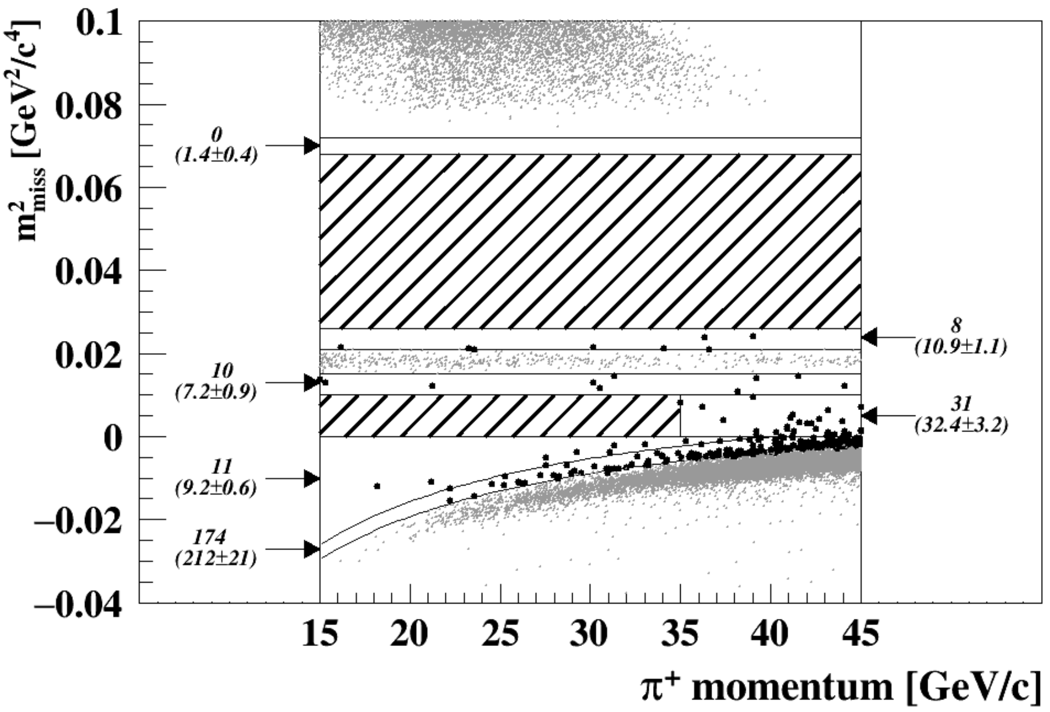

Figure 5.11: Opened control regions in the full 2018 data sample, with the numbers of observed and expected (in parenthesis) events in each control region (integrated over the full momentum range and adding OLDCOL and NEWCOL samples). Figure from [36].

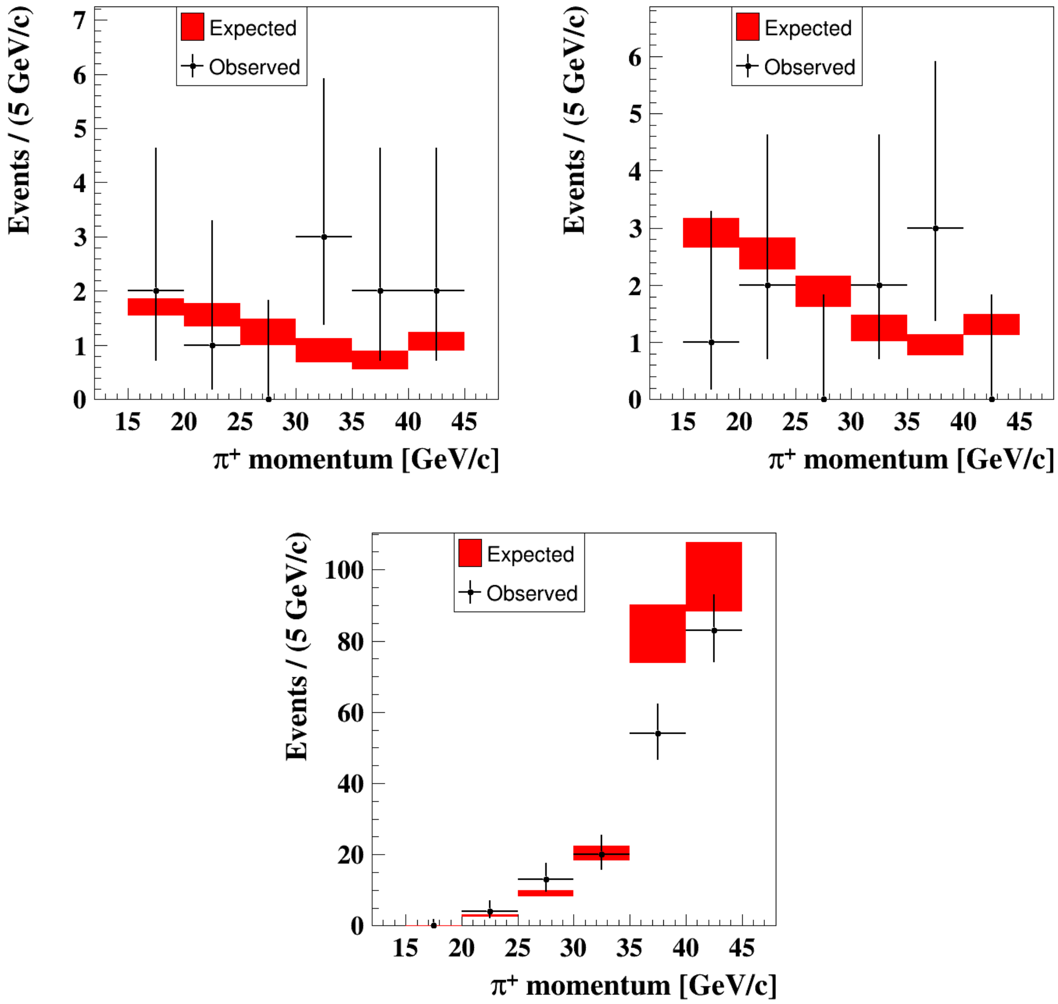

Figure 5.12: Comparison of expectations and observations for CR1 (Top-Left), CR2 (Top-Right), CRμ (Bottom) in the full 2018 data sample (OLD-COL+NEWCOL samples), split in bins of π^+ momentum. The corresponding p-values are: p-value(CR1) = 0.36, p-value(CR2) = 0.11, p-value(CRμ) = 0.07. Figures from [36].

5.14, since that region, by definition, is not included in the standard kinematic plot m^2_{miss} vs π^+ momentum. Since the contamination of this region comes from $K^+ \to \mu^+\nu$ and $K^+ \to \pi^+\pi^0$ decays, the observed events are displayed in comparison to the distributions of those decays, obtained from the $K^+ \to \mu^+\nu$ and $K^+ \to \pi^+\pi^0$ control samples.

Once the estimation and the validation of the background are completed, the

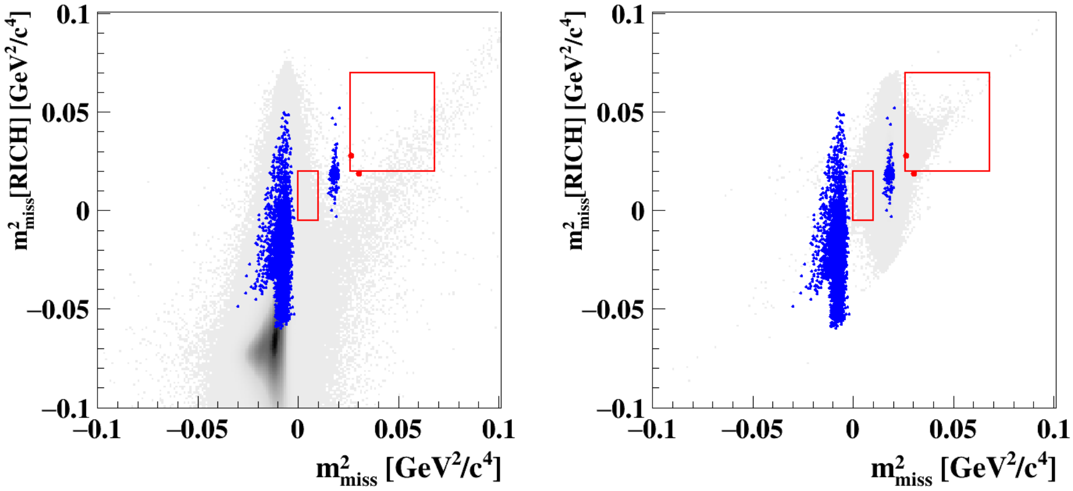

Figure 5.13: Events in the $m^2_{miss}[RICH]$ vs m^2_{miss} plane, from the 2018-OLDCOL sample, after the $K^+ \to \pi^+\nu\bar{\nu}$ selection. The red boxes represent the two signal regions. The red dots are the observed events in the CR-3d region. The blue dots are the observed events in the $K^+ \to \mu^+\nu$ and $K^+ \to \pi^+\pi^0$ background regions. The grey dots in the left (right) plot are the $K^+ \to \mu^+\nu$ ($K^+ \to \pi^+\pi^0$) control sample. The observed event displayed inside R2 is actually part of the CR-3d region because of the constraint on $m^2_{miss}[beam]$, not visible in the plots.

2018 data sample after the $K^+ \to \pi^+\nu\bar{\nu}$ selection is shown in Figure 5.15, with only the signal regions still blinded, ready to be opened to finalize the $Br(K^+ \to \pi^+\nu\bar{\nu})$ measurement, as described in the next chapter.

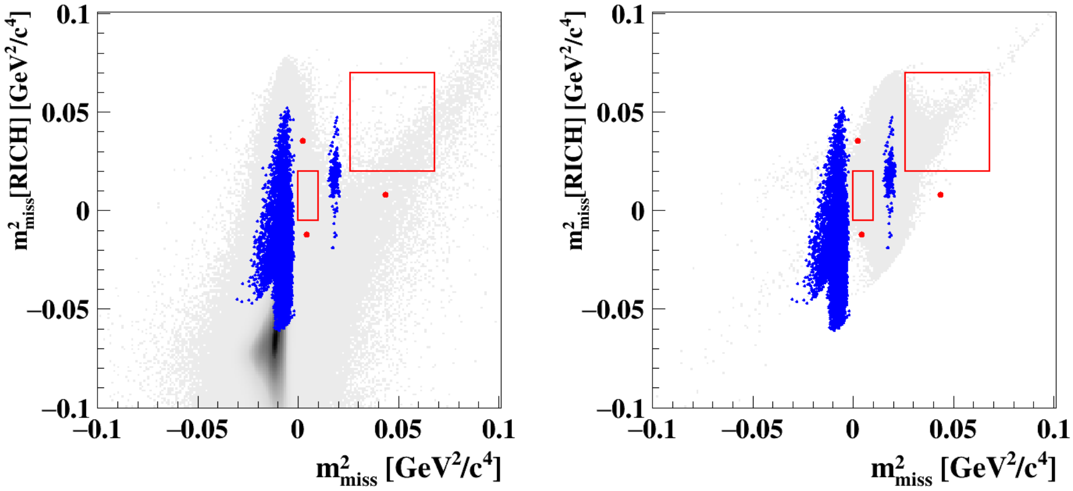

Figure 5.14: Events in the $m^2_{miss}[RICH]$ vs m^2_{miss} plane, from the 2018-NEWCOL sample, after the $K^+ \to \pi^+ \nu \bar{\nu}$ selection. The red boxes represent the two signal regions. The red dots are the observed events in the CR-3d region. The blue dots are the observed events in the $K^+ \to \mu^+ \nu$ and $K^+ \to \pi^+ \pi^0$ background regions. The grey dots in the left (right) plot are the $K^+ \to \mu^+ \nu$ ($K^+ \to \pi^+ \pi^0$) control sample.

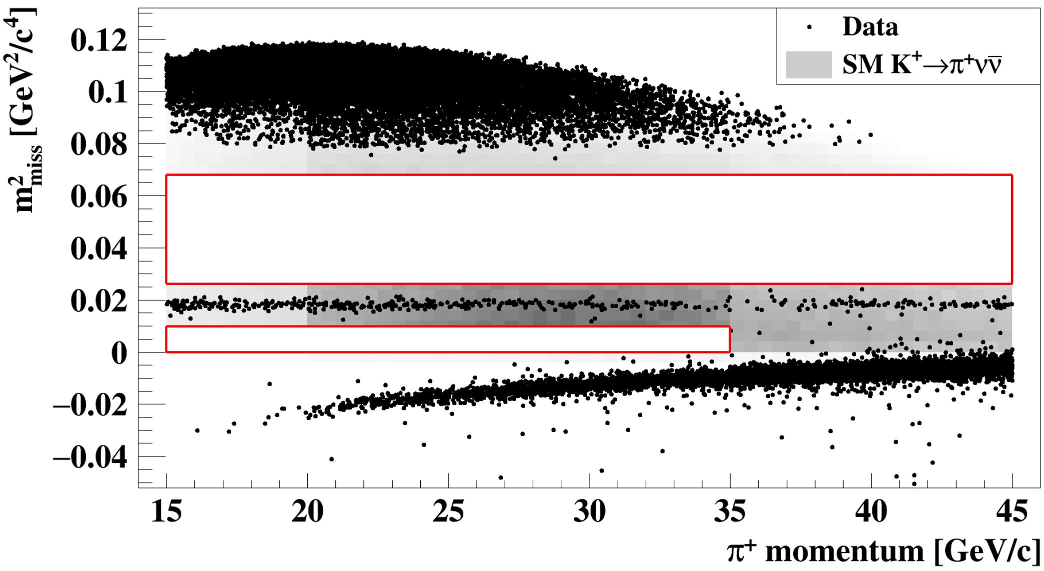

Figure 5.15: Events from the full 2018 data sample that pass the full $K^+ \to \pi^+ \nu\bar{\nu}$ selection in the (p_{π^+}, m^2_{miss}) plane, with signal regions blinded. The grey area represents the $K^+ \to \pi^+ \nu\bar{\nu}$ acceptance from the Monte Carlo simulation. Figure from [36].

Chapter 6

The measurement of $Br(K^+ \to \pi^+\nu\bar{\nu})$

After the estimations of signal and background are completed and validated, the signal regions can be unblinded to reveal the number of observed $K^+ \to \pi^+\nu\bar{\nu}$ candidates and, eventually, to compute $Br(K^+ \to \pi^+\nu\bar{\nu})$.

6.1 Events in signal regions

The full 2018 data sample after the $K^+ \to \pi^+\nu\bar{\nu}$ selection is represented in Figure 6.1, together with the signal regions opened: 17 events are observed, 4 in R1 and 13 in R2; 2 events in R2 are from the 2018-OLDCOL sample, all the others are from the 2018-NEWCOL one. A small excess of events is observed with respect to the Standard Model prediction (7.58 signal events and 5.28 background events). The observed number of events agrees with the theoretical SM prediction within 1 standard deviation.

The same events can be seen in the m^2_{miss} projection, in comparison to the expected SM signal and background (Figure 6.2 and Figure 6.3). Figure 6.3 is useful to appreciate the different background contribution originating from each source in each π^+ momentum bin.

A statistical reinterpretation of this analysis, looking for possible resonance peaks in the m^2_{miss} distribution of Figure 6.2, can be performed to search for production of an invisible exotic particle X in the process $K^+ \to \pi^+X$, as already done by NA62 in the 2017 data sample [95].

The numbers of observed events in the signal regions are also reported in Table 6.1, for the 2018-OLDCOL sample (integrated over the full π^+ momentum) and for the 2018-NEWCOL sample (split in bins of π^+ momentum), since that is how they are then used in the statistical treatment for the $Br(K^+ \to \pi^+\nu\bar{\nu})$ measurement.

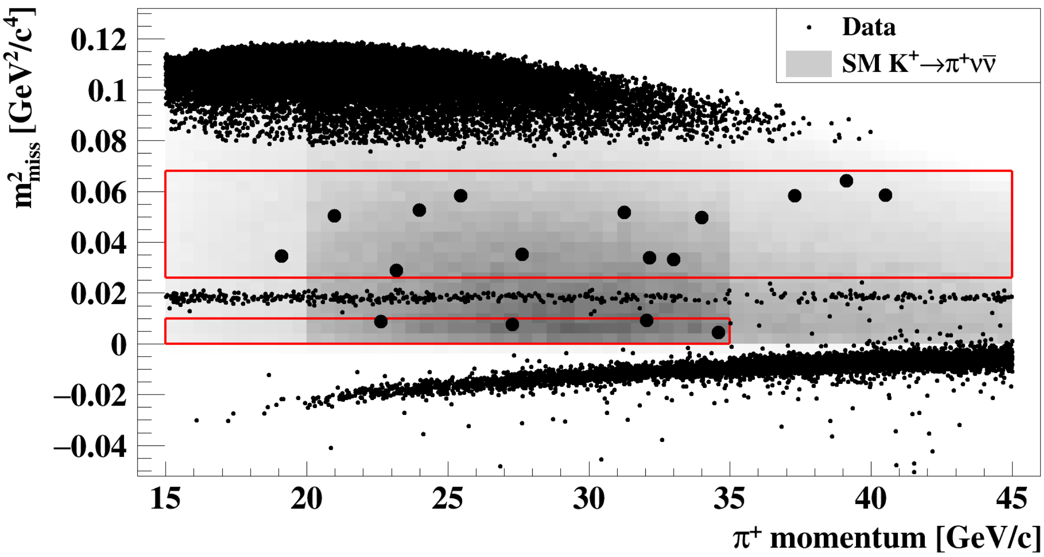

Figure 6.1: Events from the full 2018 data sample that pass the full $K^+ \to \pi^+\nu\bar{\nu}$ selection in the (p_{π^+}, m^2_{miss}) plane, with the signal regions opened. 17 events are observed in the signal regions, 4 in R1 and 13 in R2. The grey area represents the $K^+ \to \pi^+\nu\bar{\nu}$ acceptance from the Monte Carlo simulation. Figure from [36].

	15 – 20	20 – 25	25 – 30	30 – 35	35 – 40	40 – 45
OLDCOL sample	2 (all bins)					
NEWCOL sample	1	4	2	6	1	1

Table 6.1: Observed events in signal regions, from 2018-OLDCOL, integrated over the full π^+ momentum, and from 2018-NEWCOL, split in π^+ momentum bins.

6.2 Statistical interpretation

In order to statistically interpret the observed events and to compute $Br(K^+ \to \pi^+\nu\bar{\nu})$, the following procedure has been adopted. The procedure itself has been defined before the unblinding of the signal regions.

The 2018-NEWCOL sample is split in six categories, that correspond to the six momentum bins of 5 GeV/c size in which the π^+ momentum range is divided. In each category the $K^+ \to \pi^+\nu\bar{\nu}$ SES corresponds to $O(1)$ Standard Model expected signal events. The 2016, 2017 and 2018-OLDCOL samples, where the poor SES would not allow further splitting, have been treated as three separate categories. It is important to underline that the 2016 and 2017 data have not been reanalyzed:

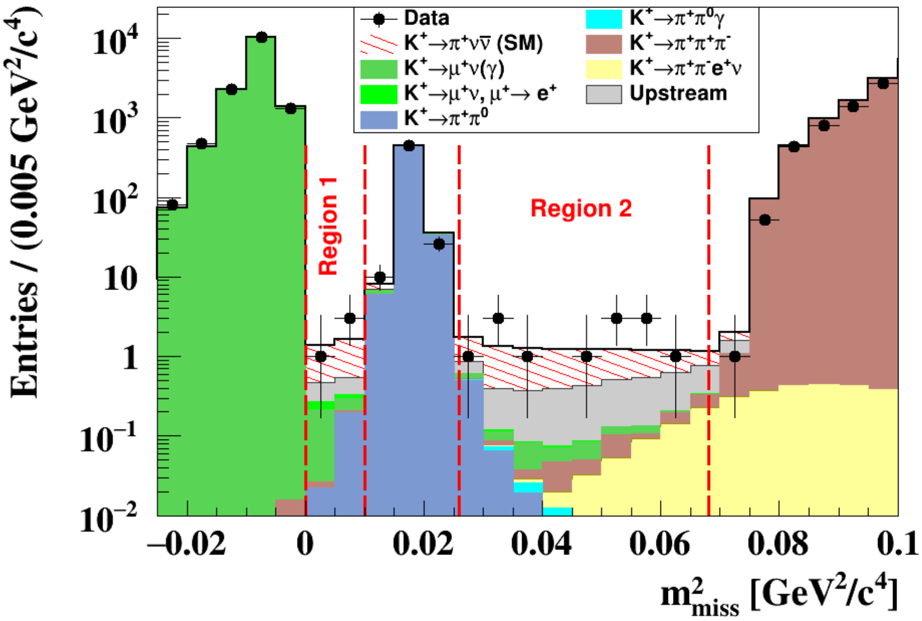

Figure 6.2: Distribution of m^2_{miss} of the events from the full 2018 data sample that satisfy the $K^+ \to \pi^+\nu\bar{\nu}$ selection. Data (points) are shown together with expected SM signal and background (histograms). The expectations are displayed without uncertainty. The distribution is integrated over the full π^+ momentum range. Figure from [36].

the results of the analyses published in [33] (2016) and in [34] (2017) are used. Those results are reported for completeness in Table 6.2.

Data sample	expected signal	expected background	observed events
2016	$0.267 \pm 0.020 \pm 0.032_{ext}$	0.15 ± 0.09	1
2017	$2.16 \pm 0.13 \pm 0.26_{ext}$	1.46 ± 0.30	2

Table 6.2: Expected and observed events in the 2016 [33] and 2017 [34] data samples.

The expected and observed number of events in each category is displayed in Figure 6.4.

A maximum likelihood fit is performed over all the categories according to Equation 40.16 of [43], where the signal strength μ, defined in Equation 6.1, is a

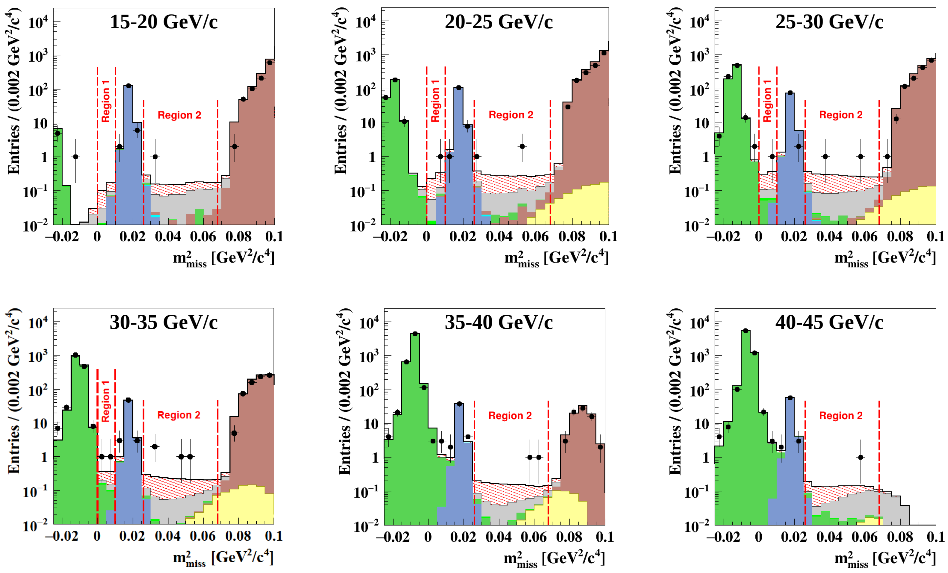

Figure 6.3: Distribution of m^2_{miss} of the events from the full 2018 data sample that satisfy the $K^+ \to \pi^+\nu\bar{\nu}$ selection. Data (points) are shown together with expected SM signal and background (histograms). The expectations are displayed without uncertainty. The distribution is shown splitting the π^+ momentum range in six bins of 5 GeV/c size. The legend is the same as for Figure 6.2. Figures from [36].

free parameter of the fit.

$$\mu = \frac{Br^{measured}(K^+ \to \pi^+\nu\bar{\nu})}{Br^{SM}(K^+ \to \pi^+\nu\bar{\nu})} \tag{6.1}$$

In the fit procedure the number of expected Standard Model signal events is used without the external uncertainty due to the theoretical prediction.

In an ideal situation (i.e. without uncertainties), in each category the number of expected events should be related to the observed events and to the signal strength μ by the following condition:

$$N^{obs} = \mu \cdot S^{exp} + B^{exp} \tag{6.2}$$

Once the signal strength is extracted from the fit, the result for $Br(K^+ \to \pi^+\nu\bar{\nu})$ is obtained inverting Equation 6.1, using only the central value, without uncertainty, for $Br^{SM}(K^+ \to \pi^+\nu\bar{\nu})$.

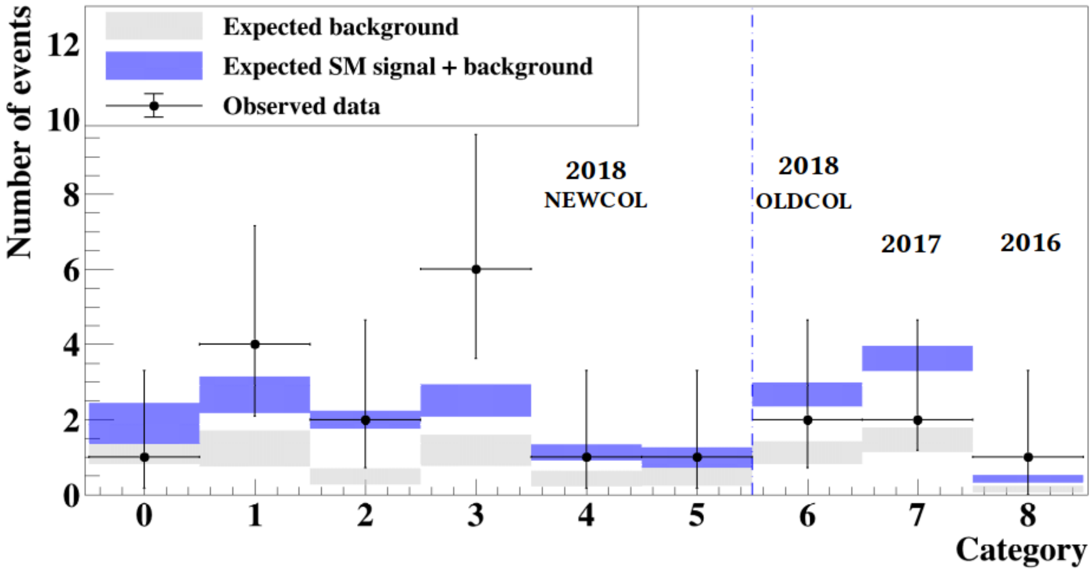

Figure 6.4: Expected and observed number of events in each category. See the text for the categories definition. Figure from [36].

6.3 Preliminary result of $Br(K^+ \to \pi^+\nu\bar{\nu})$ measurement from 2016-2018 NA62 data

The result of the statistical procedure just described, that represents the preliminary result of the $Br(K^+ \to \pi^+\nu\bar{\nu})$ measurement performed by the NA62 experiment with data collected between 2016 and 2018, is:

$$Br^{NA62-16-17-18}(K^+ \to \pi^+\nu\bar{\nu}) = (1.10^{+0.40}_{-0.35\ stat} \pm 0.03_{syst}) \cdot 10^{-10} \tag{6.3}$$

The central value is above the Standard Model prediction (Equation 1.17), but completely in agreement within less than 1 standard deviation. The uncertainty is at the level of $\sim 35\%$ relative and it is dominated by the statistical contribution, mostly due to the limited number of observed events. It represents the most precise measurement ever performed for this physics quantity, as shown in Figure 6.5.

In terms of experimental significance, the result corresponds to 3.5σ, integrated over the 9 categories of Figure 6.4, therefore it is the first evidence for the observation of the $K^+ \to \pi^+\nu\bar{\nu}$ ultra-rare process. It means that the probability that a model without the $K^+ \to \pi^+\nu\bar{\nu}$ process (i.e. only background) would yield the same observation is: $P(only\ bkg) \simeq 2 \cdot 10^{-4}$.

The new preliminary result from NA62 can be compared to several New Physics models that predict significant deviations of $Br(K^+ \to \pi^+\nu\bar{\nu})$ with respect to the Standard Model prediction, for example those illustrated in Figure 1.7 and

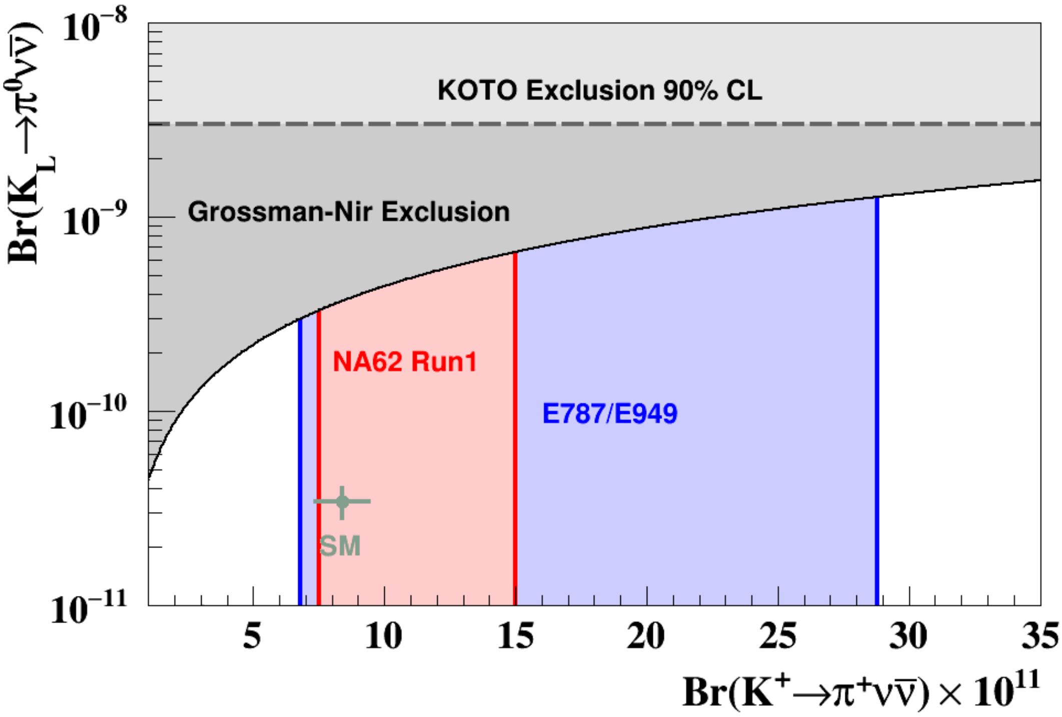

Figure 6.5: Status of $Br(K \to \pi\nu\bar{\nu})$ measurements. The grey cross represents the Standard Model prediction (Equation 1.17 and Equation 1.19). The blue band shows the $Br(K^+ \to \pi^+\nu\bar{\nu})$ measurements from BNL E787 and E949 experiments (Equation 1.21), while the red band is the new preliminary result from NA62 (Equation 6.3). The Grossman-Nir limit (Equation 1.20) can be combined with the NA62 preliminary result to obtain a tighter upper limit for $Br(K_L \to \pi^0\nu\bar{\nu})$ with respect to the KOTO upper limit at 90% CL (Equation 1.24). Figure from [36].

1.9: large discrepancies with respect to the Standard Model expectation tend to be excluded, as shown in Figure 6.6. The search for possible New Physics in $K^+ \to \pi^+\nu\bar{\nu}$ requires a more precise measurement, therefore more statistics is needed.

6.4 Prospects for $Br(K^+ \to \pi^+\nu\bar{\nu})$ measurement

Even if the new $Br(K^+ \to \pi^+\nu\bar{\nu})$ measurement is the most precise ever performed, it is still not enough to reveal possible New Physics effects. The actual precision is limited by statistics, that is affected by two main factors: the data taking duration and conditions and the signal efficiency obtained in the offline analysis.

NA62 will resume data taking in 2021, after CERN *Long Shutdown 2* (LS2),

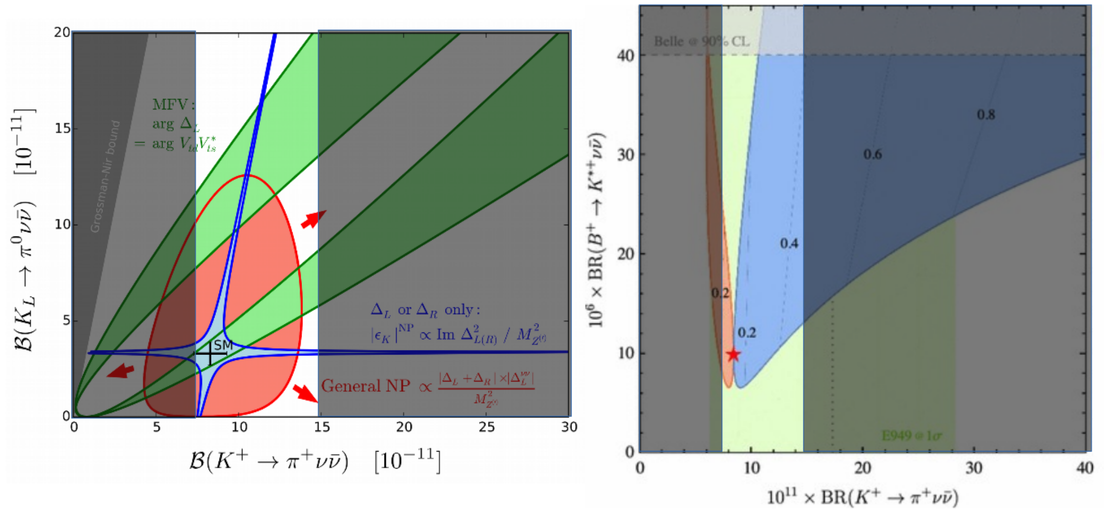

Figure 6.6: New Physics scenarios represented in Figure 1.7 (Left) and in Figure 1.9 (Right), with the shadowed areas excluded by the new preliminary result from NA62 (1σ uncertainty). Figures from [36].

and proposed to take data in the full period before CERN LS3 [81]. This would correspond to a data taking period roughly three times longer than 2018. Moreover, this run should be taken at 100% nominal beam intensity (on average), instead of 60-70% as it was during the 2018 run. Test runs at the end of the 2018 data taking indicates that full intensity can be accomplished.

Concerning the signal efficiency of the offline analysis, its main limitation is due to the background contamination: despite the sizeable improvements achieved in the 2018 analysis presented in this thesis, it will not be possible to increase the signal efficiency with an affordable increase of the background. Therefore the background must be reduced improving the detector setup: this will possibly allow for signal efficiency improvements.

The following actions are ongoing [80] and will be concluded before resuming data taking, to strongly suppress the main source of background, the *upstream* events:

- beam line re-arranging to sweep away *upstream* π^+, that should not be able to enter the fiducial decay region anymore (the re-arranging is possible using the existing beam line elements);
- adding a fourth GigaTracker station (GTK-4), to reduce the probability of matching the *upstream* π^+ track with an in time pileup beam particle that mimics the parent kaon;
- adding a new veto-counter system just before the final collimator, in order to

detect the other products of *upstream* decays now lost.

These modifications of the detector layout would bring to a strong suppression of the *upstream* background, that should become smaller than the background coming from the standard kaon decays.

An additional off-axis calorimeter (HASC-2) will also be installed, to further suppress background arising from $K^+ \to \pi^+\pi^0$ decays, the second largest background source after the *upstream* events.

The higher beam intensity, the run-time requested and the outlined detector improvements could allow NA62 to be able to reach a final statistical precision of the order of 10%.

This figure can be estimated and understood as follows.

The $\simeq 6$ expected Standard Model signal events obtained in 2018-NEWCOL can be multiplied by the factors:

- 10/7, since 2018-NEWCOL sample is only 70% of the full 2018 sample;
- 3, since three years of equivalent 2018 data taking are foreseen;
- 100/65, since the beam intensity will increase from 60-70% to 100% of the nominal;
- 1.3, that represents the foreseen +30% in the offline signal efficiency.

This would lead to a total of $\simeq 50$ expected Standard Model events in the future data taking. Adding the $\simeq 10$ expected Standard Model events already obtained in the 2016-2018 data sample, brings the total number of expected Standard Model events to $\simeq 60$.

The relative uncertainty of the $Br(K^+ \to \pi^+\nu\bar{\nu})$ measurement can be conservatively expressed as a function of the number of signal events and the signal over background ratio, as follows [81]:

$$\frac{\delta Br}{Br} \simeq \frac{1}{\sqrt{S}} \cdot \sqrt{1 + 2 \cdot (B/S)} \tag{6.4}$$

Inserting $S = 60$ and $B/S = 0.2$ (due to the background suppression given by the detector improvements) in Equation 6.4, yields an estimate of the relative uncertainty for the $Br(K^+ \to \pi^+\nu\bar{\nu})$ measurement of about 15%.

6.5 Conclusions

The analysis of the 2018 data sample collected by the NA62 experiment leads to significant improvements in terms of experimental sensitivity, thanks to a sizeable increase in signal efficiency for the $Br(K^+ \to \pi^+ \nu\bar{\nu})$ measurement. This has been possible thanks to the detector upgrade in June 2018 consisting in the installation of a final collimator that suppresses one of the main background sources and thanks to several other improvements of the offline data analysis, that represent the main task of my PhD activity.

After more than 30 years of dedicated searches for the $K^+ \to \pi^+ \nu\bar{\nu}$ decay, the NA62 experiment, with the analysis of the data collected in the 2016-2018 period, achieved the best experimental precision ever reached in the measurement of $Br(K^+ \to \pi^+ \nu\bar{\nu})$ (35% relative), and a significance of 3.5σ, i.e. the first evidence for the observation of the ultra-rare process $K^+ \to \pi^+ \nu\bar{\nu}$.

The measurement is compatible with the Standard Model expectation within less than 1 standard deviation. Therefore it is not enough to claim that possible New Physics effects could affect the branching ratio of this golden channel in the Flavor Physics sector. On the other hand this measurement can already be used to exclude some New Physics models which foresee Br values with a large discrepancy with respect to the Standard Model prediction.

The challenge of exploring the $K^+ \to \pi^+ \nu\bar{\nu}$ golden channel is still open and promising, giving the opportunity to strictly test the Standard Model and to search for indirect evidences of New Physics effects, with a complementary approach with respect to the b-flavor sector or to the direct searches of New Physics particles.

The present experience indicates that any possible New Physics effect in this decay is not too far from the Standard Model expectation, therefore a high precision measurement is needed: that is what the NA62 experiment is planning to do with the next runs, resuming the data taking in 2021.

Appendix A

Study of the $K^+ \to \pi^0 e^+ \nu\gamma$ decay and LKr energy fine calibration

During my PhD activity, I worked also on other topics, not directly related to the $K^+ \to \pi^+ \nu\bar{\nu}$ analysis. In particular I carried out the study of the radiative semi-leptonic kaon decay $K^+ \to \pi^0 e^+ \nu\gamma$ ($Ke3\gamma$), that I started as my Master thesis project. The $K^+ \to \pi^0 e^+ \nu\gamma$ analysis, after several studies on systematic uncertainties, is now close to be finalized using the full 2017-2018 data set of NA62, as briefly described in the first section of this appendix.

The high precision needed for the $K^+ \to \pi^0 e^+ \nu\gamma$ analysis on the reconstruction of the energy of the LKr cluster produced by photons led to a dedicated study for developing a new algorithm for the LKr energy fine calibration, that is now used in the standard software of NA62: the second section of this appendix is dedicated to that.

A.1 $K^+ \to \pi^0 e^+ \nu\gamma$ decay

The main theoretical interest in the $K^+ \to \pi^0 e^+ \nu\gamma$ process is the presence of the T-odd variable ξ, defined in Equation A.1, that allows a direct measurement of possible T-violation effects, measuring the asymmetry variable A_ξ [96] [97]:

$$\xi = \frac{\overrightarrow{p_\gamma} \cdot (\overrightarrow{p_e} \times \overrightarrow{p_\pi})}{M_K^3} \; ; \; A_\xi = \frac{N_+ - N_-}{N_+ + N_-} \tag{A.1}$$

where N_+ (N_-) is the number of events with positive (negative) value of ξ.

The $K^+ \to \pi^0 e^+ \nu\gamma$ decay is described in the framework of the Standard Model *Chiral perturbation theory (ChPT)*, with two main processes: Direct Emission (DE) and Inner Bremsstrahlung (IB), shown in the diagrams of Figure A.1, and their interference (INT). The treatment of the decay at different orders of *ChPT*, with the calculation of the branching ratio, is provided in [98] (*ChPT* $O(p^4)$) and in [99] (*ChPT* $O(p^6)$). The most recent calculations of both branching ratio and T-asymmetry are provided in [100].

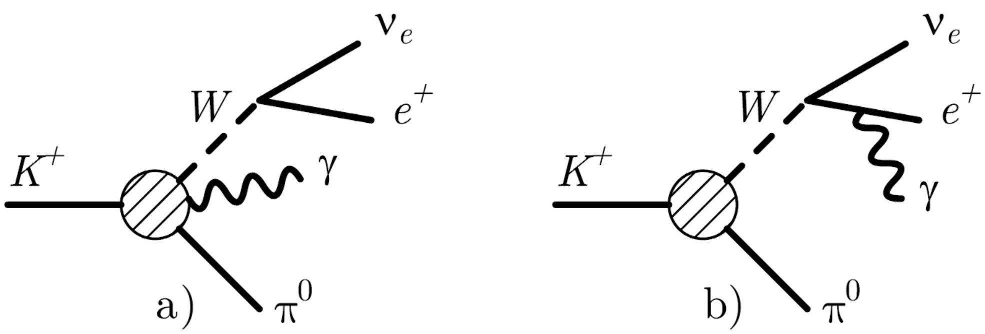

Figure A.1: Diagrams of $K^+ \to \pi^0 e^+ \nu\gamma$ decay: Direct Emission (a), Inner Bremsstrahlung (b). Figures from [99].

The two last experimental results are provided by the ISTRA+ experiment [101] (with negative charged kaons) and the OKA experiment [102] (very recent pre-print).

The $K^+ \to \pi^0 e^+ \nu\gamma$ branching ratio values (normalized to the $K^+ \to \pi^0 e^+ \nu$ channel) from the theory and from the last two experimental results are reported in Table A.1. The branching ratio strongly depends on the cut-off on the photon energy and on the angle between the photon and the positron (in the kaon rest frame), due to the divergent amplitude of the IB component.

E_γ cut	$\theta_{e,\gamma}$ cut	$O(p^6)$ *ChPT* $[10^{-2}]$	*ISTRA+* $[10^{-2}]$	*OKA* $[10^{-2}]$
$E_\gamma > 10\ MeV$	$\theta_{e,\gamma} > 10°$	1.804 ± 0.021	$1.81 \pm 0.03 \pm 0.07$	$1.990 \pm 0.017 \pm 0.021$
$E_\gamma > 30\ MeV$	$\theta_{e,\gamma} > 20°$	0.640 ± 0.008	$0.63 \pm 0.02 \pm 0.03$	$0.587 \pm 0.010 \pm 0.015$
$E_\gamma > 10\ MeV$	$0.6 < \cos\theta_{e,\gamma} < 0.9$	0.559 ± 0.006	$0.47 \pm 0.02 \pm 0.03$	$0.532 \pm 0.010 \pm 0.012$

Table A.1: Values of $Br(K^\pm \to \pi^0 e^\pm \nu\gamma)/Br(K^\pm \to \pi^0 e^\pm \nu)$, from the $O(p^6)$ *ChPT* [99] and from the measurements performed by ISTRA+ [101] and OKA [102] experiments, for different kinematic cuts. The kinematic cuts thresholds are in the kaon rest frame.

Concerning the T-symmetry violation effects, the theory predicts $|A_\xi| < 10^{-4}$ [96] [97] [100], while the best present experimental sensitivity is 2 orders of magnitude worse [101], and it refers only to the kinematic region $E_\gamma > 10\ MeV$, $0.6 < \cos\theta_{e,\gamma} < 0.9$:

$$A_\xi^{(ISTRA+)} = -0.015 \pm 0.021 \tag{A.2}$$

With the data sample collected by the NA62 experiment, there is the possibility to improve the experimental precision for both the branching ratio and the T-asymmetry measurements.

A.1.1 $K^+ \to \pi^0 e^+ \nu\gamma$ selection

The $K^+ \to \pi^0 e^+ \nu\gamma$ events are selected requiring the following conditions.

- The kaon track must be reconstructed in the GTK and the positron track must be reconstructed in the STRAW; they are then associated computing the decay vertex coordinates. The positron track is also associated with signal in the CHOD and the NewCHOD detectors, and in the RICH and LKr detectors for charged particle identification purpose (μ^+ and π^+ rejection).
- The $\pi^0 \to \gamma\gamma$ process is identified selecting two energy clusters in the LKr calorimeter, compatible with the kinematics of the π^0 decay according to the invariant mass of the photons pair.
- An extra isolated energy cluster in the LKr is associated to the radiative photon.
- In-time extra activity in LKr, LAV, IRC and SAC is not allowed, in order to reject background, mainly coming from $K^+ \to \pi^0\pi^0 e^+\nu$ decays.
- In-time signal in MUV3 is not allowed for further rejection of μ^+.
- Particular conditions are applied to reject the background coming from $K^+ \to \pi^0 e^+ \nu$ events with a photon emitted by the positron interaction with the detector material, looking to the position of the radiative photon cluster and to the extrapolation of track at the LKr plane.

The $K^+ \to \pi^0 e^+ \nu$ decay channel ($Ke3$) is used for normalization and the selection criteria are the same as the signal, except for the radiative photon cluster identification in the LKr calorimeter. This brings to the cancellation of several systematic effects due to the not ideal description of the reality in the Monte Carlo simulations. The normalized branching ratio is then computed as described in Equation A.3:

$$\frac{Br(K^+ \to \pi^0 e^+ \nu\gamma)}{Br(K^+ \to \pi^0 e^+ \nu)} = \frac{N^{signal} - N^{bkg}}{N^{norm} - N^{bkg-norm}} \cdot \frac{A^{norm}}{A^{signal}} \cdot \frac{\epsilon_{trig}^{norm}}{\epsilon_{trig}^{signal}} \tag{A.3}$$

where $N^{signal(norm)}$ is the number of selected signal (normalization) events, N^{bkg} is the number of expected background events in the signal selection, $N^{bkg-norm}$ is the number of expected background events in the normalization selection, A is the acceptance of the selections measured with MC simulation, ϵ_{trig} is the trigger efficiency for the two selections, measured with data.

The kinematics of the signal and normalization decays are reconstructed using the two variables defined in Equation A.4 and Equation A.5:

$$m^2_{miss}(Ke3\gamma) = (P_K - P_e - P_{\pi^0} - P_\gamma)^2 \tag{A.4}$$

$$m^2_{miss}(Ke3) = (P_K - P_e - P_{\pi^0})^2 \tag{A.5}$$

where $P_{particle}$ are the four-momenta of the reconstructed particles.

In particular, the $K^+ \to \pi^0 e^+ \nu\gamma$ kinematic signal region is defined by the two following conditions:

$$|m^2_{miss}(Ke3\gamma)| < 11000\ MeV^2/c^4 \tag{A.6}$$

$$m^2_{miss}(Ke3) > 5000\ MeV^2/c^4 \tag{A.7}$$

since the quantity $m^2_{miss}(Ke3\gamma)$ must be compatible with 0 (neutrino squared mass) within the experimental resolution, while the quantity $m^2_{miss}(Ke3)$ must be larger than 0 due to the presence of the photon radiated directly.

A.1.2 Background estimation

The main background contribution to the selected $K^+ \to \pi^0 e^+ \nu\gamma$ sample is represented by $K^+ \to \pi^0 e^+ \nu$ events with one more cluster coming from pile-up activity in the LKr (so-called *accidental* background).

The cut in Equation A.7 is very powerful against the *accidental* background, as shown in Figure A.2.

An additional contribution is given by $K^+ \to \pi^0 \pi^0 e^+ \nu$ events with one photon, coming from $\pi^0 \to \gamma\gamma$ decays, not detected. Contributions coming from other kaon decay channels is measured and it is negligible.

All the background sources are studied with Monte Carlo simulation, except for the *accidental* background which is estimated from data (Figure A.2).

The background over signal ratio (B/S) is reported in Table A.2, together with the other results of the analysis.

The background contamination of the normalization selection is negligible, since the measured B/S is $\sim 10^{-4}$.

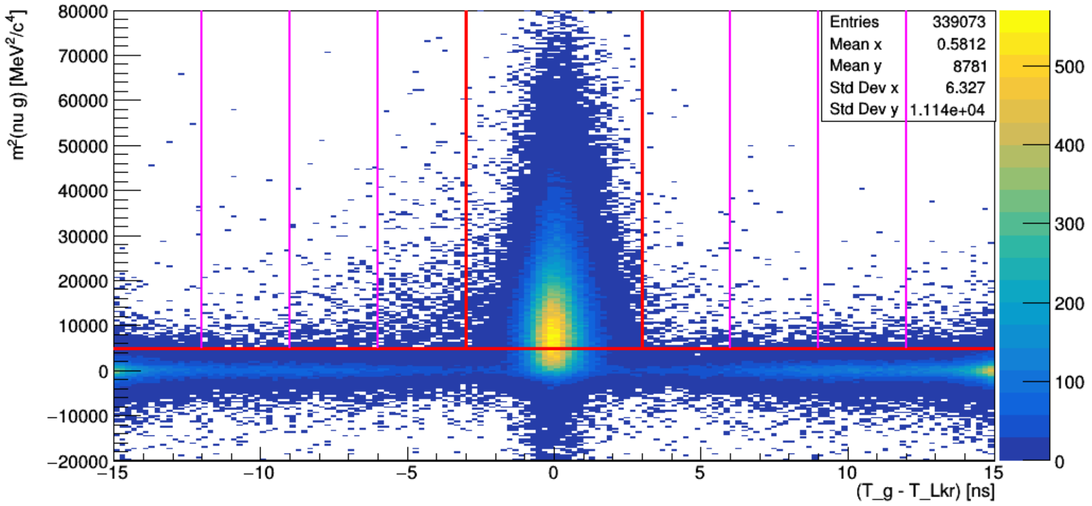

Figure A.2: Reconstructed $m^2_{miss}(Ke3)$ as a function of the difference between the radiative photon cluster time $T(\gamma)$ and the average time of e^+ and π^0 clusters $T(LKr)$, in the $K^+ \to \pi^0 e^+ \nu\gamma$ selection. The cut described in Equation A.7 is shown together with the time windows used for the radiative photon selection (± 3 ns, in red) and the sidebands (in magenta) used for the estimation and validation of the *accidental* background.

A.1.3 Uncertainties of Br measurement

The statistical uncertainty on the branching ratio measurement is given by the Poissonian fluctuation of the number of observed signal and normalization events.

The systematic uncertainties come from the errors of the selections acceptances and the trigger efficiencies estimations, and from the estimation of N^{bkg} (Equation A.3). An other not negligible source of systematic uncertainty is related to the radiative photon selection, where the LKr response, in particular at small energies, is not well reproduced in MC and the effect does not cancel in the normalization. This is estimated to be about 0.5% relative.

Few checks for possible additional systematic uncertainties are still ongoing, even if they are expected to be negligible with respect to the sources already studied.

A.1.4 A_ξ measurement

A *raw* measurement of A_ξ is obtained applying the formula in Equation A.1 directly on the selected data sample: A_ξ^{raw}. Then it must be corrected by the offset introduced by the selection, that is measured with MC simulation comparing the generated and the reconstructed values of the asymmetry: $A_\xi^{offset} = A_\xi^{MC-reco} - A_\xi^{MC-gene}$. The final measurement is then obtained as: $A_\xi^{final} = A_\xi^{raw} - A_\xi^{offset}$.

The statistical uncertainty of the final measurement is given by the statistical fluctuation of A_ξ^{raw}, that can be derived from the binomial distribution and it is due to the limited statistics of the data sample.

The systematic uncertainty of the final measurement is given by the statistical fluctuation of A_ξ^{offset}, that can be derived from the binomial distribution and it is due to the limited statistics of the Monte Carlo sample; other possible systematic sources are considered to be negligible.

A.1.5 Results

The distributions of $m^2_{miss}(Ke3\gamma)$ and ξ in the final $K^+ \to \pi^0 e^+ \nu\gamma$ sample are reported in Figure A.3.

The same cut-off thresholds of Table A.1 are used to define the $K^+ \to \pi^0 e^+ \nu\gamma$ kinematic range and to measure the branching ratio normalized to the $K^+ \to \pi^0 e^+ \nu$ channel and the A_ξ asymmetry. The preliminary results are reported in Table A.2 and represent the most precise measurements ever performed for those physics quantities, to be compared with Table A.1 and Equation A.2. They refer to the analysis of the full 2017-2018 data set collected by NA62.

E_γ cut	$\theta_{e,\gamma}$ cut	N^{signal}	B/S	$\frac{Br(K^+\to\pi^0 e^+\nu\gamma)}{Br(K^+\to\pi^0 e^+\nu)}$ $[10^{-2}]$	A_ξ
$E_\gamma > 10\ MeV$	$\theta_{e,\gamma} > 10°$	$128.3\ K$	0.45%	$1.670 \pm 0.005 \pm 0.010$	$0.001 \pm 0.003 \pm 0.003$
$E_\gamma > 30\ MeV$	$\theta_{e,\gamma} > 20°$	$53.0\ K$	0.62%	$0.593 \pm 0.003 \pm 0.005$	$0.001 \pm 0.004 \pm 0.004$
$E_\gamma > 10\ MeV$	$0.6 < \cos\theta_{e,\gamma} < 0.9$	$38.7\ K$	0.29%	$0.517 \pm 0.003 \pm 0.004$	$-0.006 \pm 0.005 \pm 0.005$

Table A.2: Preliminary results for different kinematic cuts (in the kaon rest frame), to be compared with Table A.1 and Equation A.2, related to the full NA62 2017-2018 data set. The third column reports the number of selected signal events, the fourth column reports the B/S ratio, the fifth column reports the measurement of $K^+ \to \pi^0 e^+ \nu\gamma$ branching ratio normalized to $K^+ \to \pi^0 e^+ \nu$, while the last column reports the A_ξ measurement.

The precision of the Br measurements is improved by a factor of 3 with respect to the previous measurements.

The central values of all the Br measurements are about 7% smaller than the values predicted by the theory, depending on the kinematic range definition, therefore it opens an interesting scenario to be further investigated.

The A_ξ measurements are actually only an upper limit and their precision is still two orders of magnitude far from the theoretical expectation. In any case they improve the experimental state of the art by a factor of 3 in terms of precision.

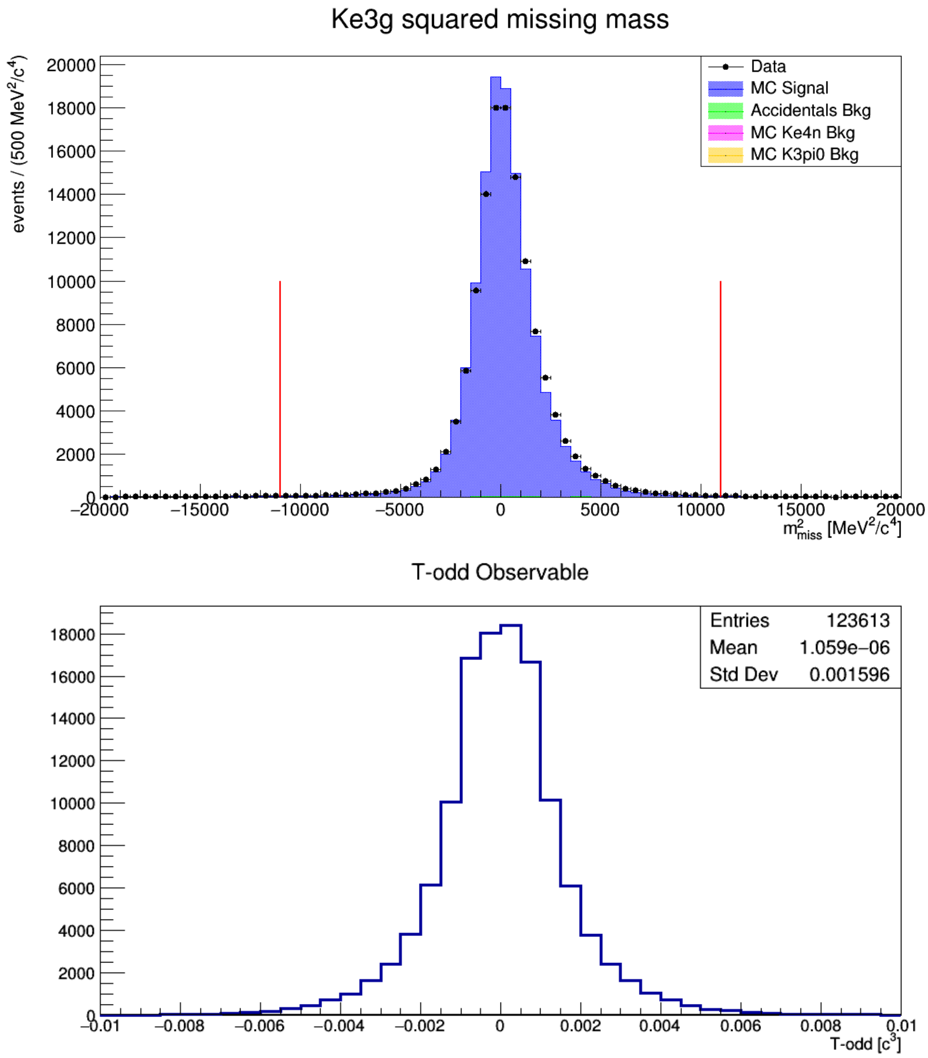

Figure A.3: Distributions of $m^2_{miss}(Ke3\gamma)$ (Top) and ξ (Bottom) for selected $K^+ \to \pi^0 e^+ \nu\gamma$ events with $E_\gamma > 10\ MeV$, $\theta_{e,\gamma} > 10°$ in the kaon rest frame. The cut described in Equation A.6 is shown.

A.2 LKr energy fine calibration

Before the introduction of the new algorithm, the fine calibration of the LKr cluster energy was performed exploiting the positrons E/p, i.e. the ratio between the energy deposited in the LKr calorimeter and the momentum measured by the STRAW spectrometer for positron tracks. The new algorithm, instead, relies on the invariant mass of the photons pairs coming form $\pi^0 \to \gamma\gamma$ decays. This is why they are also called E/p-calibration and π^0-calibration, respectively.

The goal of the calibration algorithm is to measure a calibration factor f, as a function of the reconstructed energy E^{reco}, that can be used to find the *corrected* energy $E^{corrected}$, as follows:

$$f = f(E^{reco}) = \frac{E^{reco}}{E^{corrected}} \;\to\; E^{corrected} = \frac{E^{reco}}{f(E^{reco})} \tag{A.8}$$

A.2.1 E/p-calibration

The E/p-calibration is based on two fundamental assumptions: the positron mass is negligible with respect to the momentum; a positron deposits 100% of its energy inside the LKr calorimeter. Under those assumptions, the E/p ratio should be equal to 1 (in natural units) for all the positrons: the STRAW momentum measurement corresponds to the *corrected* energy of the positron and the LKr energy measurement corresponds to the *reconstructed* energy of the positron.

At the first order the relation between the *corrected* energy and the *reconstructed* energy can be assumed to be linear, with two parameters (a scaling factor and an offset):

$$E^{reco} = A \cdot E^{corrected} + B \tag{A.9}$$

The two parameters A and B are extracted fitting the distribution of the LKr energy (E^{reco}) as a function of the STRAW momentum ($E^{corrected}$). Then, starting from Equation A.9, the calibration factor defined in Equation A.8 can be expressed as:

$$f^{E/p} = \frac{A \cdot E^{reco}}{E^{reco} - B} \tag{A.10}$$

The main limitation of the E/p-calibration algorithm is that the positron can loose energy between the STRAW spectrometer and LKr calorimeter, for example interacting with the material of the RICH mirrors. In this case the calibration procedure brings to an overestimation of the LKr cluster energy and this error is crucial in particular at small energies.

The effect has been observed in the $K^+ \to \pi^0 e^+ \nu\gamma$ analysis, reconstructing $m^2_{miss}(Ke3)$ of the $K^+ \to \pi^0 e^+ \nu$ events (Equation A.5), used as normalization channel, and the invariant mass of the photon pair coming from the $\pi^0 \to \gamma\gamma$ decay ($m_{\gamma\gamma}(\pi^0)$): in both the cases there is a shift of the peak with respect to the expected value, compatible with an overestimation of the LKr clusters energy, as shown in Figure A.4.

A.2.2 π^0-calibration

In order to fix the issue, an independent calibration algorithm has been developed, that relies only on the kinematics of the $\pi^0 \to \gamma\gamma$ decay. Under the approximation

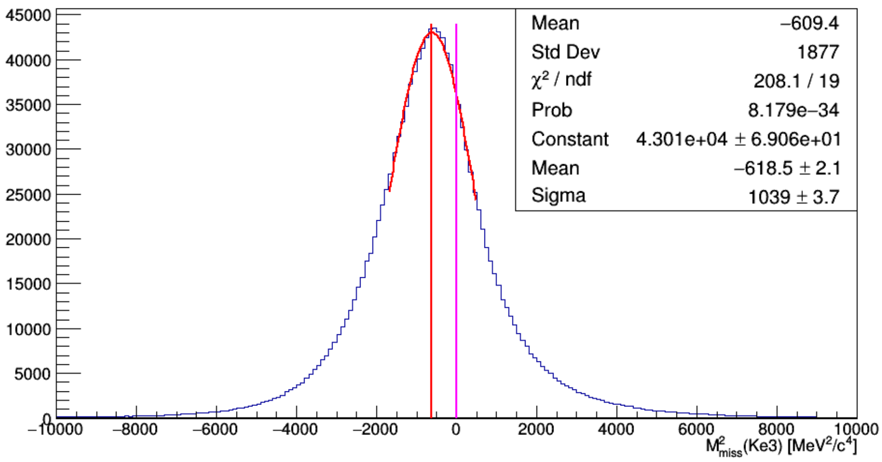

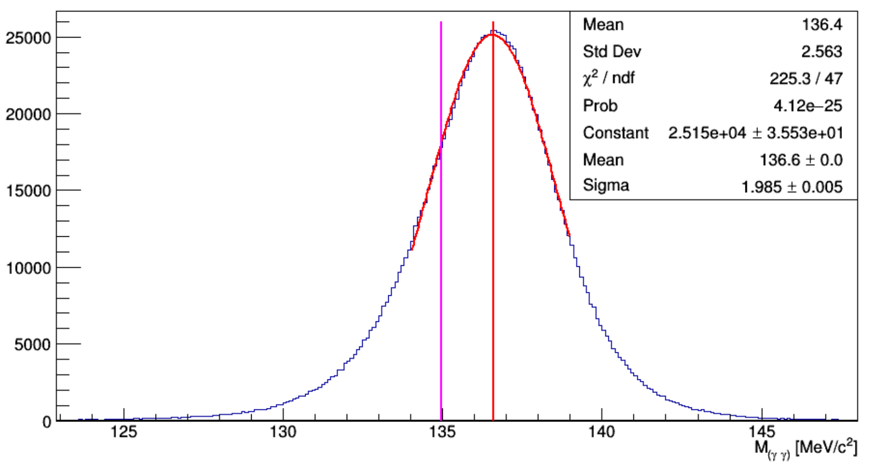

Figure A.4: Reconstructed $m^2_{miss}(Ke3)$ (Top) and $m_{\gamma\gamma}(\pi^0)$ (Bottom), in selected $K^+ \to \pi^0 e^+ \nu$ events with the E/p-calibration applied, from Monte Carlo simulation. The red line shows the peak value obtained fitting the distribution, while the magenta line shows the expected value.

of $\sin\theta_{\gamma\gamma} \simeq \theta_{\gamma\gamma}$ (where $\theta_{\gamma\gamma}$ is the angle between the two photons) the following relation can be derived from purely kinematic considerations:

$$(m_{\pi^0})^2 = \frac{D^2_{\gamma\gamma}}{(Z_{LKr} - Z_{vtx})^2} \cdot (E_1 \cdot E_2) \tag{A.11}$$

where $D_{\gamma\gamma}$ is the distance between the two photons clusters in the LKr transverse plane, Z_{LKr} is the Z coordinate of the LKr transverse plane, Z_{vtx} is the Z coordinate of the decay vertex, E_1 and E_2 are the energies of the two photons. The approximation is completely allowed in this case since $\theta_{\gamma\gamma} \sim 0.01\ rad$.

The initial part of the π^0-calibration algorithm consists in the selection of a clean sample of $K^+ \to \pi^+\pi^0$ decays, reconstructing the Z_{vtx} with the matching between the kaon and the charged pion and identifying the two photons clusters in the LKr, measuring their positions and energies.

The algorithm is then developed in 4 steps, since it is an iterative converging process.

The first step, also called *symmetric step*, is used to find out a first correction on average for both the clusters. In order to reduce the effect given by the different energies of the two clusters, only events with $|E_1 - E_2| < 1\ GeV$ (so-called *symmetric condition*) are used. The π^0 mass is reconstructed according to Equation A.11 and the calibration factor of Equation A.8 is computed comparing that value with the π^0 mass provided by the PDG [43]:

$$f^{symm} = \frac{m_{\pi^0}^{reco}}{m_{\pi^0}^{PDG}} \tag{A.12}$$

The values of f^{symm} are plotted as a function of the mean of the two clusters energies and then the distribution is fitted with a polynomial of 7^{th} degree, to find an analytical expression for $f^{symm}(E^{reco})$, as shown in Figure A.5.

The limitations of the symmetric step are the following: due to the *symmetric condition*, it covers only the central range of energies, i.e. 15-25 GeV, and it returns an average correction for both the clusters. This last effect is mitigated by the *symmetric condition*.

The second step, called *Asymmetric-1*, is performed on the same $K^+ \to \pi^+\pi^0$ events selection, after the application of $f^{symm}(E^{reco})$ to only one photon with energy in the range 15-25 GeV. If both the photons are outside the energy range, the event is rejected; if both the photons are inside the energy range, a random choice is applied. Let's call the corrected cluster "1" and the other cluster "2". The *corrected* energy of the cluster 2, $E_2^{corrected}$, is then obtained inverting the Equation A.11, assuming the PDG π^0 mass, and trusting on the corrected value of E_1. Then the calibration factor of Equation A.8 is computed comparing such value with the reconstructed energy of cluster 2, E_2^{reco}:

$$f^{asymm} = \frac{E_2^{reco}}{E_2^{corrected}} \tag{A.13}$$

The values of f^{asymm} are plotted as a function of E_2^{reco} and the distribution is fitted with a polynomial of 7^{th} degree, to find an analytical expression for $f^{asymm}(E^{reco})$, as shown in Figure A.5.

With respect to the symmetric step, the asymmetric step covers a larger energy range and find out a correction on the energy of one single cluster, instead of an average correction for the two clusters. On the other hand, the main disadvantage is that it is strongly affected by the precision of the correction given by the previous step: if the energy of the cluster 1 is wrongly calibrated, also $E_2^{corrected}$ will be wrong in the opposite direction of E_1. Therefore more asymmetric steps are needed, that will bring to an oscillation of $f^{asymm}(E^{reco})$ in each step, around the correct values. In order to make the procedure convergeing, the average of the results of steps n and $n-1$ is the output used for the step $n+1$.

Three asymmetric steps are performed (Figure A.5), as a compromise between precision and computation time, and then the last output, that should be used for the step *Asymmetric-4*, is actually the final result of the calibration procedure. This is enough to determine $f(E^{reco})$ in the energy range 2-50 GeV: then for clusters with energy smaller than 2 GeV, $f(2\ GeV)$ is used, while for clusters with energy larger than 50 GeV, $f(50\ GeV)$ is used.

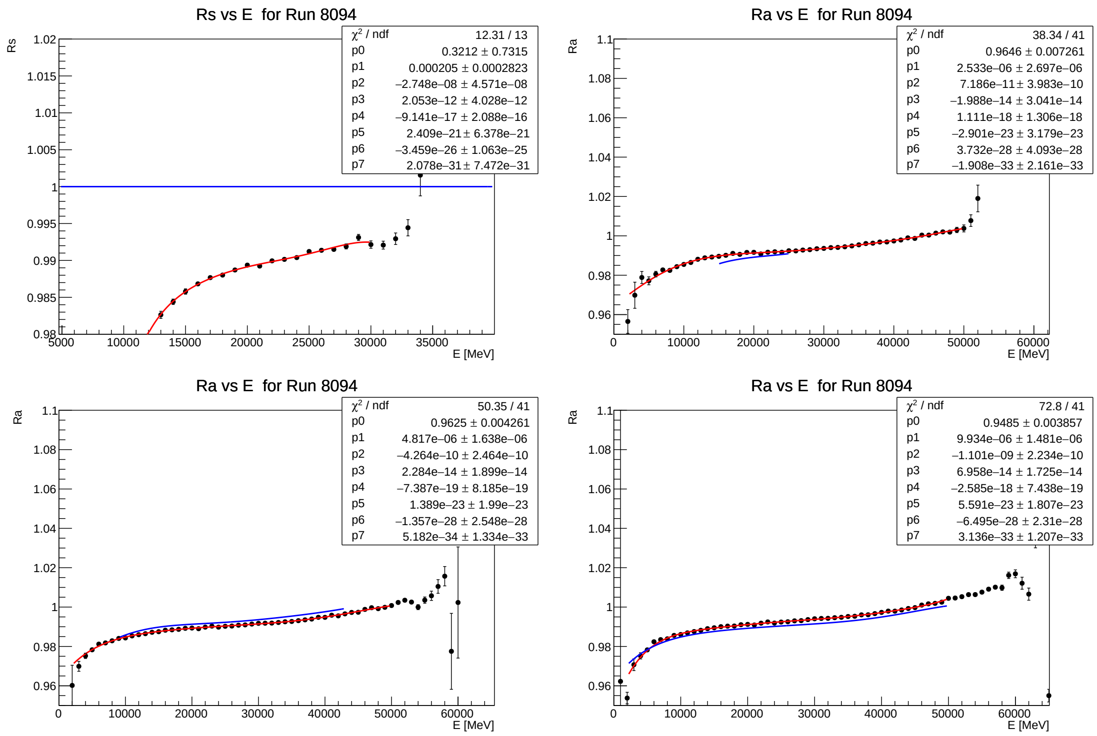

Figure A.5: Results of π^0-calibration steps: Symmteric (Top-Left), Asymmetric-1 (Top-Right), Asymmetric-2 (Bottom-Left), Asymmetric-3 (Bottom-Right). The ratio $E^{reco}/E^{corrected}$ is represented as a function of E^{reco}. The blue curve represent the correction obtained from the previous step. The dots are the results obtained in each energy bin, the red curve is the result of the fit with a 7^{th} degree polynomial. The *oscillation* effect due to the definition of the asymmetric step algorithm is evident.

The choice of a 7^{th} degree polynomial to fit the distribution is motivated by the fact that it is not possible to determine which is the behaviour of the distribution a-priori, therefore it is only possible to follow the experimental results, giving enough degrees of freedom to the fitting function.

The calibration algorithm is applied in the central processing of the data and provides run-by-run calibrations. It is also applied similarly to the Monte Carlo samples. When in a new MC version there are changes that could affect the calibration output, the algorithm is run again and a new set of calibration is produced.

The calibration results of four different Monte Carlo versions, and using both the E/p and the π^0 algorithms, are shown in Figure A.6, where the different behaviour of the two approaches is evident, in particular at small energies.

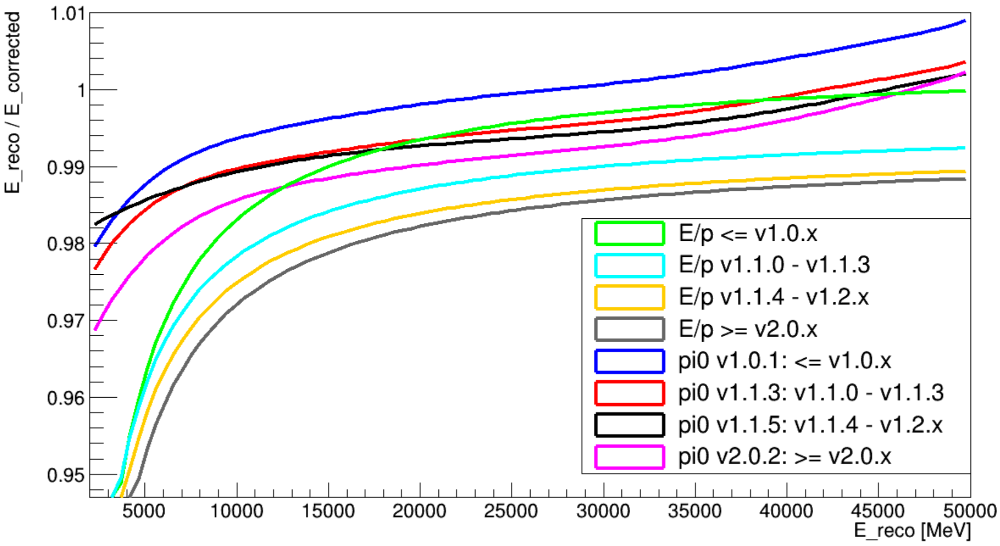

Figure A.6: Results of LKr energy fine calibration ($E^{reco}/E^{corrected}$ vs E^{reco}), for four different Monte Carlo versions and using both the E/p and the π^0 algorithms.

The same distributions of Figure A.4 are reported in Figure A.7, after the application of the π^0-calibration in place of the E/p calibration: it is evident how the peaks of the distributions are now very close to the expected values, that confirming the validity and the improvement of the new approach.

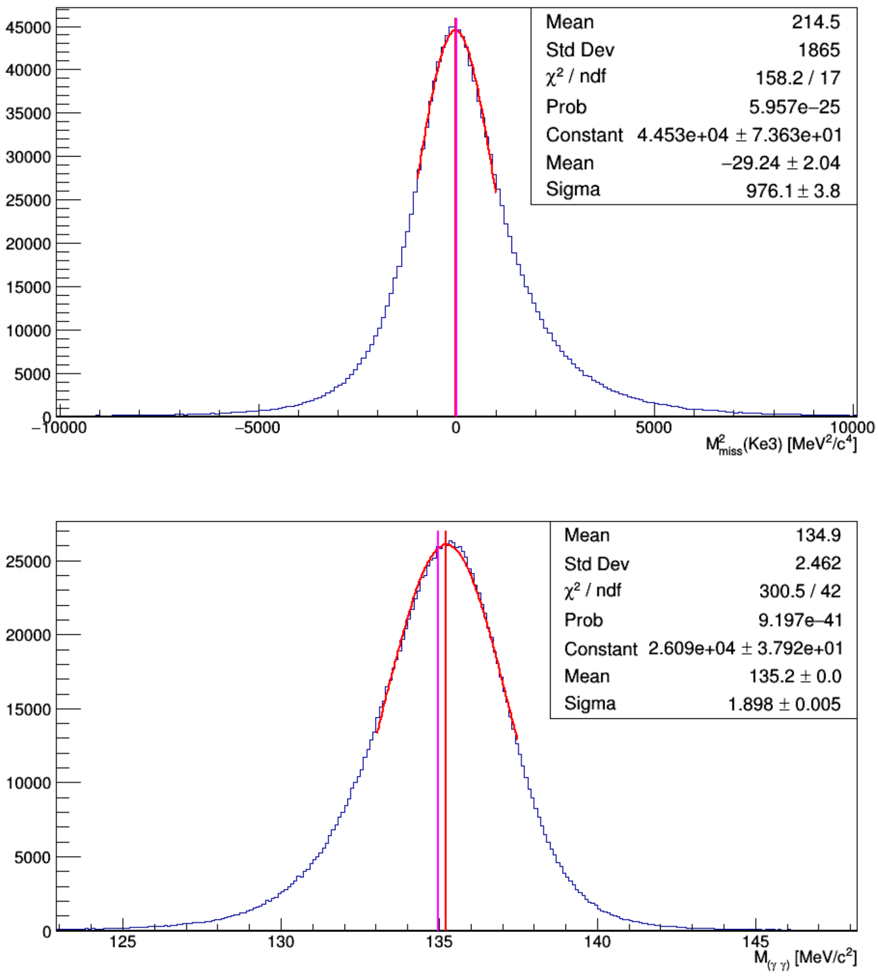

Figure A.7: Reconstructed $m^2_{miss}(Ke3)$ (Top) and $m_{\gamma\gamma}(\pi^0)$ (Bottom), in selected $K^+ \to \pi^0 e^+ \nu$ events with the π^0-calibration applied, from Monte Carlo simulation. The red line shows the peak value obtained fitting the distribution, while the magenta line shows the expected value.

Bibliography

[1] S.L. Glashow. «Partial Symmetries of Weak Interactions». In: *Nucl. Phys.* 22 (1961), pp. 579–588. DOI: 10.1016/0029-5582(61)90469-2 (cit. on p. xvii).

[2] Steven Weinberg. «A Model of Leptons». In: *Phys. Rev. Lett.* 19 (21 Nov. 1967), pp. 1264–1266. DOI: 10.1103/PhysRevLett.19.1264. URL: https://link.aps.org/doi/10.1103/PhysRevLett.19.1264 (cit. on p. xvii).

[3] Abdus Salam. «Weak and Electromagnetic Interactions». In: *Conf. Proc. C* 680519 (1968), pp. 367–377. DOI: 10.1142/9789812795915_0034 (cit. on p. xvii).

[4] John F. Donoghue, Eugene Golowich, and Barry R. Holstein. *Dynamics of the Standard Model*. 2nd ed. Cambridge Monographs on Particle Physics, Nuclear Physics and Cosmology. Cambridge University Press, 2014. DOI: 10.1017/CBO9780511803512 (cit. on p. xvii).

[5] Georges Aad et al. «Observation of a new particle in the search for the Standard Model Higgs boson with the ATLAS detector at the LHC». In: *Phys. Lett. B* 716 (2012), pp. 1–29. DOI: 10.1016/j.physletb.2012.08.020. arXiv: 1207.7214 [hep-ex] (cit. on p. xvii).

[6] Serguei Chatrchyan et al. «Observation of a New Boson at a Mass of 125 GeV with the CMS Experiment at the LHC». In: *Phys. Lett. B* 716 (2012), pp. 30–61. DOI: 10.1016/j.physletb.2012.08.021. arXiv: 1207.7235 [hep-ex] (cit. on p. xvii).

[7] F. Englert and R. Brout. «Broken Symmetry and the Mass of Gauge Vector Mesons». In: *Phys. Rev. Lett.* 13 (1964), pp. 321–323. DOI: 10.1103/PhysRevLett.13.321 (cit. on p. xvii).

[8] Peter W. Higgs. «Broken symmetries, massless particles and gauge fields». In: *Phys. Lett.* 12 (1964), pp. 132–133. DOI: 10.1016/0031-9163(64)91136-9 (cit. on p. xvii).

[9] Peter W. Higgs. «Broken Symmetries and the Masses of Gauge Bosons». In: *Phys. Rev. Lett.* 13 (1964), pp. 508–509. DOI: 10.1103/PhysRevLett.13.508 (cit. on p. xvii).

[10] G.S. Guralnik, C.R. Hagen, and T.W.B. Kibble. «Global Conservation Laws and Massless Particles». In: *Phys. Rev. Lett.* 13 (1964), pp. 585–587. DOI: 10.1103/PhysRevLett.13.585 (cit. on p. xvii).

[11] Peter W. Higgs. «Spontaneous Symmetry Breakdown without Massless Bosons». In: *Phys. Rev.* 145 (1966), pp. 1156–1163. DOI: 10.1103/PhysRev.145.1156 (cit. on p. xvii).

[12] T.W.B. Kibble. «Symmetry breaking in nonAbelian gauge theories». In: *Phys. Rev.* 155 (1967), pp. 1554–1561. DOI: 10.1103/PhysRev.155.1554 (cit. on p. xvii).

[13] S.L. Glashow. «Partial Symmetries of Weak Interactions». In: *Nucl. Phys.* 22 (1961), pp. 579–588. DOI: 10.1016/0029-5582(61)90469-2 (cit. on p. xvii).

[14] Steven Weinberg. «A Model of Leptons». In: *Phys. Rev. Lett.* 19 (1967), pp. 1264–1266. DOI: 10.1103/PhysRevLett.19.1264 (cit. on p. xvii).

[15] Abdus Salam. «Weak and Electromagnetic Interactions». In: *Conf. Proc. C* 680519 (1968), pp. 367–377. DOI: 10.1142/9789812795915_0034 (cit. on p. xvii).

[16] Y. Fukuda et al. «Evidence for Oscillation of Atmospheric Neutrinos». In: *Phys. Rev. Lett.* 81 (8 Aug. 1998), pp. 1562–1567. DOI: 10.1103/PhysRevLett.81.1562. URL: https://link.aps.org/doi/10.1103/PhysRevLett.81.1562 (cit. on p. xvii).

[17] Q. R. Ahmad et al. «Direct Evidence for Neutrino Flavor Transformation from Neutral-Current Interactions in the Sudbury Neutrino Observatory». In: *Phys. Rev. Lett.* 89 (1 June 2002), p. 011301. DOI: 10.1103/PhysRevLett.89.011301. URL: https://link.aps.org/doi/10.1103/PhysRevLett.89.011301 (cit. on p. xvii).

[18] Marco Roncadelli. «Astrophysical and cosmological evidence for dark matter and dark energy». In: *PoS* NEUTEL2015 (2015), p. 018. DOI: 10.22323/1.244.0018 (cit. on p. xvii).

[19] Laurent Canetti, Marco Drewes, and Mikhail Shaposhnikov. «Matter and Antimatter in the Universe». In: *New J. Phys.* 14 (2012), p. 095012. DOI: 10.1088/1367-2630/14/9/095012. arXiv: 1204.4186 [hep-ph] (cit. on p. xvii).

[20] Augusto Ceccucci et al. *Proposal to measure the rare decay $K^+ \to \pi^+\nu\bar{\nu}$ at the CERN SPS*. Tech. rep. CERN-SPSC-2005-013. SPSC-P-326. Geneva: CERN, Apr. 2005. URL: `https://cds.cern.ch/record/832885` (cit. on pp. xviii, 12).

[21] Andrzej J. Buras, Dario Buttazzo, Jennifer Girrbach-Noe, and Robert Knegjens. «$K^+ \to \pi^+\nu\overline{\nu}$ and $K_L \to \pi^0\nu\overline{\nu}$ in the Standard Model: status and perspectives». In: *JHEP* 11 (2015), p. 033. DOI: `10.1007/JHEP11(2015)033`. arXiv: `1503.02693 [hep-ph]` (cit. on pp. xviii, 6–8).

[22] Monika Blanke, Andrzej J. Buras, and Stefan Recksiegel. «Quark flavour observables in the Littlest Higgs model with T-parity after LHC Run 1». In: *Eur. Phys. J. C* 76.4 (2016), p. 182. DOI: `10.1140/epjc/s10052-016-4019-7`. arXiv: `1507.06316 [hep-ph]` (cit. on pp. xviii, 9).

[23] Monika Blanke, Andrzej J. Buras, Bjorn Duling, Katrin Gemmler, and Stefania Gori. «Rare K and B Decays in a Warped Extra Dimension with Custodial Protection». In: *JHEP* 03 (2009), p. 108. DOI: `10.1088/1126-6708/2009/03/108`. arXiv: `0812.3803 [hep-ph]` (cit. on pp. xviii, 9).

[24] Andrzej J. Buras, Dario Buttazzo, and Robert Knegjens. «$K \to \pi\nu\overline{\nu}$ and ϵ/ϵ in simplified new physics models». In: *JHEP* 11 (2015), p. 166. DOI: `10.1007/JHEP11(2015)166`. arXiv: `1507.08672 [hep-ph]` (cit. on pp. xviii, 9–11).

[25] Paul Langacker. «The physics of heavy Z' gauge bosons». In: *Rev. Mod. Phys.* 81 (3 Aug. 2009), pp. 1199–1228. DOI: `10.1103/RevModPhys.81.1199`. URL: `https://link.aps.org/doi/10.1103/RevModPhys.81.1199` (cit. on pp. xviii, 9).

[26] Gino Isidori, Federico Mescia, Paride Paradisi, Christopher Smith, and Stephanie Trine. «Exploring the flavour structure of the MSSM with rare K decays». In: *JHEP* 08 (2006), p. 064. DOI: `10.1088/1126-6708/2006/08/064`. arXiv: `hep-ph/0604074` (cit. on pp. xviii, 9).

[27] Tomáš Blažek and Peter Maták. «Left–left squark mixing, $K^+ \to \pi^+\nu\bar{\nu}$ and minimal supersymmetry with large tanβ». In: *Int. J. Mod. Phys. A* 29.27 (2014), p. 1450162. DOI: `10.1142/S0217751X14501620`. arXiv: `1410.0055 [hep-ph]` (cit. on pp. xviii, 9).

[28] Morimitsu Tanimoto and Kei Yamamoto. «Probing SUSY with 10 TeV stop mass in rare decays and CP violation of kaon». In: *PTEP* 2016.12 (2016), 123B02. DOI: `10.1093/ptep/ptw160`. arXiv: `1603.07960 [hep-ph]` (cit. on pp. xviii, 9).

[29] Marzia Bordone, Dario Buttazzo, Gino Isidori, and Joachim Monnard. «Probing Lepton Flavour Universality with $K \to \pi\nu\bar{\nu}$ decays». In: *Eur. Phys. J. C* 77.9 (2017), p. 618. DOI: 10.1140/epjc/s10052-017-5202-1. arXiv: 1705.10729 [hep-ph] (cit. on pp. xviii, 10, 12).

[30] Dario Buttazzo, Admir Greljo, Gino Isidori, and David Marzocca. «B-physics anomalies: a guide to combined explanations». In: *JHEP* 11 (2017), p. 044. DOI: 10.1007/JHEP11(2017)044. arXiv: 1706.07808 [hep-ph] (cit. on pp. xviii, 10).

[31] Christoph Bobeth and Andrzej J. Buras. «Leptoquarks meet ε'/ε and rare Kaon processes». In: *JHEP* 02 (2018), p. 101. DOI: 10.1007/JHEP02(2018)101. arXiv: 1712.01295 [hep-ph] (cit. on pp. xviii, 10).

[32] S. Fajfer, N. Košnik, and L. Vale Silva. «Footprints of leptoquarks: from $R_{K^{(*)}}$ to $K \to \pi\nu\bar{\nu}$». In: *Eur. Phys. J. C* 78.4 (2018), p. 275. DOI: 10.1140/epjc/s10052-018-5757-5. arXiv: 1802.00786 [hep-ph] (cit. on pp. xviii, 10).

[33] Eduardo Cortina Gil et al. «First search for $K^+ \to \pi^+\nu\bar{\nu}$ using the decay-in-flight technique». In: *Phys. Lett. B* 791 (2019), pp. 156–166. DOI: 10.1016/j.physletb.2019.01.067. arXiv: 1811.08508 [hep-ex] (cit. on pp. xviii, 12, 14, 112).

[34] Eduardo Cortina Gil et al. «An investigation of the very rare $K^+ \to \pi^+\nu\bar{\nu}$ decay». In: *JHEP* 11 (2020), p. 042. DOI: 10.1007/JHEP11(2020)042. arXiv: 2007.08218 [hep-ex] (cit. on pp. xviii, 12, 14, 20, 34, 44, 46, 48, 51, 54, 55, 69, 81, 85, 100, 112).

[35] Radoslav Marchevski. «New result on the search for the $K^+ \to \pi^+\nu\bar{\nu}$ decay at the NA62 experiment at CERN». In: *ICHEP 2020 Conference* (July 2020). URL: https://indico.cern.ch/event/868940/contributions/3815641/ (cit. on p. xviii).

[36] Francesco Brizioli. «Measurement of $Br(K^+ \to \pi^+\nu\bar{\nu})$ with the NA62 experiment at CERN SPS». In: *CERN EP Seminars* (Oct. 2020). URL: https://indico.cern.ch/event/965896/ (cit. on pp. xviii, 30, 41, 47, 55, 57, 60–62, 71, 75, 79, 80, 83, 89, 91, 95–97, 101, 105, 106, 109, 111–116).

[37] G.D. Rochester and C.C. Butler. «Evidence for the Existence of New Unstable Elementary Particles». In: *Nature* 160 (1947), pp. 855–857. DOI: 10.1038/160855a0 (cit. on p. 1).

[38] J. H. Christenson, J. W. Cronin, V. L. Fitch, and R. Turlay. «Evidence for the 2π Decay of the K_2^0 Meson». In: *Phys. Rev. Lett.* 13 (4 July 1964), pp. 138–140. DOI: 10.1103/PhysRevLett.13.138. URL: https://link.aps.org/doi/10.1103/PhysRevLett.13.138 (cit. on p. 1).

[39] *LHCb : Technical Proposal*. Tech. Proposal. Geneva: CERN, 1998. URL: http://cds.cern.ch/record/622031 (cit. on p. 1).

[40] T. Abe et al. *Belle II Technical Design Report*. 2010. arXiv: 1011.0352 [physics.ins-det] (cit. on p. 1).

[41] Nicola Cabibbo. «Unitary Symmetry and Leptonic Decays». In: *Phys. Rev. Lett.* 10 (1963), pp. 531–533. DOI: 10.1103/PhysRevLett.10.531 (cit. on p. 1).

[42] S.L. Glashow, J. Iliopoulos, and L. Maiani. «Weak Interactions with Lepton-Hadron Symmetry». In: *Phys. Rev. D* 2 (1970), pp. 1285–1292. DOI: 10.1103/PhysRevD.2.1285 (cit. on p. 2).

[43] P.A. Zyla et al. «Review of Particle Physics». In: *PTEP* 2020.8 (2020), p. 083C01. DOI: 10.1093/ptep/ptaa104 (cit. on pp. 2–5, 18, 19, 71, 72, 103, 112, 128).

[44] Makoto Kobayashi and Toshihide Maskawa. «CP Violation in the Renormalizable Theory of Weak Interaction». In: *Prog. Theor. Phys.* 49 (1973), pp. 652–657. DOI: 10.1143/PTP.49.652 (cit. on p. 2).

[45] Lincoln Wolfenstein. «Parametrization of the Kobayashi-Maskawa Matrix». In: *Phys. Rev. Lett.* 51 (1983), p. 1945. DOI: 10.1103/PhysRevLett.51.1945 (cit. on p. 3).

[46] Gerhard Buchalla and Andrzej J. Buras. «Sin2beta from K —> pi neutrino anti-neutrino». In: *Phys. Lett. B* 333 (1994), pp. 221–227. DOI: 10.1016/0370-2693(94)91034-0. arXiv: hep-ph/9405259 (cit. on p. 5).

[47] Andrzej J. Buras, Felix Schwab, and Selma Uhlig. «Waiting for precise measurements of $K^+ \to \pi^+ \nu\bar{\nu}$ and $K_L \to \pi^0 \nu\bar{\nu}$». In: *Rev. Mod. Phys.* 80 (2008), pp. 965–1007. DOI: 10.1103/RevModPhys.80.965. arXiv: hep-ph/0405132 (cit. on p. 6).

[48] Andrzej J. Buras. «Weak Hamiltonian, CP violation and rare decays». In: *Les Houches Summer School in Theoretical Physics, Session 68: Probing the Standard Model of Particle Interactions*. June 1998, pp. 281–539. arXiv: hep-ph/9806471 (cit. on p. 6).

[49] Federico Mescia and Christopher Smith. «Improved estimates of rare K decay matrix elements from $K_{\ell 3}$ decays». In: 76.3, 034017 (Aug. 2007), p. 034017. DOI: 10.1103/PhysRevD.76.034017. arXiv: 0705.2025 [hep-ph] (cit. on p. 7).

[50] Joachim Brod, Martin Gorbahn, and Emmanuel Stamou. «Two-loop electroweak corrections for the $K \to \pi\nu\bar{\nu}$ decays». In: *Phys. Rev. D* 83 (3 Feb. 2011), p. 034030. DOI: 10.1103/PhysRevD.83.034030. URL: https://link.aps.org/doi/10.1103/PhysRevD.83.034030 (cit. on p. 7).

[51] Gerhard Buchalla and Andrzej J. Buras. «The rare decays $K \to \pi\nu\bar{\nu}$, $B \to X\nu\bar{\nu}$ and $B \to l^+l^-$: An Update». In: *Nucl. Phys. B* 548 (1999), pp. 309–327. DOI: 10.1016/S0550-3213(99)00149-2. arXiv: hep-ph/9901288 (cit. on p. 7).

[52] Joachim Brod and Martin Gorbahn. «Electroweak Corrections to the Charm Quark Contribution to K+ → pi+ nu anti-nu». In: *Phys. Rev. D* 78 (2008), p. 034006. DOI: 10.1103/PhysRevD.78.034006. arXiv: 0805.4119 [hep-ph] (cit. on p. 7).

[53] Gino Isidori, Federico Mescia, and Christopher Smith. «Light-quark loops in K —> pi nu anti-nu». In: *Nucl. Phys. B* 718 (2005), pp. 319–338. DOI: 10.1016/j.nuclphysb.2005.04.008. arXiv: hep-ph/0503107 (cit. on p. 7).

[54] Yuval Grossman and Yosef Nir. «K(L) → π^0 neutrino anti-neutrino beyond the standard model». In: *Phys. Lett. B* 398 (1997), pp. 163–168. DOI: 10.1016/S0370-2693(97)00210-4. arXiv: hep-ph/9701313 (cit. on p. 10).

[55] Xiao-Gang He, Xiao-Dong Ma, Jusak Tandean, and German Valencia. «Breaking the Grossman-Nir Bound in Kaon Decays». In: *JHEP* 04 (2020), p. 057. DOI: 10.1007/JHEP04(2020)057. arXiv: 2002.05467 [hep-ph] (cit. on p. 10).

[56] T Yamanaka. «Introduction to KAON2019 – Experiments –». In: *Journal of Physics: Conference Series* 1526 (Apr. 2020), p. 012001. DOI: 10.1088/1742-6596/1526/1/012001. URL: https://doi.org/10.1088%2F1742-6596%2F1526%2F1%2F012001 (cit. on p. 11).

[57] Y. Asano, E. Kikutani, S. Kurokawa, T. Miyachi, M. Miyajima, Y. Nagashima, T. Shinkawa, S. Sugimoto, and Y. Yoshimura. «Search for a Rare Decay Mode K+ —> pi+ Neutrino anti-neutrino and Axion». In: (Oct. 1981). Ed. by R.J. Cence, E. Ma, and A. Roberts, pp. 411–414. DOI: 10.1016/0370-2693(81)91172-2 (cit. on p. 11).

[58] S. Adler et al. «Measurement of the K+ –> pi+ nu nu branching ratio». In: *Phys. Rev. D* 77 (2008), p. 052003. DOI: 10.1103/PhysRevD.77.052003. arXiv: 0709.1000 [hep-ex] (cit. on p. 11).

[59] A. V. Artamonov et al. «Study of the decay $K^+ \to \pi^+\nu\overline{\nu}$ in the momentum region $140lt; P_\pi lt; 199$ MeV/c». In: *Phys. Rev. D* 79 (9 May 2009), p. 092004. DOI: 10.1103/PhysRevD.79.092004. URL: https://link.aps.org/doi/10.1103/PhysRevD.79.092004 (cit. on pp. 11, 13).

[60] J. K. Ahn et al. «Search for $K_L \to \pi^0\nu\overline{\nu}$ and $K_L \to \pi^0 X^0$ Decays at the J-PARC KOTO Experiment». In: *Phys. Rev. Lett.* 122 (2 Jan. 2019), p. 021802. DOI: 10.1103/PhysRevLett.122.021802. URL: https://link.aps.org/doi/10.1103/PhysRevLett.122.021802 (cit. on p. 13).

[61] S. Shinohara. «Search for the rare decay $K_L \to \pi^0\nu\bar{\nu}$ at J-PARC KOTO experiment». In: *J. Phys. Conf. Ser.* 1526.1 (2020), p. 012002. DOI: 10.1088/1742-6596/1526/1/012002 (cit. on pp. 13, 16).

[62] Teppei Kitahara, Takemichi Okui, Gilad Perez, Yotam Soreq, and Kohsaku Tobioka. «New Physics Implications of Recent Search for $K_L \to \pi^0\nu\bar{\nu}$ at KOTO». In: *Phys. Rev. Lett.* 124 (7 Feb. 2020), p. 071801. DOI: 10.1103/PhysRevLett.124.071801. URL: https://link.aps.org/doi/10.1103/PhysRevLett.124.071801 (cit. on pp. 15, 17).

[63] J.K. Ahn et al. «Study of the $K_L \to \pi^0\nu\bar{\nu}$ decay at the J-PARC KOTO experiment». In: (Dec. 2020). arXiv: 2012.07571 [hep-ex] (cit. on p. 15).

[64] Eduardo Cortina Gil et al. «Search for heavy neutral lepton production in K^+ decays to positrons». In: *Phys. Lett. B* 807 (2020), p. 135599. DOI: 10.1016/j.physletb.2020.135599. arXiv: 2005.09575 [hep-ex] (cit. on p. 18).

[65] Eduardo Cortina Gil et al. «Searches for lepton number violating K^+ decays». In: *Phys. Lett. B* 797 (2019), p. 134794. DOI: 10.1016/j.physletb.2019.07.041. arXiv: 1905.07770 [hep-ex] (cit. on p. 18).

[66] Eduardo Cortina Gil et al. «Search for heavy neutral lepton production in K^+ decays». In: *Phys. Lett. B* 778 (2018), pp. 137–145. DOI: 10.1016/j.physletb.2018.01.031. arXiv: 1712.00297 [hep-ex] (cit. on p. 18).

[67] Michele Corvino. «Novel technique to measure Lepton Universality ratio R_K at NA62». Presented 20 Apr 2020. 2020. URL: https://cds.cern.ch/record/2728458 (cit. on p. 18).

[68] Marco Boretto. «First observation of the rare decay mode $K^+ \to \mu^+\nu_\mu\mu^+\mu^-$ in the NA62 experiment at CERN SPS». Presented 15 Jan 2020. 2019. URL: https://cds.cern.ch/record/2716696 (cit. on p. 18).

[69] Lubos Bician. «Measurement of $K^+ \to \pi^+\mu^+\mu$ Decay Form Factor and Evaluation of Muon Veto and Charged Hodoscope Efficiencies at NA62 Experiment at CERN». Presented 06 May 2019. 2019. URL: https://cds.cern.ch/record/2675833 (cit. on p. 18).

[70] Elisa Minucci. «Search for Lepton Number and Flavor violations in K decays at the NA62 experiment». Presented 15 Nov 2018. 2018. URL: http://cds.cern.ch/record/2655875 (cit. on p. 18).

[71] Eduardo Cortina Gil et al. «Search for π^0 decays to invisible particles». In: (Oct. 2020). arXiv: 2010.07644 [hep-ex] (cit. on pp. 18, 69, 70, 88).

[72] Eduardo Cortina Gil et al. «Search for production of an invisible dark photon in π^0 decays». In: *JHEP* 05 (2019), p. 182. DOI: 10.1007/JHEP05(2019)182. arXiv: 1903.08767 [hep-ex] (cit. on p. 18).

[73] Lorenza Iacobuzio. «Heavy Neutral Lepton Decay Searches at the NA62 Experiment at CERN». Presented 2019. 2019. URL: https://cds.cern.ch/record/2712960 (cit. on p. 18).

[74] F Hahn et al. *NA62: Technical Design Document*. Tech. rep. NA62-10-07. Geneva: CERN, Dec. 2010. URL: https://cds.cern.ch/record/1404985 (cit. on p. 18).

[75] Eduardo Cortina Gil et al. «The Beam and detector of the NA62 experiment at CERN». In: *JINST* 12.05 (2017), P05025. DOI: 10.1088/1748-0221/12/05/P05025. arXiv: 1703.08501 [physics.ins-det] (cit. on pp. 18, 23, 25–28, 31, 32, 36–38, 42, 69).

[76] Riccardo Aliberti. «Particle Identification with Calorimeters for the Measurement of the Rare Decay $K^+ \to \pi^+\nu\bar{\nu}$ at NA62». Presented 21 Jan 2019. Aug. 2018. URL: https://cds.cern.ch/record/2671696 (cit. on pp. 18, 40, 64, 65).

[77] Radoslav Ivanov Marchevski. «First measurement of the $K^+ \to \pi^+\nu\bar{\nu}$ decay with the NA62 experiment at CERN». Presented 19 Feb 2019. July 2018. URL: https://cds.cern.ch/record/2663316 (cit. on p. 18).

[78] Collaboration NA62. *2018 NA62 Status Report to the CERN SPSC*. Tech. rep. CERN-SPSC-2018-010. SPSC-SR-229. Geneva: CERN, Apr. 2018. URL: https://cds.cern.ch/record/2312430 (cit. on p. 18).

[79] Collaboration NA62. *2019 NA62 Status Report to the CERN SPSC*. Tech. rep. CERN-SPSC-2019-012. SPSC-SR-249. Geneva: CERN, Mar. 2019. URL: https://cds.cern.ch/record/2668548 (cit. on p. 18).

[80] Collaboration NA62. *2020 NA62 Status Report to the CERN SPSC*. Tech. rep. CERN-SPSC-2020-007. SPSC-SR-266. Geneva: CERN, Mar. 2020. URL: https://cds.cern.ch/record/2713499 (cit. on pp. 18, 22, 56, 116).

[81] NA62 Collaboration. *ADDENDUM I TO P326 Continuation of the physics programme of the NA62 experiment*. Tech. rep. CERN-SPSC-2019-039. SPSC-P-326-ADD-1. Geneva: CERN, Oct. 2019. URL: https://cds.cern.ch/record/2691873 (cit. on pp. 18, 47, 116, 117).

[82] V. Fanti et al. «The beam and detector for the NA48 neutral kaon CP violation experiment at CERN». In: *Nuclear Instruments and Methods in Physics Research Section A: Accelerators, Spectrometers, Detectors and Associated Equipment* 574.3 (2007), pp. 433–471. ISSN: 0168-9002. DOI: https://doi.org/10.1016/j.nima.2007.01.178. URL: http://www.sciencedirect.com/science/article/pii/S0168900207002719 (cit. on pp. 22, 35, 37, 39).

[83] R. Ammendola et al. «The integrated low-level trigger and readout system of the CERN NA62 experiment». In: *Nucl. Instrum. Meth. A* 929 (2019), pp. 1–22. DOI: 10.1016/j.nima.2019.03.012. arXiv: 1903.10200 [physics.ins-det] (cit. on pp. 23, 34, 44).

[84] Matthew Moulson. «Searches for exotic particles at NA62». In: *PoS* ICHEP2018 (2019), p. 629. DOI: 10.22323/1.340.0629 (cit. on p. 24).

[85] M. Fiorini et al. «High rate particle tracking and ultra-fast timing with a thin hybrid silicon pixel detector». In: *Nucl. Instrum. Meth. A* 718 (2013). Ed. by Franco Cervelli, Giorgio Chiarelli, Francesco Forti, Marco Grassi, and Angelo Scribano, pp. 270–273. DOI: 10.1016/j.nima.2012.10.108 (cit. on p. 26).

[86] F. Ambrosino et al. «CHANTI: a fast and efficient charged particle veto detector for the NA62 experiment at CERN». In: *Journal of Instrumentation* 11.03 (Mar. 2016), P03029–P03029. DOI: 10.1088/1748-0221/11/03/p03029. URL: https://doi.org/10.1088%2F1748-0221%2F11%2F03%2Fp03029 (cit. on p. 29).

[87] G. Anzivino et al. «Light detection system and time resolution of the NA62 RICH». In: *Journal of Instrumentation* 15.10 (Oct. 2020), P10025–P10025. DOI: 10.1088/1748-0221/15/10/p10025 (cit. on pp. 33, 34).

[88] G. Anzivino et al. «Precise mirror alignment and basic performance of the RICH detector of the NA62 experiment at CERN». In: *JINST* 13.07 (2018), P07012. DOI: 10.1088/1748-0221/13/07/P07012. arXiv: 1809.04026 [physics.ins-det] (cit. on p. 34).

[89] D. Aisa et al. «Mirror system of the RICH detector of the NA62 experiment». In: *Journal of Instrumentation* 12 (Dec. 2017), P12017–P12017. DOI: 10.1088/1748-0221/12/12/P12017 (cit. on p. 34).

[90] Francesco Brizioli. «The RICH detector of the NA62 experiment at CERN». In: *2019 IEEE Nuclear Science Symposium (NSS) and Medical Imaging Conference (MIC)*. 2019, pp. 1–6. DOI: 10.1109/NSS/MIC42101.2019.9059969 (cit. on p. 34).

[91] F. Brizioli and R. Lollini. «The RICH detector of the NA62 experiment». In: *J. Phys. Conf. Ser.* 1526.1 (2020), p. 012033. DOI: 10.1088/1742-6596/1526/1/012033 (cit. on pp. 34, 35, 66–68).

[92] «The OPAL detector at LEP». In: *Nuclear Instruments and Methods in Physics Research Section A: Accelerators, Spectrometers, Detectors and Associated Equipment* 305.2 (1991), pp. 275–319. ISSN: 0168-9002. DOI: https://doi.org/10.1016/0168-9002(91)90547-4. URL: http://www.sciencedirect.com/science/article/pii/0168900291905474 (cit. on p. 41).

[93] J. Allison et al. «Recent developments in Geant4». In: *Nuclear Instruments and Methods in Physics Research Section A: Accelerators, Spectrometers, Detectors and Associated Equipment* 835 (2016), pp. 186–225. ISSN: 0168-9002. DOI: `https://doi.org/10.1016/j.nima.2016.06.125`. URL: `http://www.sciencedirect.com/science/article/pii/S0168900216306957` (cit. on p. 45).

[94] Riccardo Lollini. «Study of the upstream background for the measurement of the branching ratio of the $K^+ \to \pi^+\nu\bar{\nu}$ decay with the NA62 experiment at CERN». Feb. 2019 (cit. on p. 97).

[95] Eduardo Cortina Gil et al. «Search for a feebly interacting particle X in the decay $K^+ \to \pi^+ X$». In: (Nov. 2020). arXiv: `2011.11329 [hep-ex]` (cit. on p. 110).

[96] V.V. Braguta, A.A. Likhoded, and A.E. Chalov. «T odd correlation in the K(l3 gamma) decay». In: *Phys. Atom. Nucl.* 65 (2002). Ed. by J. Caparthy, pp. 1868–1876. DOI: `10.1103/PhysRevD.65.054038`. arXiv: `hep-ph/0106147` (cit. on pp. 119, 120).

[97] Eike H. Muller, Bastian Kubis, and Ulf-G. Meissner. «T-odd correlations in radiative K(l3)+ decays and chiral perturbation theory». In: *Eur. Phys. J. C* 48 (2006), pp. 427–440. DOI: `10.1140/epjc/s10052-006-0033-5`. arXiv: `hep-ph/0607151` (cit. on pp. 119, 120).

[98] J. Bijnens, G. Ecker, and J. Gasser. «Radiative semileptonic kaon decays». In: *Nucl. Phys. B* 396 (1993), pp. 81–118. DOI: `10.1016/0550-3213(93)90259-R`. arXiv: `hep-ph/9209261` (cit. on p. 120).

[99] Bastian Kubis, Eike H. Muller, Jurg Gasser, and Martin Schmid. «Aspects of radiative K+(e3) decays». In: *Eur. Phys. J. C* 50 (2007), pp. 557–571. DOI: `10.1140/epjc/s10052-007-0215-9`. arXiv: `hep-ph/0611366` (cit. on p. 120).

[100] I.B. Khriplovich and A.S. Rudenko. «$K^+_{l3\gamma}$ decays revisited: branching ratios and T-odd momenta correlations». In: *Phys. Atom. Nucl.* 74 (2011), pp. 1214–1222. DOI: `10.1134/S1063778811080102`. arXiv: `1012.0147 [hep-ph]` (cit. on p. 120).

[101] S.A. Akimenko. «Study of $K^- \to \pi^0 e^- \bar{\nu}_e \gamma$ Decay with ISTRA+ Setup». In: *Phys. Atom. Nucl.* 70 (2007), p. 702. DOI: `10.1134/S1063778807040114` (cit. on pp. 120, 121).

[102] A.Yu. Polyarush et al. «Study of $K^+ \to \pi^0 e^+ \nu\gamma$ decay with OKA setup». In: (Oct. 2020). arXiv: `2010.07983 [hep-ex]` (cit. on p. 120).